Flexo-Elastic and Electro-Optical Studies of some Novel Liquid Crystalline Systems

by

Reshma Balachandran

A thesis submitted for the

degree of Doctor of Philosophy

Laboratory of Advanced Electronic Materials

Department of Electronic and Electrical Engineering

TRINITY COLLEGE DUBLIN

The University of Dublin

November 2014

Declaration of Authorship

I, Reshma Balachandran, declare that this thesis has been composed by me and is entirely my own work, unless stated otherwise. The use of any other author's work has been duly acknowledged at their point of use. I confirm that:

- This thesis has not been submitted as an exercise for a degree at any other University.
- I agree to deposit this thesis in the University's open access institutional repository or allow the library to do so on my behalf. Trinity College Dublin has the permission to lend or copy this thesis on request, subject to Irish Copyright Legislation and TCD's conditions of use and acknowledgement.

Signed: Reshma

Date: 13/11/2014

Summary

This thesis presents the experimental investigation of the material properties of liquid crystalline systems composed of (i) bent-core molecules, (ii) bimesogens composed of rod-like molecules and (iii) dimesogens composed of a rod-like and bent-core mesogenic unit. Most of the studies were performed in the nematic phase of these materials. A brief summary of the work presented in this thesis is described below.

1. The flexo-elastic properties of three bent-core systems belonging to a homologous series are investigated. X-ray studies show that Smectic-*C* like cybotactic clusters are present in the nematic phase of compounds with longer chain length (C6, C7), while it is measurably absent in the shortest chain length material (C4). It is found experimentally that regardless of the presence/absence of clusters, the bend (K_{33}) elastic constant is always smaller in comparison to the splay (K_{11}) constant; suggesting that the elastic properties are more likely to be influenced by the bent shape of the molecules rather than the presence of clusters. The effective flexoelectric coefficients determined using the ULH technique are found to be larger than calamitic systems; however there is no evidence of giant flexoelectricity in the bent-core system studied (Chapter 3).

2. The elastic constants, effective flexoelectric coefficient and flexoelectric polarization are studied for a bimesogenic liquid crystal CBC11CB exhibiting a twist bend nematic phase (N_{tb}). Results show that K_{11} increases with decreasing temperature but the value of K_{33} tends to fall steadily as the temperature is reduced. The effective flexoelectric coefficient is found to be at least two times higher than for bimesogens that do not exhibit the N_{tb} phase. The flexoelectric polarization,

measured using pyroelectric technique, in the N_{tb} phase is almost two times greater than in its nematic phase (Chapter 4).

3. A new phenomenon of periodic self-assembly is observed close to the N - N_{tb} phase transition temperature in some bimesogens and their mixtures with the monomer 5CB. This phenomenon is reminiscent of the self-deformation and spontaneous chirality that appears in the system (Chapter 5).

4. The dielectric behaviour of a dimesogen BR1 composed of a bent-core unit combined with a laterally attached rod-like mesogenic core is investigated. The material shows dual frequency nematic mode and the sign reversal of dielectric anisotropy occurs at very low frequencies. Detailed analysis of the dielectric spectra is carried out using the Maeir-Meier (M-M) model by considering independent reorientation of each constituent mesogen. The dielectric behaviour is interpreted in terms of the Kirkwood correlation factors in the M-M equation, and the results suggest the presence of anti-parallel correlation of the transverse dipoles in the neighbouring layer of the Sm*C* like clusters (Chapter 6).

Acknowledgements

During the course of my research study at Trinity College Dublin, there have been many people who have helped and supported me. First and foremost, I would like to thank my supervisor Prof. Jagdish Vij for his outstanding guidance and support. He is an excellent teacher as well as a mentor, and constantly encouraged me in difficult times. I would sincerely wish to express my deepest gratitude to Dr. Vitaly Panov for his invaluable instructions and discussions. He has vast experience in the field of liquid crystal research, which he never hesitated to share with me, and was also extremely approachable, helpful and supportive throughout my research studies. Many of the results presented in this thesis were accomplished together with him. I would like to extend my sincere thanks to Prof. Antoni Kocot for his helpful advice and fruitful discussions throughout my PhD. The MATLAB programme to evaluate the bend elastic constant was written by him. I would also wish to express my gratitude towards Dr. Yuri Panarin for his valuable suggestions. He was always kind in sharing his expertise of liquid crystals. I also thank the Professors on my dissertation committee for sparing their valuable time to reading and evaluating this work.

My special appreciation goes to Dr. Chandani Perera, Dr. Mamatha Nagaraj and Dr. Yun Jang for their help and suggestions during my initial years as a research student. I shall also remain deeply indebted to Dr. Sithara Pavithran for her friendship, valuable suggestions and kind words. In her, I found an elder sister with whom I enjoyed discussing topics that extended beyond research activities.

I also wish to thank the staff at Department of Electronic and Electronic Engineering, Prof. Martin Burke, Dr. Tania Perova, Ms. Teresa Lawlor, Mr. Conor

Nolan, Mr. Shane Hunt, Mr. Robert Dempsey, Mr. John Squires and others for their endless help.

I whole-heartedly thank my friends Ms. Nitheen Kaperi, Dr. Lankani and Ms. Yue Lu from the chemistry department at TCD for their company. I've been invited to their lovely homes on several occasions and thoroughly enjoyed their wonderful hospitalities. My special thanks to Ms. Shanu Susan, Ms. Shareen, Ms. Sara, Ms. Zahraa and Ms. Fatema for always supporting me in all my endeavours.

Lastly, but most importantly, I would like to thank my parents and younger brother for their constant words of encouragement throughout my studies. Without their love and support, this work would have been difficult to accomplish.

Abbreviations

LC	Liquid Crystal
N/N_u	Uniaxial Nematic phase
N_b	Biaxial Nematic phase
N_{tb}	Twist Bend Nematic Phase
N_{cyb}	Cybotactic Nematic
N_{cybC}	Nematic phase with Smectic-C type cluster
NLC	Nematic Liquid Crystal
CLC, N^*	Chiral/Cholesteric Nematic Liquid Crystal
Sm*A*	Smectic-A phase
Sm*C*	Smectic-C phase
BCN	Bent Core Nematic
Cr	Crystal
I	Isotropic
^oC	Degree Centigrade (Celsius)
T	Temperature
C_T	Cross-over Temperature
T_{NI}	Transition Temperature from Isotropic to Nematic phase
K	Kelvin
ITO	Indium Tin Oxide
E	Electric Field

dc/DC	Direct Current
ac/AC	Alternating Current
DFN	Dual Frequency Nematic
HTP	Helical Twisting Power
ULH	Uniform Lying Helix
BC	Bent Core
K_{11}, K_{22}, K_{33}	Splay, Twist, Bend Elastic Constant
e_1, e_3	Splay, Bend Flexoelectric coefficient
$(e_1 - e_3)$	Effective Flexoelectric Coefficient
P_f	Flexoelectric Polarization
P_s	Spontaneous Polarization
ε', ε''	Real, Imaginary part of Dielectric Permittivity
$\Delta\varepsilon'$	Dielectric Anisotropy
S	Order Parameter
p	Pitch
V_{pk}	Peak Voltage

Table of Contents

3. Elastic and Flexoelectric Properties of Bent-Core Liquid Crystals

4. Elastic and Flexoelectric Properties of a Bimesogen

5. Electro-Optical Investigations at the N-N_{tb} Interface

6. Dielectric and Electro-Optical Investigations of a Dimesogen

7. Conclusion and Future Work

List of Figures

List of Tables

Chapter 1

Introduction

In this chapter, the fundamentals of liquid crystals and the theoretical tools required to understand the subject matter of the various works undertaken in this thesis are described.

Contents

1.1 Introduction to Liquid Crystals

Conventionally, there are three states of matter: solids, liquids and gases. The molecules in the solid state have a high degree of positional order (i.e. molecules are arranged in an ordered lattice) and orientational order (molecules mostly point in the same direction), while in the liquid state the molecules have much lower degree of positional and orientational order. In many organic compounds there exists a state of matter intermediate between solid crystal and isotropic liquids known as liquid crystals (LCs), whose degree of order lies between that of a crystal and a solid. This phase was first discovered by an Austrian botanist Friedrich Reinitzer in 1888. He observed that as the temperature of the solid sample (cholesteryl benzoate) was increased, the crystal changed into a hazy liquid, and on further heating it changed into a clear, transparent liquid. Because of his early work, Reinitzer is often credited with discovering a new phase of matter – the liquid crystal phase [1].

Liquid crystals exhibit many physical properties that are intermediate between those of solids and crystals. For example they possess mechanical properties of liquids such as viscosity, coalescence of droplets etc., and are also similar to crystals as they exhibit anisotropy in their optical, electrical, mechanical and magnetic properties. These intermediate phases are referred to as liquid crystalline phases or mesophases [1].

Liquid crystals can be classified as being either themotropic or lyotropic. Lyotropic LCs exhibit phase transitions as a function of both temperature and concentration of the LC molecules in a solvent, and have applications in biological systems. Thermotropic liquid crystals, on the other hand, show phase transition into the LC phases as the temperature of the material is altered and have use in technical applications. In this thesis we study the material properties of thermotropic LCs.

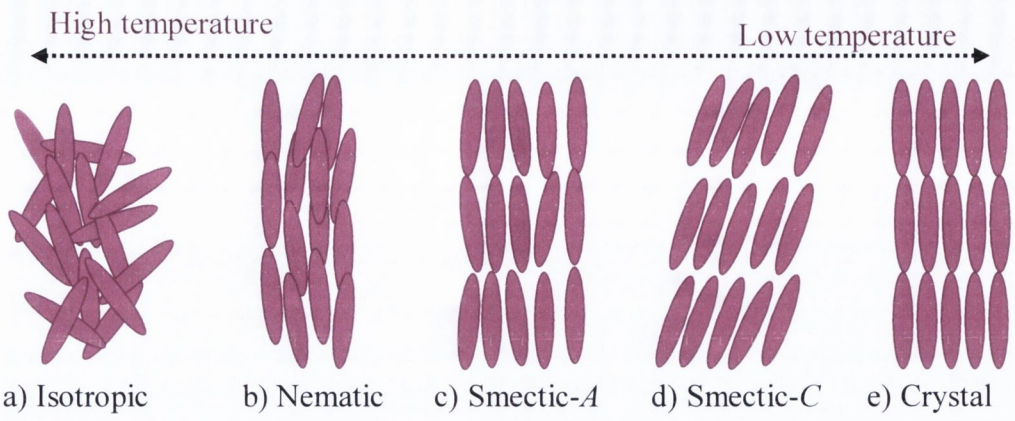

Figure 1.1: Phase sequence in calamitic liquid crystals

The molecular structure has a profound effect on the properties exhibited by the LC material and its phase behaviour. Based on the shape anisotropy, thermotropic LC molecules can be categorized as (i) rod-like/calamitics, (ii) banana/ bent-core, or (iii) discotic LCs.

1.2 Calamitcs

Calamitics or rod-like molecules are the most common types of LCs. The length-to-breadth ratio in calamitics is greater than unity, hence providing the required shape anisotropy. The typical structure of calamitic mesogen is composed of rigid core units consists of linearly linked aromatic or alicyclic rings and flexible terminal moieties composed of alky, alkoxy or cyano groups connected to both of its ends [2].

In the LC state, the unit vector **n** known as the director, defines the average direction in which the molecular long axes point. Depending on the degree of orientation and positional order, LCs exhibit different phases. A typical phase sequence of calamitic molecules on cooling from high to low temperature is: Isotropic - Nematic – Smectic-*A* – Smectic-*C* – Crystal (Fig. 1.1).

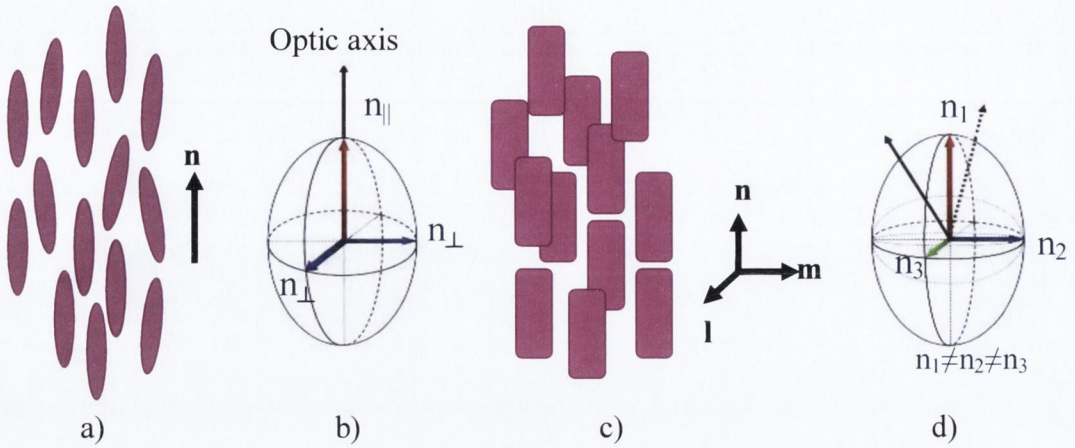

Figure 1.2: Molecular arrangement of uniaxial (a) and biaxial (c) nematic phases and their corresponding indicatrices (b) and (d).

The uniaxial nematic (*N or Nu*) is the simplest LC phase, wherein one axis is longer and preferred, and other two being equivalent. In the nematic phase the molecules tend to point along the director, but have no positional order; additionally the nematic director is apolar i.e., $\mathbf{n} \equiv -\mathbf{n}$. Some LCs can also be biaxial, possessing D_{2h} phase symmetry, with three mutually orthogonal symmetry axes ($n \neq l \neq m$).

In the smectic phase, the molecules possess one dimensional orientational and translational order. The molecules tend to align themselves in layers or planes and motion is restricted to these layers. These separate layers can flow past each other. In the Smectic-*A* (Sm*A*) mesophase, the director is perpendicular to the layer plane, while in the Smectic-*C* (Sm*C*) phase the director is at a constant tilt angle with respect to the layer normal, which is measured normal to the smectic plane.

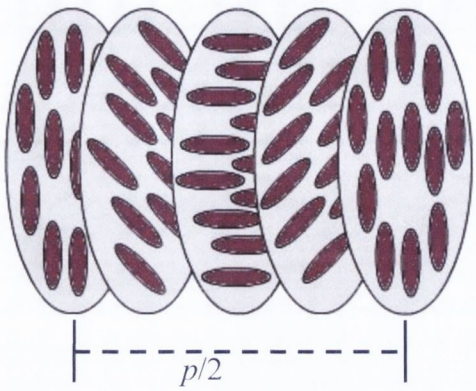

Figure 1.3: Cholesteric or Chiral nematic liquid crystalline phase

Another common phase is the cholesteric or chiral nematic (N^*) phase, wherein the director vector twists in space, resulting in a spiral or helical structure (Fig. 1.3). The most important characteristic of the cholesteric mesophase is its pitch. The pitch p is the distance required by the director to complete one full turn in the helix. The chiral nematic repeats itself at every half pitch, as $\mathbf{n} \equiv -\mathbf{n}$, hence the period of the N^* phase corresponds to $p/2$. Though the cholesteric phase occurs naturally in many LC compounds composed of chiral molecules, this mesophase can also be induced in achiral LCs by introducing a chiral dopant into the host material. The pitch can be varied by adjusting the concentration, c , of the chiral agent using the following equation [3]:

$$p = \frac{1}{\mathrm{HTP(c)}}, \qquad (1.1)$$

where HTP is the helical twisting power, and provides a measure of the ability of the chiral dopant to twist the NLC.

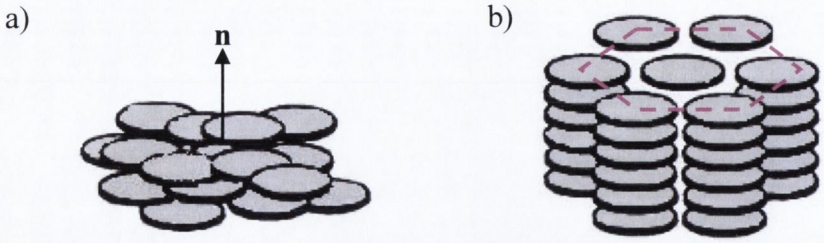

Figure 1.4: Schematic representation of (a) nematic phase and (b) hexagonal columnar phase exhibited by discotic LCs.

1.3 Discotics

Discotic LCs (DLCs) are composed of disc-shaped molecules which have an aromatic core and a series of alkyl side chains [4]. In this class of LCs the disc-like molecules are stacked one above the other to form liquid columns. The disc-like molecules can arrange themselves to form a nematic phase (Fig. 1.4(a)), with one-dimensional order. DLCs also exhibit columnar phases (Fig. 1.4(b) shows the hexagonal columnar phase) in which the molecules stack one above the other to form a hexagonal or rectangular array of molecular columns.

1.4 Bent-Cores

Typical structure of a bent-core liquid crystal consists of a bent-aromatic core connected to flexible tails on both sides (Fig. 1.5(a)). Though bent core molecules composed of intrinsically achiral molecules were first synthesized by Vorländer as early as 1930's [5]; their special properties were not realized until Niori et al. [6] and Link et al. [7] discovered polar switching and spontaneous breaking of the achiral symmetry in smectic phases. This demonstration led to intense research activity, carried out by several groups internationally [8] which got greatly accelerated during the last decade.

A variety of orthogonal smectic phases [9] have recently been discovered in several bent-core systems and several versions of columnar (Fig. 1.5(c)) and nematic phase have also been observed in some systems. In addition to these, compounds made of bent core molecules are known to exhibit a variety of liquid crystalline phases, designated as B_1, B_2....., where the letter B stands for banana/bent/bow shaped molecules and the suffix indicates the chronological order of the discovery [10] of the different B phases.

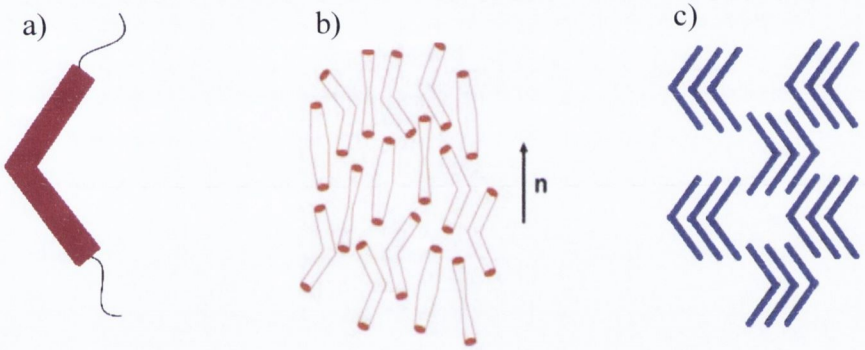

Figure 1.5: (a) Structure of a Bent core molecule, (b) Uniaxial nematic and (c) Col_r (B1) phase. Image (b) modified from [11].

1.4.1 Short Range Order in Bent-Core LCs

In bent core systems, a deviation from the rod-like shape and existence of large transverse dipole moment often gives rise to strong intermolecular interactions, leading to the formation of smectic-like (cybotactic) clusters [12,13]. The short-range structure is also described as an extension of the "cybotactic group" [14] proposed originally by de Vries [15]; de Vries suggested that layered molecular arrangements exist on short length and timescales, which are predominantly associated with pre-transitional

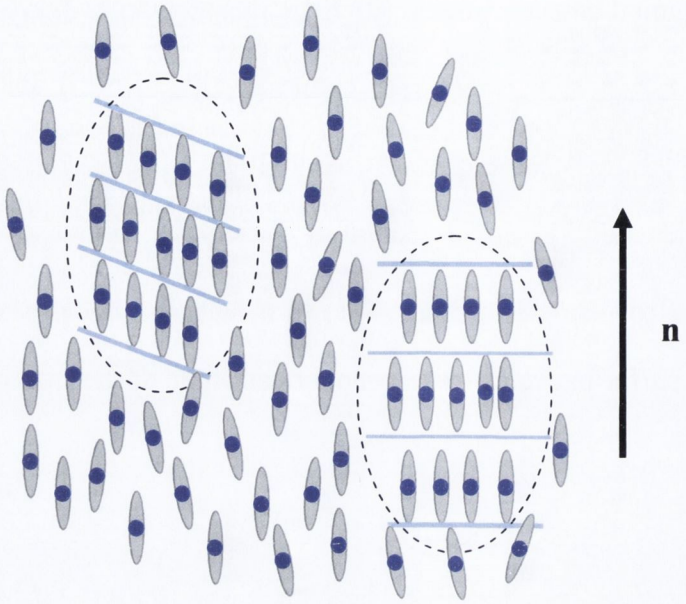

Figure 1.6: Schematic representation of a nematic phase exhibiting tilted (left) and normal (right) smectic fluctuations.

fluctuations near the nematic-smectic transition in calamitic molecules. A nematic phase with smectic-like ordering is described in the form of smectic fluctuations, in which the layer is either titled (Sm*C*-like clusters) or normal (Sm*A*-like clusters) to the nematic director (Fig. 1.6). Such a nematic phase is referred to as cybotactic nematic or simply N_{cyb}. In case of BCNs, such smectic-like clusters, formed as a result of the strong preference of the molecular shape to pack into layers [16], could manifest themselves over the entire nematic range even in the absence of an underlying smectic phase, as evidenced by several experimental results [9,16-17]. BCNs exhibiting N_{cyb} phase has garnered a lot of attention due to a range of interesting properties exhibited by them such as field induced biaxiality [18], sign reversal of dielectric anisotropy [19] etc. In Chapter 3 of this thesis, some bent-core compounds exhibiting the cybotactic nematic phase are investigated.

1.5 Bimesogens or Dimers

Figure 1.7: Schematic representation of bimesogens composed of (i) rod + rod and (ii) bent-core + bent-core molecules.

Liquid crystalline (LC) bimesogens or dimers or dimesogens are composed of two mesogenic units connected by a flexible spacer [20]. These materials are of significant interest due to a range of interesting phenomena exhibited by them; some of these properties are often different to that of conventional low molar mass LCs. Bimesogens can be symmetric or asymmetric, and are classified into those composed of (a) identical mesogenic units or (b) combining different types of units: such as the two non-identical rod-like molecules or bent-core molecules, or a calamitic unit connected to a bent-core or a discotic molecule (example of few combinations are shown in Fig. 1.7). The material properties in the resulting compounds are not only influenced by the constituent mesogens, but also the parity of the spacer connecting the two monomers [21]. For example, in LC dimers composed of rod-like molecules, even–spaced compounds predominantly consist of linear conformations [21]; the behaviour of the material properties, such as elastic constants, in these bimesogens are found to be similar to conventional monomesogens [22]. Odd-spaced bimesogens have an overall bent shape [21], and the behaviour in such compounds is similar to BCNs. In Chapters 4, 5 and 6 we will present some of the unusual properties observed in liquid crystal bimesogens.

1.6 Physical Properties of Nematic Liquid Crystals

1.6.1 Order Parameter

The amount of orientational order in a liquid crystalline state is quantitatively specified by the order parameter S (Fig. 1.8), which can be obtained by averaging the macroscopic molecular orientation with respect to the director **n**.

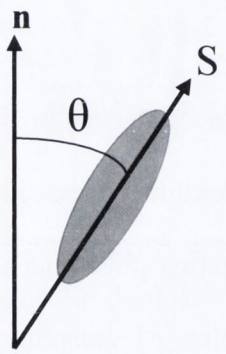

Figure 1.8: Schematic presentation of the Order Parameter.

The order parameter can be defined as the average of the second Legendre polynomial:

$$S = \langle P_2(\cos\theta) \rangle = \frac{1}{2}\langle 3\cos^2\theta - 1 \rangle, \qquad (1.2)$$

where θ is the angle between the director and long axis of the molecule, < > denotes the average over all the molecules in the sample. If the molecules are well aligned with the director, as in a perfect crystal, then S = 1. When the molecules are randomly oriented, S = 0. In liquid crystals, the order parameter value usually ranges from 0.3 to 0.9 and is temperature dependent [1]. S can also attain negative values (ranging from 0 to -0.5) if the molecules, on average, are perpendicular to **n**.

1.6.2 Dielectric Properties

The dielectric permittivity is an important parameter that characterizes the response of a liquid crystal sample to an applied electric field. Because of molecular and energy level structures of nematic molecules, the dielectric responses are dependent on the direction and frequencies of the applied field [23]. In nematics the dielectric permittivity is a tensorial quantity [2], and the value and sign of the dielectric anisotropy play an important role in display technologies employing nematic liquid crystals.

An external field when applied to a dielectric medium like liquid crystals induces a polarization, **P**, which is the dipole moment per unit volume. For small fields **P** is proportional to the electric field **E:**

$$\mathbf{P} = \varepsilon_0 \chi \mathbf{E}, \tag{1.3}$$

Where ε_0 is the permittivity of free space and χ is the second rank susceptibility tensor. If we assume that the director is along the z-axis, then the above equation can be written as:

$$\begin{pmatrix} P_x \\ P_y \\ P_z \end{pmatrix} = \varepsilon_0 \begin{pmatrix} \chi_\perp & 0 & 0 \\ 0 & \chi_\perp & 0 \\ 0 & 0 & \chi_\parallel \end{pmatrix} \begin{pmatrix} E_x \\ E_y \\ E_z \end{pmatrix} \tag{1.4}$$

The electric displacement is:

$$\mathbf{D} = \varepsilon_0 \mathbf{E} + \mathbf{P}, \tag{1.5}$$

or,

$$\mathbf{D} = \varepsilon_0 (1 + \chi)\mathbf{E} = \varepsilon \mathbf{E}, \tag{1.6}$$

where $\varepsilon = \varepsilon_0 \varepsilon_r$, and $\varepsilon_r = (1+\chi)$ is the relative permittivity of the material. Eqn. (1.7) can also be written in terms of the relative permittivity as:

$$\mathbf{P} = \varepsilon_0(\varepsilon_r - 1)\mathbf{E}. \qquad (1.7)$$

The Polarization **P** comes from two sources:

(i) The relative displacement of atoms and electronic charge caused by the electric field. This contribution is relatively small.

(ii) The permanent dipole moment μ of the molecules, when they possess a rotational freedom, which allows them to align along the applied field. Usually this contribution dominates the dielectric properties of LC molecular systems.

The dielectric constant or relative permittivity is also related to the capacitance by:

$$\varepsilon_r = C/C_0 \ , \qquad (1.8)$$

where C and C_0 are the capacitance of the filled and empty cell, respectively. Thus the determination of ε_r can be made by measuring the capacitance of the LC sample.

Nematic liquid crystals possess two principal components of the permittivity: $\varepsilon'_{\parallel}$ - for a field oscillating parallel to the optic axis, and $\varepsilon'_{\perp}$ - for field oscillating perpendicular to the optic axis. The dielectric anisotropy $\Delta\varepsilon'$ is then written as:

$$\Delta\varepsilon' = \varepsilon'_{\parallel} - \varepsilon'_{\perp} \ . \qquad (1.9)$$

The sign of the dielectric anisotropy may be positive or negative. A molecule has positive $\Delta\varepsilon'$ ($\varepsilon'_{\parallel} > \varepsilon'^{'}_{\perp}$) if the dipole moment is parallel to the long molecular axis

(which coincides with the optic axis). In this case the molecules tend to align along the field direction. If the dipole moment is more or less perpendicular to the molecular long axis, then $\Delta\varepsilon'$ is negative ($\varepsilon'_{\parallel} < \varepsilon'_{\perp}$) and the molecules align normal to the field direction. Thus the sign of $\Delta\varepsilon'$ dictates whether the molecules will align along the applied field or perpendicular to it.

When an electric field is applied to a system with a positive dielectric anisotropy, the liquid crystal molecules will realign themselves along the field direction in order to minimize the free energy density; or in other words, an applied field will cause distortion of the liquid crystal director. However, for any distortion to occur the strength of the applied field must be greater than a certain threshold. This threshold field is called the *Freedericksz* threshold and the transition from the uniform to the distorted state is called the *Freedericksz* transition. The threshold voltage V_{th}, which is independent of the cell thickness, is given by:

$$V_{th} = \pi \sqrt{\frac{K_{ii}}{\varepsilon_0 \Delta\varepsilon'}} , \qquad (1.10)$$

where K_{ii} is the elastic constant related to the corresponding deformation. For materials with positive $\Delta\varepsilon'$, the splay elastic constant K_{11} can be measured using a planar configuration. The director distortion above the threshold involves both K_{11} and K_{33}, and can also be used to determine K_{33}. This will be described further in Chapter 2.

1.6.3 Optical Properties

A nematic liquid crystal with uniaxial symmetry exhibits uniaxial optical symmetry with two principal refractive indices n_e and n_o; where, n_e and n_o are the ordinary and the extraordinary refractive indices for light with electric field polarization

parallel and perpendicular to the director, respectively [1]. Thus when light enters a NLC it is refracted into two components, fast (ordinary ray) and slow (extraordinary ray), each polarized with the vibration directions oriented perpendicular to each other

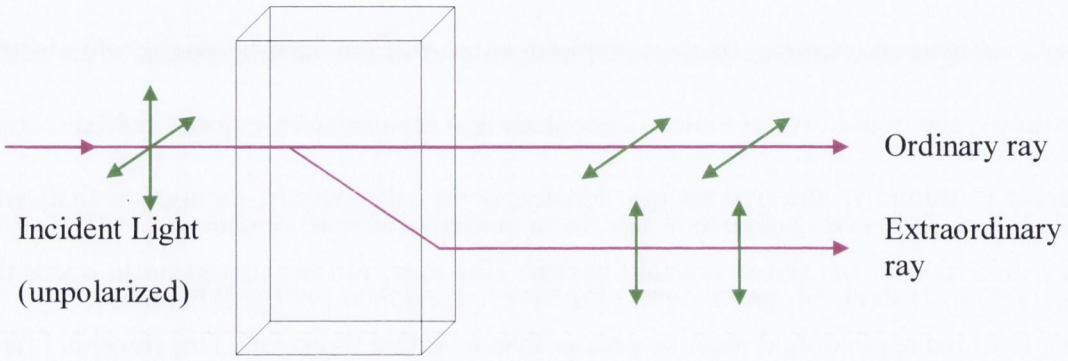

Figure 1.9: Schematic of Light travelling through a birefringent medium

and travelling at different velocities. The two independent refractive indices are quantified in terms of their optical anisotropy or birefringence, given by:

$$\Delta n = n_e - n_o . \qquad (1.11)$$

LCs have rather large birefringence, typically ranging from 0.10 to 0.15 [2]. Because of their dielectric anisotropy, the application of an electric field can reorient the director, resulting in a large electro-optical effect. This phenomenon is exploited in various LC applications.

Due to the different velocities at which the rays travel through the sample, the waves get out of phase. As a result of this phase difference, the polarization state of the incident light changes when the rays exit the birefringent material. Consequently, the LC sample acts as a retarder, with the retardation angle given by:

$$\delta = \frac{2\pi\Delta nd}{\lambda} \quad , \tag{1.12}$$

where λ is the wavelength of the incident light and d is the sample thickness. The length of the sample is an important parameter as the phase shift accumulates as long as the light travels in the birefringent material. With the right combination of birefringence and length, any polarization state can be produced.

Consider the case when a LC sample is placed between crossed polarizers whose transmission axis lies at an angle θ between the slow and fast axis of the material. Due to the birefringent nature of the material, the incoming linearly polarized light, given by

$$E_{incident} = \begin{pmatrix} E_x \\ E_y \end{pmatrix} = \begin{pmatrix} E_0 \cos\theta \\ E_0 \sin\theta \end{pmatrix} \tag{1.13}$$

becomes elliptically polarized:

$$E_{sample}(z) = \begin{pmatrix} E_x \exp(ik_e z) \\ E_y \exp(ik_o z) \end{pmatrix}, \tag{1.14}$$

where $k_{e,o}$ is the wave vector given by $k_{e,o}=n_{e,o}2\pi/\lambda$, with n being the refractive index.

Using the Jones calculus for optical polarizer, given by :

$$\hat{J} = \begin{pmatrix} \sin^2\theta & -\cos\theta\sin\theta \\ -\cos\theta\sin\theta & \cos^2\theta \end{pmatrix}, \tag{1.15}$$

We can obtain the light, emerging from the second polarizer, as:

$$E_{out} = \hat{J}E_{sample}(z = d) \tag{1.16}$$

$$= E_0 \sin(2\theta)\sin(\Delta kd/2)\exp[i(k_o + k_e)d/2]\begin{pmatrix} \sin\theta \\ \cos\theta \end{pmatrix}. \tag{1.17}$$

And the output intensity becomes,

$$I_{out} = |E_{out}|^2 = E_0^2 \sin^2(2\theta)\sin^2\left(\frac{\Delta kd}{2}\right) \tag{1.18}$$

$$= E_0 \sin^2(2\theta)\sin^2(\frac{\pi\Delta nd}{\lambda}). \tag{1.19}$$

1.6.4 Elasticity

In an undistorted monodomain sample of a nematic liquid crystal the director **n** is constant everywhere throughout the sample. When the sample is distorted due to an external perturbration an elastic restoring torque comes into play and tends to reinstate **n** to the undistorted state. The twist, bend and splay are the three principal director axis deformation in nematic liquid crystals and correspond to spatial changes in **n**(r) [23].

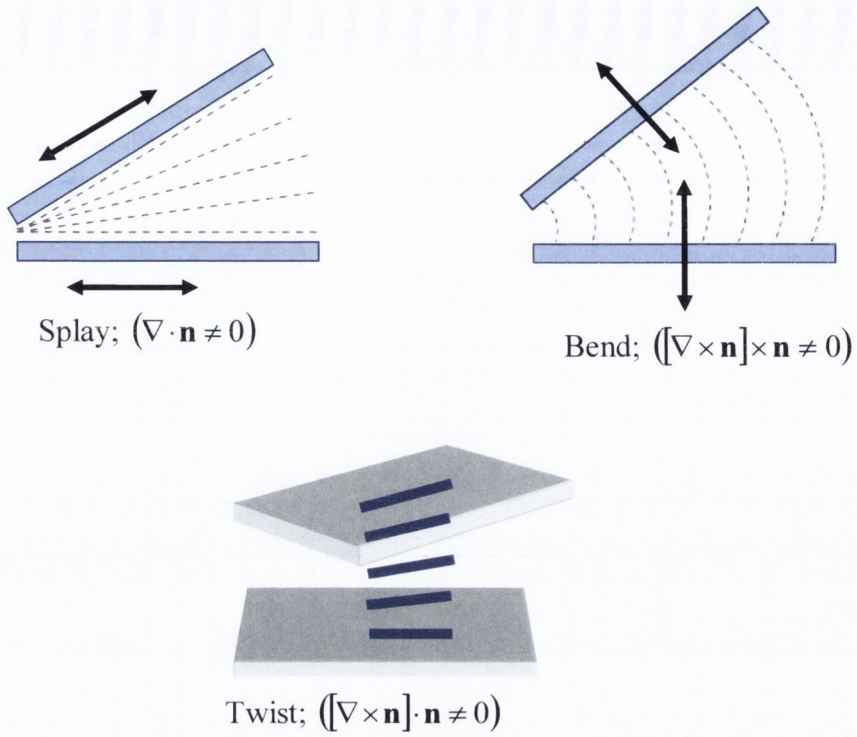

Figure 1.10: Schematic representation of Splay, Bend and Twist Deformations.

Following the theoretical formalism developed by Frank [24], the free energy densities associated with these deformations are given by:

$$splay : f_1 = \frac{1}{2} K_{11} [\nabla \cdot \mathbf{n}]^2, \tag{1.20}$$

$$twist : f_2 = \frac{1}{2} K_{22} [\mathbf{n} \cdot \nabla \times \mathbf{n}]^2, \tag{1.21}$$

$$bend : f_3 = \frac{1}{2} K_{33} [\mathbf{n} \times \nabla \times \mathbf{n}]^2, \tag{1.22}$$

where, K_{11}, K_{22} and K_{33} are the respective Franks splay, twist and bend elastic constants respectively. A schematic representation of these deformations is shown in Fig. 1.10

In general more than one form of deformation will be induced by an applied external field. If all three kinds of deformations are present, then the total free energy density of the deformations is proportional to the squares of the spatial derivatives of the director and can be written as:

$$F = \frac{1}{2}K_{11}[\nabla \cdot \mathbf{n}]^2 + \frac{1}{2}K_{22}[\mathbf{n} \cdot \nabla \times \mathbf{n}]^2 + \frac{1}{2}K_{33}[\mathbf{n} \times \nabla \times \mathbf{n}]^2. \quad (1.23)$$

The elastic constants are positive for most calamitic materials, with the order $K_{33}>K_{11}>K_{22}$ followed most generally [23]. In some liquid crystal materials, such as the bent-cores, this effect has been seen to be reversed, with $K_{33}< K_{11}$. The elastic constants for different LC systems will be explored in more details in Chapters 3 and 4 of this thesis.

1.6.5 Flexoelectricity

The flexolectric effect in liquid crystals was first predicted by Meyer [25] as a mechano-electrical phenomenon analogous to piezoelectricity observed in crystalline solids. Usually in the absence of director deformation, the packing of the molecules is such that the net polarization is zero. However, for molecules possessing permanent dipole moments and asymmetric shapes, such as the pear/drop or crescent/banana shape, a macroscopic polarization can be induced by splay and bend distortions of the director [see Fig. 1.11]. This is referred to as flexoelectric polarization P_f and the

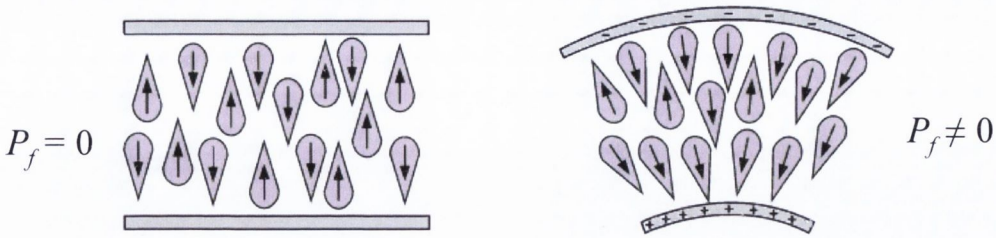

Figure 1.11: A nematic sample consisting of pear-shaped molecules with longitudinal dipole moments becomes polarized under splay deformation.

phenomenon itself is called flexoelectric effect. The flexoelectric polarization can be expressed in terms of the splay and bend flexoelectric coefficients as follows [25]:

$$P_f = e_1 \mathbf{n}(\nabla \cdot \mathbf{n}) - e_3 \mathbf{n} \times (\nabla \times \mathbf{n}). \qquad (1.24)$$

Here e_1 and e_3 are the flexoelectric coefficients corresponding to the splay and bend deformations, respectively. In this thesis, we follow Meyer's notation [25]. The size and sign of e_1 and e_3 are a molecular property. Alternatively, an electric field can align the dipole, inducing a splay- bend deformation in the appropriate shaped system - referred to as the converse flexoelectric effect.

Prost and Marcelou [26] proposed that flexoelectric effects can also arise in non-polar nematic LCs through the electric quadrupole mechanism. The splay or bend deformation could bring about a gradient in the quadrupole density, thereby generating a net bulk polarization (see Fig. 1.12).

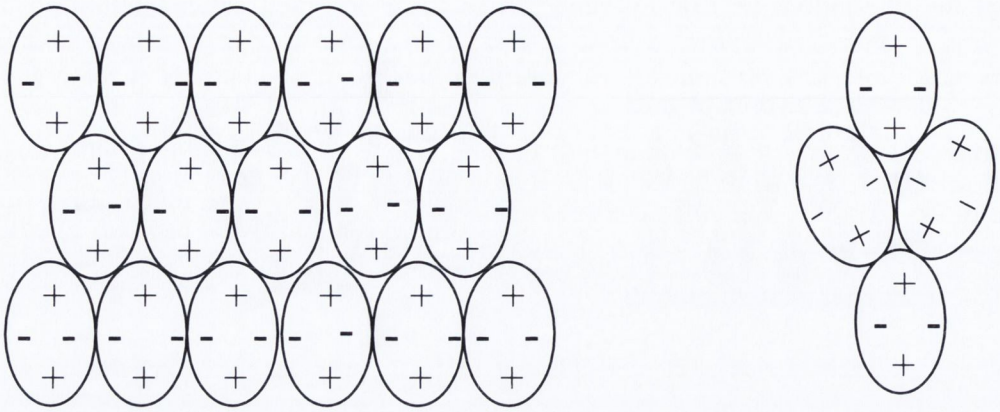

Figure 1.12: (a) A stack of quadrupoles; due to the symmetry of the arrangement of the quadrupoles, the bulk polarization is zero, (b) system becomes polarized when subjected to a splay distortion.

The flexoelectric polarization is difficult to obtain from direct methods involving distortion of the director as the screening of the polarization charges by ions present in the sample considerably affects the results. Therefore, usually the converse flexoelectric method is preferred, i.e., flexoelectric distortion of the director configuration using an external field; this technique measures the combination of the flexoelectric coefficient terms $(e_1 - e_3)$ and/or $(e_1 + e_3)$. The term $(e_1 - e_3)$is mainly determined by dipolar contributions and varies as S^2 for rigid molecular structures [27], while $(e_1 + e_3)$is related to quadrupolar effects and varies as S [26]. In some cases, when a uniform electric field is present only, the $(e_1 - e_3)$term contributes to the director torque, since an electric field gradient must be present in order to couple to the $(e_1 + e_3)$term [2]. This will be described later in Chapter 3.

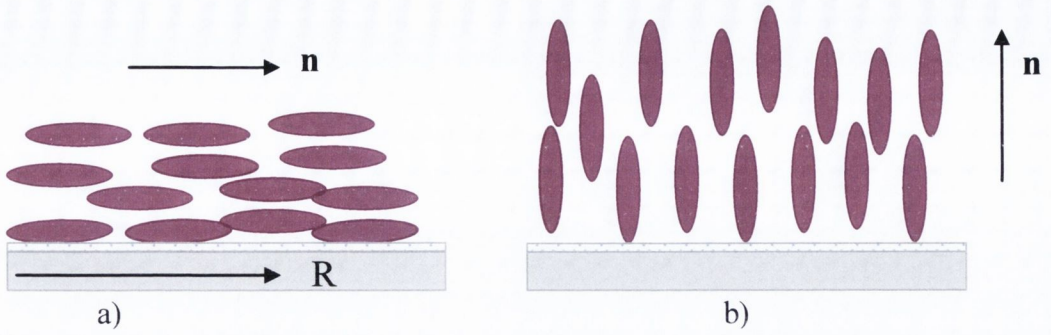

Figure 1.13: Schematic representation of (a) planar and (b) homeotropic alignment. R denotes the rubbing direction and **n** is the director.

1.7 Surface Alignment

In almost all applications based on liquid crystals, uniform orientation of the LC molecules is very important. Without uniform orientation the LC sample will have many domains, and hence many discontinuities. These multiple domains and discontinuities can cause scattering of light and cause a reduction in the image quality. Factors such as dipolar interactions, elasticity of the molecules, van der Waals interactions, steric factors, surface topology etc influence the alignment of the LC molecules on the substrates. There are two main types of LC director alignment at the free surface, known as planar and homeotropic alignment. In **planar alignment** (Fig. 1.13 (a)) the liquid crystal director is parallel to the surface of the substrate. This kind of alignment can be obtained by coating the surface with a thin polymer layer and then rubbing the substrate to obtain the desired director orientation. In **homeotropic alignment** (Fig. 1.13 (b)) the liquid crystal director is perpendicular to the substrate. A simple way of obtaining this alignment is by coating the substrate with a suitable polymer layer.

1.8 Aims and Objectives

The main aim of this thesis is to study the flexo-elastic and dielectric properties of various liquid crystalline systems. The main objectives are:

- To investigate the flexo-elastic properties of some bent core molecules and to study if their values are modified due to the presence of smectic-like clusters.
- To study the material parameters in the ordinary nematic phase of odd-bimesogens and investigate how these may influence the unusual properties exhibited by the second nematic phase present in these materials.
- To examine the dielectric properties of a dimesogen composed of a bent-core and rod-like unit.

1.9 Thesis Preface

Chapter 1 is a general introduction to Liquid Crystals, which briefly outlines the basic concepts such as the various molecular shapes, physical properties and mathematical expressions needed to realize the subject matter of this thesis.

Chapter 2 presents a brief introduction to the various experimental methods used to investigate the properties of the liquid crystals studied in this thesis.

Chapter 3 describes the flexo-elastic measurements carried out on some bent-core materials belonging to a homologous series. This study provides useful insight into how the material parameters behave in these classes of materials and in particular if the cybotactic clusters have any significant effect on the measured properties of the BCNs.

Chapter 4 presents the flexo-elastic measurements of a bimesogen that exhibits a second nematic phase at lower temperatures. These studies are particularly important as they could reveal useful information about how the material parameters change close to the nematic-nematic transition.

Chapter 5 deals with the experimental studies in some bimesogens that exhibit a second nematic phase (N_{tb}). A brief overview of the various properties exhibited by the lower temperature nematic phase is introduced. After which we describe the electro-optical effects observed close to the nematic-nematic interface in detail.

Chapter 6 focuses on the electro-optical and dielectric properties of a dimer material, composed of a bent-core and rod-like unit. A brief theoretical background of the dielectric properties is introduced. The experimental results are analyzed in terms of Maier-Meier model. A possible model of the arrangement of the molecules within a cluster is proposed based on the dielectric results and X-ray data.

Chapter 7 contains a summary of the results and general conclusion drawn from the work presented in this thesis.

References

[1] P.G. deGennes and J.Prost, *The Physics of Liquid Crystals*, 2nd ed., Oxford University Press, New York, USA, 1993.

[2] D. Dunmur, A Fukuda, G. R. Luckhurst, *Physical Properties of Liquid Crystals: Nematics*, Institution of Engineering and Technology, 2001.

[3] G. Gottarelli and G. P. Spada, *Mol. Cryst. Liq. Cryst.*, **123**, 377 (1985).

[4] S. Chandrasekhar, B. Sadashiva and K.A. Suresh, *Pramana*, **9**, 471 (1977).

[5] D. Vorländer, Ber. Dtsch. Chem. Ges. 62, 2831 (1929); D. Vorländer and A. Apel, *Ber. Dtsch. Chem. Ges.*, **65**, 1101 (1932).

[6] T. Niori, T. Sekine, J. Watanabe, T. Furukawa and H. Takezoe, *J. Mater. Chem.*, **6**, 1231 (1996).

[7] D. R. Link, G. Natale, R. Shao, J. E. Maclennan, N. A. Clark, E. Korblova, D. M. Walba, *Science,* **278**, 1924 (1997).

[8] H. Takezoe and Y. Takanishi, *Jap. J. App. Phys.*, **45**, 597 (2006).

[9] C. Keith, M. Prehm, Y. P. Panarin, J. K. Vij and C. Tschierske, *Chem. Commun.*, **46**, 372 (2010).

[10] G. Pelzl, S. Diele and W. Weisflogg, *Adv. Mater.*, **11**, 707 (1999).

[11] J. Extebarria and M.B. Ros, *J. Mater. Chem.*, **18**, 2919 (2008,).

[12] G. Liao, S. Stojadinovic, G. Pelzl, W. Weissflog, S. Sprunt, and A. Jakli, *Phys. Rev. E*, **72**, 021710 (2005).

[13] O. Francescangeli, V. Stanic, S. I. Torgova, A. Strigazzi, N. Scaramuzza,C. Ferrero, I. P. Dolbnya, T. M. Weiss, R. Berardi, L. Muccioli, S. Orlandi,and C. Zannoni, *Adv. Funct. Mater.*, **19**, 2592 (2009).

[14] C. Bailey, K. Fodor-Csorba, R. Verduzco, J. T. Gleeson, S. Sprunt, and A. Jákli, *Phys. Rev. Lett.*, **103**, 237803 (2009).

[15] A. de Vries, Mol. Cryst. Liq. Cryst., **10**, 219 (1970); A. de Vries, *J. Phys. Colloq.*,**36**, C1-1-C11 (1975).

[16] S. H. Hong, R. Verduzco, J. C. Williams, R. J. Twieg, E. DiMasi, R. Pindak, A. Jákli, J. T. Gleeson and S. Sprunt, *Soft Matter*, **6**, 4819 (2010).

[17] O. Francescangeli and E.T. Samulski, *Soft Matter*, **6**, 2413 (2010).

[18] M. Nagaraj, Y. P. Panarin, U. Manna, J. K. Vij, C. Keith and C. Tschierske, *Appl. Phys. Lett.*, **96**, 011106 (2010).

[19] Y. Jang, V. P. Panov, A. Kocot, A. Lehmann, C. Tschierske and J. K. Vij, *Phys. Rev. E*, **84**, 060701(R) (2011).

[20] D. Demus, J. Goodby, G.W. Gray, H.W. Speiss and V.Vill, *Handbook of Liquid crystals*, ed., Vol. 2A, Wiley-VCH: Weinheim Vol. 1, 1988.

[21] C.T. Imrie and P.A. Henderson, *Chem. Soc. Rev.*, **36**, 2096-124 (2007).

[22] K. L. Atkinson, S. M. Morris, F. Castles, M. M. Qasim, D. J. Gardiner, and H. J. Coles, *Phys. Rev. E.*, **85**, 012701 (2012).

[23] Iam-Choon Khoo, *Liquid Crystals*, 2nd ed., John Wiley & Sons, 2007.

[24] F.C. Frank, *Discuss. Faraday Soc.*, **25**, 19 (1958).

[25] R. B. Meyer, *Phys. Rev. Lett.*, **22**, 918 (1969).

[26] J. Prost and J.P Marcerou, *J. De. Phys.*, **38**, 315 (1977).

[27] I. Dozov, P. Martinot-Lagarde and G. Durand, *J. Phys. Lett.*, **44**, L817 (1983).

Chapter 2

Experimental Techniques

In this chapter, the various experimental methods used for the investigation of liquid crystal materials are discussed.

Contents

2.1 Introduction

In order to study the material properties of LCs presented in this thesis, various complimentary techniques were employed. Most of the techniques used in this thesis are commercially available, and detailed information of the various equipments used is listed below:

- **Optical Microscope**: Olympus BX-51, including objective lens (Olympus, LM PlanFI) and Leica DFC480 (Leica, digital camera for microscope), and Leitz Laborlux 12 POL S (microscope).

  - http://www.olympusfluoview.com/brochures/pdfs/bx51.pdf

  - http://www.leica-microsystems.com/

- **Photo-Elastic Modulator (PEM) system** for measuring retardation and birefringence: PEM-90 (HINDS Instruments)

  - http://www.hindsinstruments.com/PEM_Components/producys/default.aspx

- **Broadband dielectric spectrometer** for measuring the dielectric response: This system includes an Alpha-A impedance analyzer (Novocontrol GmbH, Impedance analyzer), Agilent 4291B RF Impedance/Material Analyzer and Quatro Cryosystem (Novocontrol GmbH, temperature controller). The system is controlled via a WINDETA (Novocontrol GmbH, software).

  - http://www.novocontrol.de/

  - http://home.agilent.com/agilent/home.jspx

- **Optical Spectrometer** for determining the cell thickness and optical pitch: Avaspec-2048 (Avantes, fast fiber optical spectrometer) and Lambda 900 UV/VIS/NIR spectrometer (PerkinElmer, broadband high resolution spectrometer).

- http://www.avantes.com
- http://perkinelmer.com/default.htm

The experimental techniques mentioned above are useful tools in the investigation of liquid crystalline properties. This chapter mainly focuses on providing detailed explanations of the methods used in the determination of the elastic constants, flexoelectric coefficients, X-ray diffraction patterns and dielectric spectroscopy.

2.2 Cell Construction

In most of the experiments, a mono-domain sample is investigated. In the case of LCs, the orientation of the director is generally random, and has to be constrained in one direction by an external force. The selected direction is usually obtained by providing suitable surface treatments to the glass-substrates used to confine the LCs.

Sandwich liquid crystal cells were prepared by using two indium tin oxide (ITO) glass plates with a sheet resistance of 20 Ω/□. The ITO film is thin enough to be practically transparent, and is also conductive. The ITO layer thus allows leads to be soldered, enabling the cell to be connected to a measuring circuit. To achieve necessary shape and size of the electrodes, the glass plates were etched in an acid mixture, using an appropriate mask.

In order to obtain planar alignment of the sample, the two etched glass substrates were spin-coated with a thin layer of polymer alignment layer RN1175 (Nissan Chemicals, Japan), and cured for one and a half hours at 250°C to evaporate the solvent and/or cause polymerization. The homeotropic alignment was achieved by coating the cells with the alignment agent AL60702 (JSR, Korea), and baking the glass plates at 220°C for 30 minutes. In case of the planar alignment it is necessary to provide a

selected direction in order to obtain a mono-domain sample. For this purpose, the polymer coated glass substrates were rubbed on a velvet track.

After depositing the alignment layers on the glass substrate, as described above, the cell was assembled (Fig 2.1). The cells for the homogeneous alignment were assembled in such a way that the rubbing directions on the top and bottom substrates were anti-parallel. The cell was sealed with epoxy or UV curing glue on both sides.

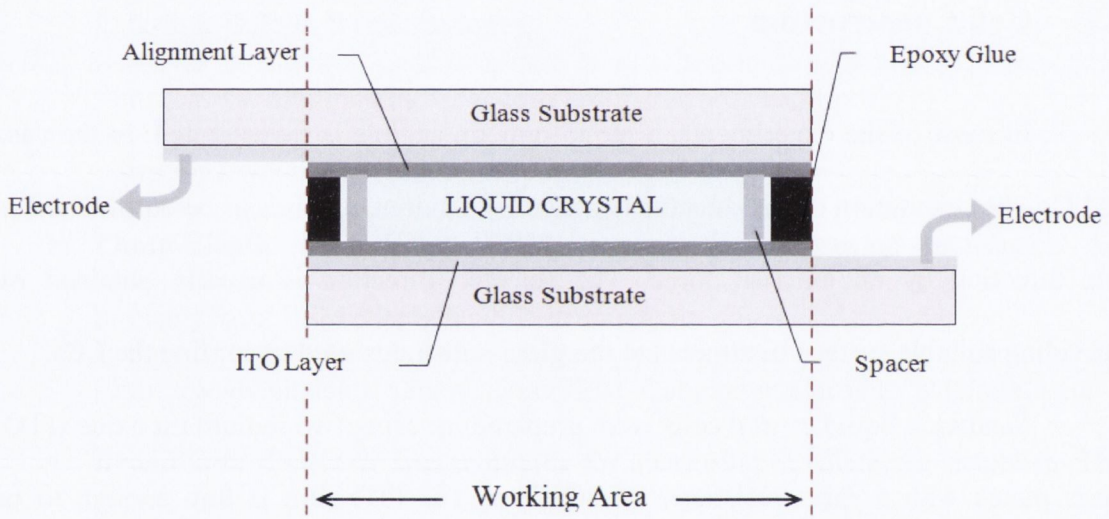

Figure 2.1: Sandwich liquid crystal cell

The capacitance of the empty cell was measured before filling it with the material. The sample was then filled via capillary action by heating the empty cells into the isotropic phase using a temperature controller (Eurotherm 2604).

In addition to homemade cells, commercial planar and homeotropic cells (EHC Co. Japan) of various thicknesses were also used in some of the experiments presented in this thesis.

2.2.1 Cell Thickness Measurement

Sample thickness is one of the critical parameters in the dielectric and flexoelectric measurements. Two methods were used to measure the cell thickness. In cases when the cell has electrodes, the thickness can be easily estimated by measuring the empty capacitance of the cell, and using the equation $C_0 = \varepsilon_0 A/d$, where C_0 is the capacitance of the empty cell, A and d are the area and cell thickness respectively, ε_0 = 8.85×10^{-12} F/m. The experimental error obtained for d using this technique is ~ 10-15%, and arises mainly due to error in the estimation of the electrode area.

The second method allows accuracy better than 10% and does not require the presence of electrodes. This technique is based on the measurements of the transmittance (absorbance) spectra, using an UV-visible Avantes-2048 fiber optical spectrometer. The spectrum of an empty cell produces interference fringes caused by refection from two close surfaces. The cell thickness can then be calculated using the formula:

$$d = \frac{\lambda_k \lambda_{k+n} n}{2(\lambda_{k+n} - \lambda_k)}. \qquad (2.1)$$

Where λ_k and λ_{k+n} are the wavelengths of two maxima (or minima) separated by n minima (or maxima) correspondingly.

2.3 Electro-Optical Technique

A typical electro-optical setup is presented in Fig. 2.3.1. This technique is based on the utilization of a polarizing microscope set-up to obtain information on the light transmitted through the cell in the presence/absence of an electric field, for different temperatures.

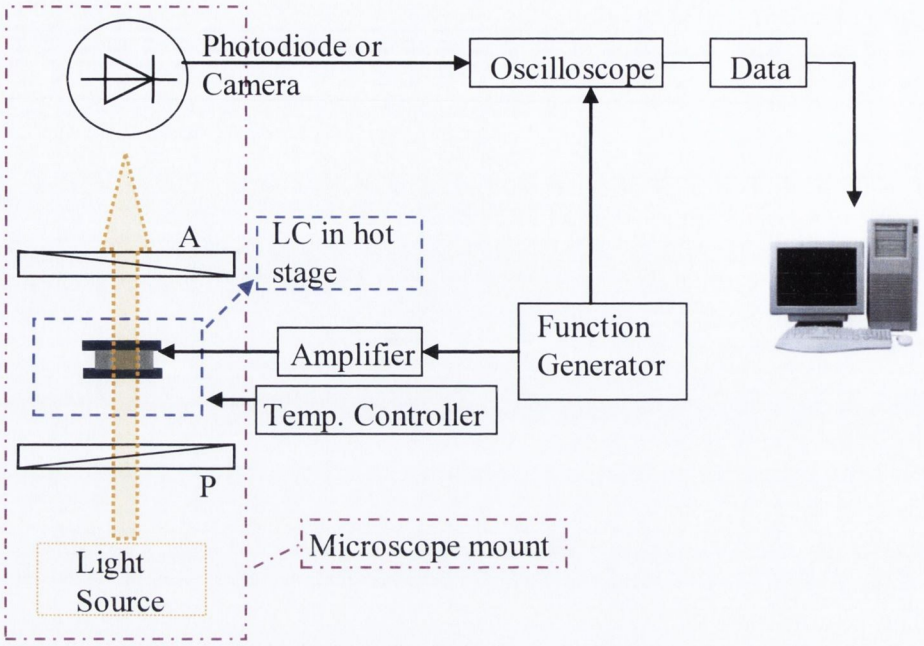

Figure 2.2: Schematic of the Electro-optical Set-up

The polarizing microscope (Olympus BX-51) by itself is used to observe/analyze the sample texture, and for capturing the images with a camera (Leica DFC 480) connected to a computer. The main difference from an ordinary optical microscope is that the presence of a pair of polarizers allows the investigation of the influence of the sample on the plane of polarization of the transmitted light. The intensity of the transmitted light is measured by the photo-diode, and the output signal is recorded on a digital oscilloscope (Tektronix TDS 2014). A waveform generator (Agilent 33120A) is used to apply an electric field to the liquid crystal cell. The liquid crystalline temperature is controlled by a temperature-controller (Eurotherm 2604), connected to a PC.

The electro-optical set-up was used for the preliminary investigation of the LCs including phase transitions, electric field effects etc, as well as for measurement of spontaneous polarization and tilt of the optic-axis of cholesteric LC materials.

2.3.1 Measurement of Spontaneous Polarization

The schematic for the system used for measuring the field induced polarization of a liquid crystal is shown in Fig. 2.3. A rectangular waveform of alternating voltage is applied to the LC cell. The current i flowing through the liquid crystal cell is integrated by a capacitor C_1 connected in series with the cell and a voltage generator.

For simplicity, let us assume that the LC is in the smectic phase and the smectic layers are oriented perpendicular to the electrodes. For a voltage U applied to the electrodes of the cell, the polarization vector tends to lie in the direction of the electric field **E**, while the azimuthal angle φ between them tends to zero. In the process of the reorientation of the polarization P_s, there occurs a repolarization current i_p which is associated with the change in the surface charge on the electrodes [1, 2]. Additionally, a current i_r associated with the ionic conduction also passes through the LC cell. The third component is the displacement current i_c, which is related to the recharging of the cell capacitance. Consequently, the instantaneous value of the current through the cell can be presented as:

$$i = i_r + i_c + i_p = \frac{U}{R} + C\frac{dU}{dt} + A\frac{dP_s}{dt}, \qquad (2.2)$$

where C is the capacitance of the cell, A and R represent the area and resistance of the cell respectively, and U is the applied voltage across the cell.

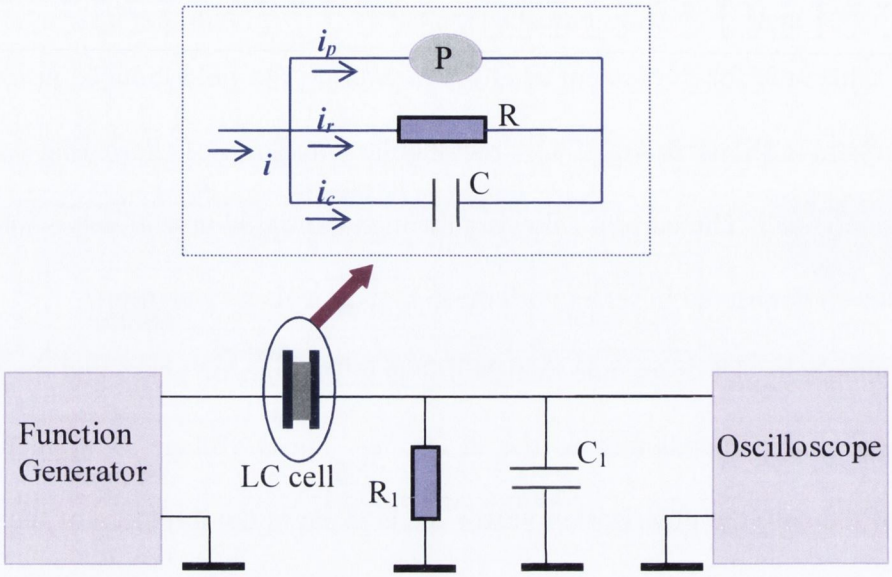

Figure 2.3: Schematic of the Polarization Measurement System

The instantaneous value of the voltage across the capacitor C_1 is:

$$U_{out} = -\frac{1}{C_1}\int_0^t idt \qquad (2.3)$$

$$= \frac{U}{RC_1}t + \frac{2UC}{C_1} + \frac{P_s A}{C_1}\cos(\varphi(t)) = U_r + U_c + U_p \,, \qquad (2.4)$$

where $t = 0$ represents the instant of reversing the sign of the electric field across the cell. A typical example of the output voltage across the capacitor C_1 is shown in Fig. 2.4.

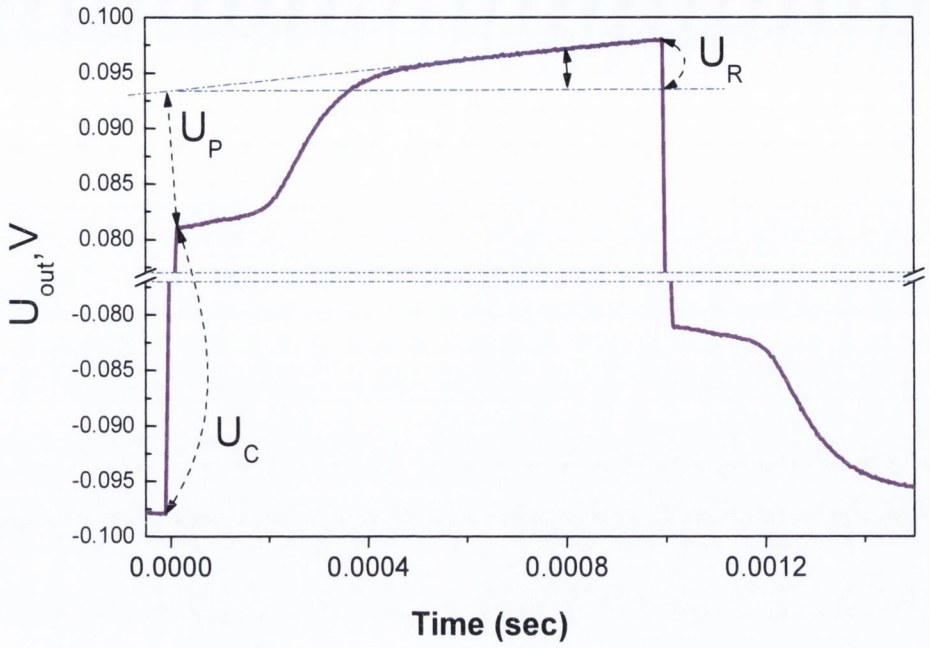

Figure 2.4: Oscillogram for the output signal from capacitor C_1. Image courtesy [3].

Here U_{out} is given as the sum of three components corresponding to the current though resistive part (U_r), voltage due to the recharging of the cell capacitance (U_c) and the voltage across C due to the repolarisation current (U_p). The function generator time constant is much shorter than the oscilloscope sweep time; hence the oscillogram depicts U_c as an instantaneous jump. This is followed by a smooth growth in the voltage due to integration of the repolarization (i_p) and conductivity current (i_r). In order to eliminate the effect of i_r, a variable resistor R_1 can be introduced into the measuring circuit as shown in Fig. 2.3. By measuring the value of U_p, the polarization can be determined using the formula:

$$P_S = \frac{U_p C_1}{2A}. \tag{2.5}$$

2.4 Broadband Dielectric Spectroscopy Equipment

The dielectric spectrometer measures the impedance spectrum $Z^*(\omega)$ of a material arranged between the electrodes. The intrinsic electrical properties of the material such as the complex permittivity $\varepsilon^*(\omega)$ or conductivity $\sigma^*(\omega)$ are then evaluated from $Z^*(\omega)$. In addition to the measurement of the temperature and frequency dependence of $Z^*(\omega)$, the effects of a DC bias and AC field strength applied across the sample can also be determined.

The dielectric properties of the LC materials mentioned in this thesis were mostly studied using a **Novocontrol Alpha-A dielectric analyzer** (set-up shown in Fig. 2.5). The system functions are controlled via the Novocontrol WINDETA software connected to the Alpha-A analyzer main frame.

Figure 2.5: Novocontrol Alpha-A Dielectric Spectrometer Set-Up.

The **Low frequency Alpha A (<20 MHz)** measurement system has test interfaces for nearly all materials including special application ranges, such as

impedance: 0.001 to $10^{15}\Omega$ and tan (δ) $>3X10^{-5}$. It also supports a series of high performance test interfaces with special functionality such as integrated active sample cell, 4-wire impedance measurements, high voltage/current measurements and potentiostat and galvanostat functions for electro chemical applications.

(**RF impedance analyzer**): At frequencies above 10 MHz electrical wave effects become prominent and microwave techniques have to be applied. Typical operating ranges of RF-impedance analyzers are, frequency: 1 to 3 GHz, Impedance: 0.1 to 10^5 Ω and tan(δ) > $3x10^{-3}$. This method is particularly convenient for dielectrics with sufficient relaxation strengths and for conductive samples like semiconductors and electrolytes.

2.4.1 Principle of Dielectric Measurements

The basic operation of the dielectric measurements is to create a sinusoidal wave at a frequency of interest and apply it to the sample (Figure 2.6).

$$U(t) = U_0 \cos(\omega t). \tag{2.6}$$

The resulting current is

$$I(t) = I_o \cos(\omega t + \varphi) = \mathrm{Re}[I^*(\omega)\exp(i\omega t)]. \tag{2.7}$$

i.e., there will be a phase shift between the current and voltage described by the angle φ. From this, the amplitude (I_0) and phase angle (φ) of the current harmonic wave component $I^*(\omega)$ are calculated by the complex Fourier Transform of $I(t)$ as follows:

The Fourier transform of eqn. (2.7) over m periods is

$$I(\omega) = I' + iI'' = \frac{2}{mT}\int_0^{mT} I(t)\exp(i\omega t)dt, \tag{2.8}$$

$$I_0 = \sqrt{(I')^2 + (I'')^2}\ ; \quad \tan(\varphi) = \frac{I''}{I'} \tag{2.9}$$

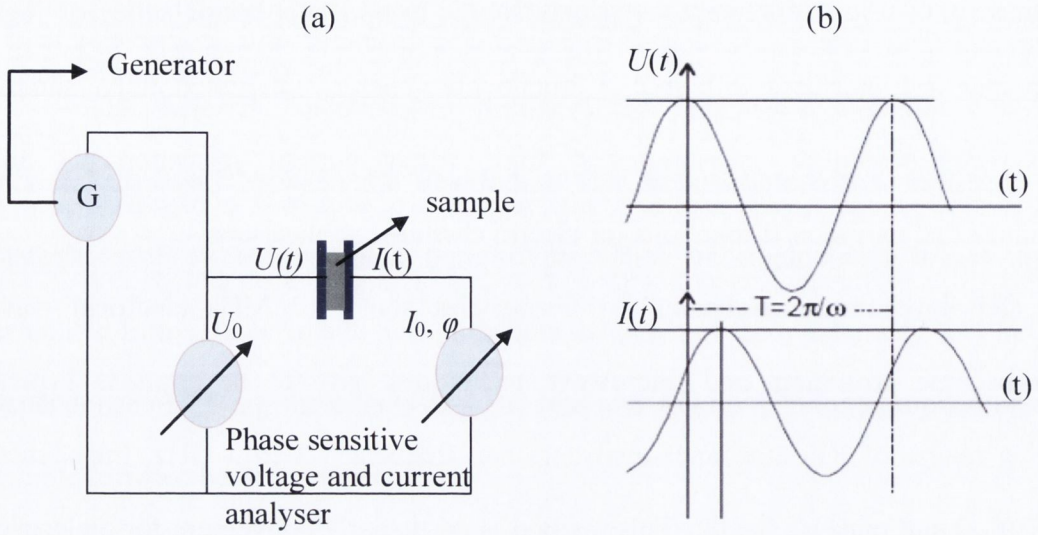

Figure 2.6: (a) Principle of dielectric measurement, (b) Amplitude and phase relation between current and voltage of a sample capacitor for dielectric measurements.

All frequency components in $I(t)$ except a narrow band centered on the generator frequency is compressed by the Fourier transform. This helps to reduce the DC noise and drift, and improves the accuracy of the measurements. The impedance and other material parameters are then calculated as:

Impedance,

$$Z^*(\omega) = Z' + iZ'' = \frac{U_O}{I^*(\omega)}, \tag{2.10}$$

Permittivity,

$$\varepsilon^*(\omega) = \varepsilon' - i\varepsilon'' = \frac{-i}{\omega Z^*(\omega)} \frac{1}{C_0}, \tag{2.11}$$

Conductivity,

$$\sigma^*(\omega) = \sigma' - i\sigma'' = \frac{-i}{Z^*(\omega)} \frac{d}{A}, \tag{2.12}$$

where C_0 is the capacitance of the empty cell, d is the electrode spacing and A is the electrode area.

2.5 X-ray diffraction studies

X-ray diffractometry (XRD) is an important tool to determine the mesophases of the LC material and the molecular packing. A typical X-ray set-up is shown in Fig. 2.7.

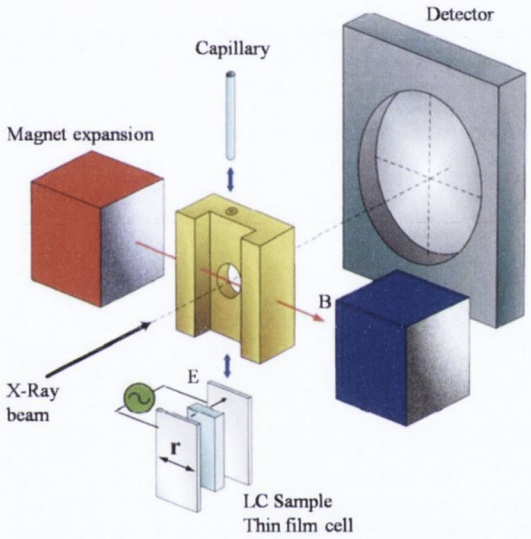

Figure 2.7: Schematic representation of the XRD set-up. Reprinted from ref. [4].

The basic principal behind XRD is Bragg's law (depicted in Fig. 2.8) where, X-rays reflected from adjacent crystal lattice undergoes constructive interference only when the path difference between them is an integral multiple of the X-ray's wavelength. Bragg's law is given by:

$$2d\sin\theta = n\lambda, \tag{2.13}$$

where d is the separation between the planes, θ is the angle of incidence, n is an integer and λ is the wavelength.

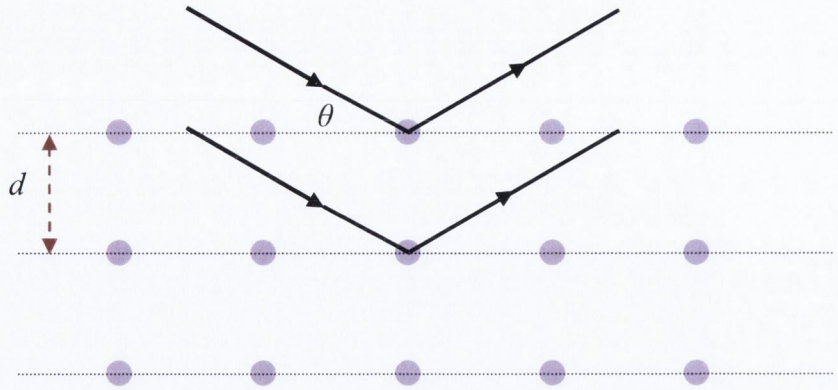

Figure 2.8: Illustration of Bragg's Law.

Bragg's law shows an inverse relation between the separation of the planes and the diffraction angle; however it provides no information about the intensities of the various peaks. The total scattered intensity is independent of the positional order, and depends only on the total number of scattering centers, consisting of any periodic distribution of electron density, and their scattering power. When an X-ray beam with an initial wave vector k_i, whose direction specifies the direction of propagation and modulus $|k_i| = 2\pi/\lambda$, is scattered, the wave vector k_i changes to k_f with a momentum transfer. Since the scattering is elastic (no change in energy), the magnitudes of the wave vectors are equal. By the de Broglie relation, the scattering vector is defined by $Q = k_f - k_i$. Its modulus is given by:

$$|Q| \equiv Q = \frac{4\pi \sin\theta}{\lambda}. \tag{2.14}$$

And the equivalent statement of Bragg's law is:

$$Q_n = n\left(\frac{2\pi}{d}\right). \tag{2.15}$$

The diffracted intensity is hence most conveniently plotted as a function of the scattering vector. For a system containing N molecules, the total scattered intensity at a

point is expressed by the product of the form factor $F(\vec{q})$ and the structure factor $S(\vec{q})$. The form factor is determined by the molecular structure of the mesogens and depends only on the single particle distribution function, while the structure factor includes both orientational and spatial correlations. The total intensity is given as:

$$I(Q) = F(\vec{q}) \times S(\vec{q}) \tag{2.16}$$

In order to observe a particular diffraction peak, the planes must be aligned at an angle θ_n to the incident beam. The LC sample can be aligned by either a magnetic field for the material in a glass capillary or an electric field applied across a LC thin film in the planar cell configuration. Examples of scattering from N, Sm*A* and Sm*C* phases are shown in Fig. 2.9.

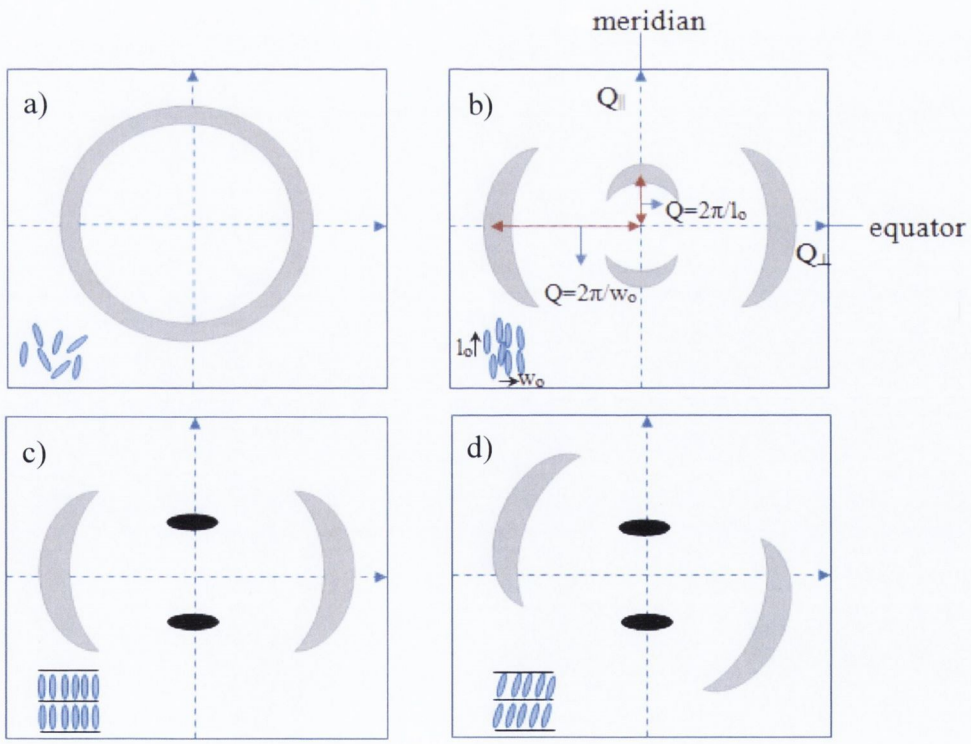

Figure 2.9: Schematic representation of 2D X-ray diffraction patterns of different types of LC phases: (a) Isotropic, (b) Aligned nematic, (c) Smectic-*A* and (d) Smectic-*C*; $Q_{\parallel}$ and $Q_{\perp}$ are the wave vector components in the direction collinear and normal to **n**.

The isotropic phase is characterized by the absence of long range orientational or positional order. The isotropic state cannot be aligned; hence its diffraction pattern consists of weak, diffuse rings (Fig. 2.9(a)). For an aligned nematic LC sample the XRD patterns consists of two sets of diffuse arcs (Fig. 2.9(b)). The intensity of these arcs is indicative of the extent of alignment within the sample; generally represented by the order parameter, *S*. As the sample is cooled down to the smectic-*A* phase, two sets of diffuse peaks are seen in diffraction pattern (Fig. 2.9(c)); the diffuse peaks at small angles condense into sharp quasi-Bragg peaks. In smectic-*C* phases, where the molecules are tilted with respect to the layer normal, the diffuse peaks at smaller and larger angles are no longer orthogonal to each other (Fig. 2.9(d)).

2.6 Determining K_{11} and K_{33} using *Freedericksz* Transition Technique

The setup used for determining the elastic constants consists of a photoelastic modulator (HINDS Instruments PEM-90), microscope, waveform generator, helium-neon laser and two lock-in amplifiers (Fig. 2.10). The setup measures the retardation as a function of the applied voltage from which both K_{11} and K_{33} can be estimated from a single homogeneously aligned cell for materials with positive $\Delta\varepsilon'$.

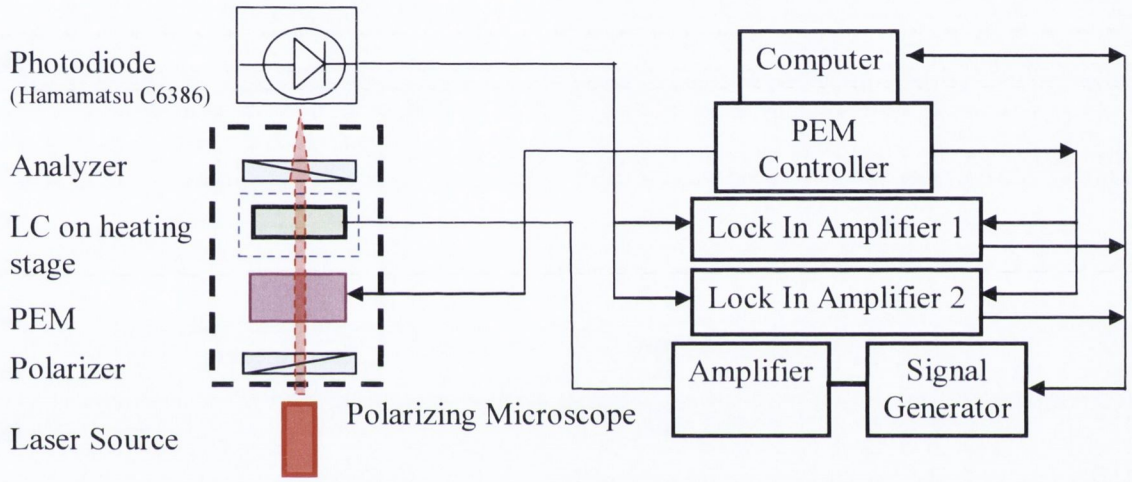

Figure 2.10: PEM Setup

The simplest method to determine the elastic constants is by applying a field perpendicular to the director of the well aligned sample. Above a certain threshold field, the director orientation starts distorting and this called *Freedericksz* transition [5]. There are three possible geometries for measuring all three elastic constants. However, in this thesis we determine both the splay and bend elastic constants for materials with positive $\Delta\varepsilon'$ using a planar cell configuration. The threshold voltage (V_{th}) required to distort the director field was used to calculate the splay elastic constant. The analysis of the director distortion at higher fields was used to determine the bend elastic constant. In order to measure K_{22} a twisted nematic cell or cell with in-plane electrodes is required

as an electric field applied across the substrates of a conventional planar cell does not induce a twist deformation.

For a liquid crystal that is enclosed between two conducting glass plates separated by a distance *d*, let us assume that the plates lie in the x-y plane; with director **n** parallel to the x-axis. For a LC with positive $\Delta\varepsilon'$ if an electric field **E** is applied across the cell, along the z-axis, the dielectric energy is lowered by tilting of the director (Fig. 2.11). In most cases, the director is anchored on both surfaces with a pre-tilt angle $\phi(0) = \phi(d)$. The tilt angle $\phi(z)$ varies along the cell gap and reaches a maximum value ϕ_m at $z = d/2$.

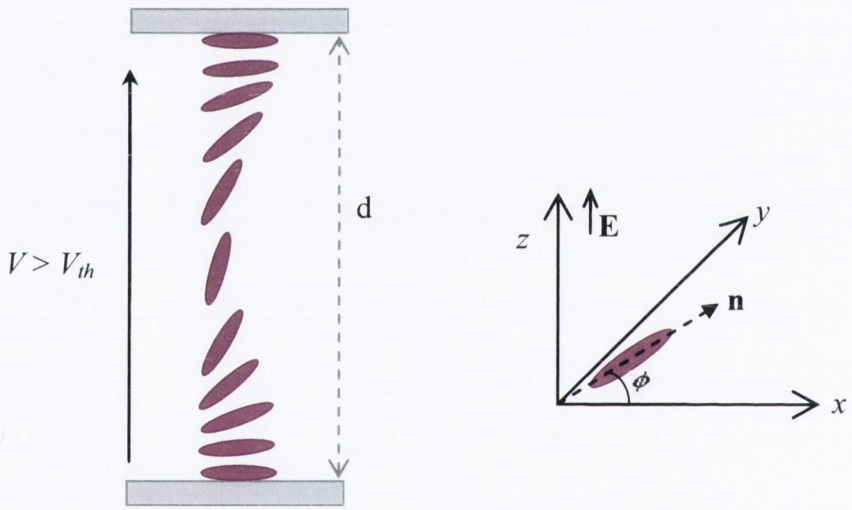

Figure 2.11: Distribution of the director field for an applied electric field greater than the threshold voltage.

Depending on the surface anchoring and pre-tilt angle four boundary conditions are possible: (i) infinite surface anchoring energy and zero pretilt angle at the surfaces; here the angle at the surfaces are independent of the applied field, ($\phi(0) = \phi(d) = \phi_0 = 0$), (ii) Zero pretilt but finite anchoring energy, (iii) Non-zero pretilt but infinite anchoring energy, (iv) Non-zero pretilt and finite anchoring energy. A perfect *Freedericksz* threshold voltage is usually obtained only with the first boundary condition.

Now, the director and electric field varies along the z-axis as:

$$\mathbf{n} = (\cos\phi(z), 0, \sin\phi(z)), \tag{2.17}$$

$$\mathbf{E} = (0, 0, E(z)). \tag{2.18}$$

The total free energy per unit of the cell is given as [6]

$$G = \frac{1}{2}\int_0^d [K_{11}\cos^2\phi + K_{33}\sin^2\phi\left(\frac{d\phi}{dz}\right)^2 - \mathbf{E}\cdot\mathbf{D}]dz + 2f_s(\phi_0). \tag{2.19}$$

Here the terms within the integrand are due to the elastic and dielectric energy densities respectively; the sum of these terms is denoted by g later on in the analysis. The second term is the Rapini Papoular [7] form of the surface energy

$$f_s(\phi_0) = \frac{1}{2}W_s\sin^2(\phi_0 - \phi_t) \quad \text{at} \quad z = 0, d \ , \tag{2.20}$$

where W_s is the surface anchoring strength and ϕ_0 is the actual tilt angle at the surface. Assuming there are no free ions in the LC, and $\mathbf{E}$ satisfies the Maxwell's equations [6], $\nabla\cdot\mathbf{D} = 0$ and $\nabla\times\mathbf{E} = 0$. This implies that the z-component (D_z) of the displacement vector is a constant; by symmetry $\mathbf{E}$ will only have a component along the z-direction, but its magnitude will be a function of z [8]. D_z can also be written in form of the voltage V ($=\int_0^d E(z)dz$) as [8]:

$$D_z = \frac{\varepsilon_0 V}{\int_0^d \left(\varepsilon_{\|}\sin^2\phi + \varepsilon_{\perp}\cos^2\phi\right)^{-1} dz}. \tag{2.21}$$

The dielectric energy per unit area is expressed as:

$$-\frac{1}{2}\int_0^d \mathbf{E}\cdot\mathbf{D}\,dz = -\frac{1}{2}D_z\int_0^d E(z)dz = -\frac{1}{2}\frac{\varepsilon_0 V^2}{\int_0^d \left(\varepsilon_{\|}\sin^2\phi + \varepsilon_{\perp}\cos^2\phi\right)^{-1} dz}. \tag{2.22}$$

Equation (2.19) can be re-written as

$$G = \frac{1}{2}\int_0^d [(K_{11}\cos^2\phi + K_{33}\sin^2\phi)\left(\frac{d\phi}{dz}\right)^2]dz - \frac{1}{2}\varepsilon_0 V^2 \left\{\int_0^d \frac{dz}{(\varepsilon_{\parallel}\sin^2\phi + \varepsilon_{\perp}\cos^2\phi)}\right\}^{-1} + 2f_s(\phi_0). \tag{2.23}$$

Minimizing the free energy leads to the Euler-Lagrange equation [9]:

$$\frac{d}{dz}\left(\frac{\partial g}{\partial \phi'}\right) - \left(\frac{\partial g}{\partial \phi}\right) = 0, \tag{2.24}$$

here g (integrand part) is the bulk free energy density and $\phi' = d\phi/dz$. The Euler-Lagrange Eqn. results in the following relation:

$$\frac{d}{dz}\left[(K_{11}\cos^2\phi + K_{33}\sin^2\phi)\left(\frac{d\phi}{dz}\right)^2 - \frac{D_z^2}{\varepsilon_0(\varepsilon_{\parallel}\sin^2\phi + \varepsilon_{\perp}\cos^2\phi)}\right] = 0. \tag{2.25}$$

By using the boundary condition $\phi(0) = \phi(d) = \phi_0$, i.e., assuming that a finite pre-tilt is present, and the maximum distorted angle of the director field at the center of the cell $\phi(d/2) = \phi_m$ (see Fig. 2.11, where $d\phi/dz = 0$) we obtain:

$$\frac{d\phi}{dz} = D_z\sqrt{\frac{\gamma}{\varepsilon_0\varepsilon_{\perp}K_{11}}}\left[\frac{\sin^2\phi_m - \sin^2\phi}{(1+\gamma\sin^2\phi_m)(1+\kappa\sin^2\phi)(1+\gamma\sin^2\phi)}\right]^{\frac{1}{2}}, \tag{2.26}$$

where $\kappa = \dfrac{K_{11}-K_{33}}{K_{11}}$ and $\gamma = \dfrac{\varepsilon_{\parallel}-\varepsilon_{\perp}}{\varepsilon_{\perp}}$.

Integrating over half the cell thickness, which is sufficient because of the symmetry of distortion, we obtain:

$$D_z = \frac{2}{d}\sqrt{\frac{\varepsilon_0\varepsilon_{\perp}K_{11}}{\gamma}}\sqrt{(1+\gamma\sin^2\phi_m)}\int_{\phi_0}^{\phi_m}\left[\frac{(1+\kappa\sin^2\phi)(1+\gamma\sin^2\phi)}{(\sin^2\phi_m - \sin^2\phi)}\right]^{\frac{1}{2}}d\phi \ . \tag{2.27}$$

By substituting $\sin\phi = \sin\phi_m \sin\psi$ and utilizing the value of D_z, we obtain the following expression for the applied voltage:

$$\frac{V}{V_{th}} = \frac{2}{\pi}\sqrt{(1+\gamma\sin^2\phi_m)}\int_{\Theta}^{\pi/2}\left[\frac{(1+\kappa\sin^2\phi_m\sin^2\psi)}{(1+\gamma\sin^2\phi_m\sin^2\psi)(1-\sin^2\phi_m\sin^2\psi)}\right]^{\frac{1}{2}}d\psi \ , \quad (2.28)$$

where $\Theta = \sin^{-1}(\sin\phi_0/\sin\phi_m)$, γ = ($\varepsilon'_{\parallel}$ / $\varepsilon'_{\perp}$) -1, and

$$V_{th} = \pi\sqrt{\frac{K_{11}}{\varepsilon_0\varepsilon_{\perp}\gamma}} = \pi\sqrt{\frac{K_{11}}{\varepsilon_0\Delta\varepsilon'}} \ , \quad (2.29)$$

where V_{th} is the threshold voltage and $\Delta\varepsilon'$ is the dielectric anisotropy defined as $\varepsilon'_{\parallel} - \varepsilon'_{\perp}$.

Now, the torque balance condition at the surface is given by:

$$\left(\frac{\partial g}{\partial \phi'}\right)_{z=0,d} = \left(\frac{\partial f_s}{\partial \phi}\right)_{z=0,d} , \quad (2.30)$$

where, $\phi' = d\phi/dz$. On simplifying this equation we get:

$$\left(K_{11}\cos^2\phi_0 + K_{33}\sin^2\phi_0\right)\left(\frac{d\phi}{dz}\right)_0 = \frac{1}{2}W_s\sin 2(\phi_0 - \phi_t), \quad (2.31)$$

where at the surface:

$$\left(\frac{d\phi}{dz}\right)_0 = D_z\sqrt{\frac{\gamma}{\varepsilon_0\varepsilon_{\perp}K_{11}}}\left[\frac{\sin^2\phi_m - \sin^2\phi_0}{(1+\gamma\sin^2\phi_m)(1+\kappa\sin^2\phi_0)(1+\gamma\sin^2\phi_0)}\right]^{\frac{1}{2}} , \quad (2.32)$$

By using the value of $(d\phi/dz)_0$ and the boundary condition $\phi' = 0$ at $z = d/2$, we obtain:

$$W_s = \frac{4K_{11}\mathrm{I}}{d\sin 2(\phi_0 - \phi_t)}\left[\frac{(1+\kappa\sin^2\phi_0)(\sin^2\phi_m - \sin^2\phi_0)}{1+\gamma\sin^2\phi_0}\right]^{\frac{1}{2}}, \quad (2.33)$$

where

$$\mathrm{I} = \int_{\Theta}^{\frac{\pi}{2}}\left[\frac{(1+\kappa\sin^2\phi_m\sin^2\psi)(1+\gamma\sin^2\phi_m\sin^2\psi)}{(1-\sin^2\phi_m\sin^2\psi)}\right]^{\frac{1}{2}}d\psi . \quad (2.34)$$

For an applied voltage, the optical phase difference is given by

$$\delta = \frac{2\pi}{\lambda}\int_0^d [n_{eff}(z) - n_o]dz, \tag{2.35}$$

where $n_{eff}(z) = n_e n_o / \sqrt{(n_e^2 \sin^2\phi + n_o^2 \cos^2\phi)}$ is the effective extraordinary index at z. By changing the variable from z to ϕ, and by using Eqn. (2.26) in Eqn. (2.35), we obtain:

$$\delta(V) = 2\pi \frac{n_e d}{\lambda}\left[\frac{\int_\Theta^{\frac{\pi}{2}} \sqrt{\frac{(1+\gamma\sin^2\phi_m\sin^2\psi)(1+\kappa\sin^2\phi_m\sin^2\psi)}{(1-\sin^2\phi_m\sin^2\psi)(1+\nu\sin^2\phi_m\sin^2\psi)}}\, d\psi}{\int_\Theta^{\frac{\pi}{2}} \sqrt{\frac{(1+\gamma\sin^2\phi_m\sin^2\psi)(1+\kappa\sin^2\phi_m\sin^2\psi)}{(1-\sin^2\phi_m\sin^2\psi)}}\, d\psi} - \frac{n_o}{n_e}\right], \tag{2.36}$$

where $\nu = (n_e^2/n_o^2) - 1$ and $\kappa = (K_{33}/K_{11}) - 1$.

In the experiment, n_e and n_o is estimated by recording the light intensity as a function of the wavelength using a UV-visible spectrometer (section 2.2.1) for light polarized parallel and perpendicular to the optic axis, respectively and by utilizing the equation [10]: $n_{e,o} = \frac{\lambda_k \lambda_{k+n} n}{2d(\lambda_{k+n} - \lambda_k)}$. The birefringence ($\Delta n$) value is evaluated from the retardation data using the relation $\delta = 2\pi\Delta n d/\lambda$, where λ (= 632.8nm) is the wavelength of the laser source. K_{11} is evaluated by using the threshold voltage V_{th} for *Freedericksz* transition (obtained from the retardation data $\delta(V)$) in equation (2.29); V_{th} is determined from the intersection of the linear ($V > V_{th}$) and curved ($V < V_{th}$) part of the $\delta(V)$ plot, as demonstrated in Fig. 2.12 for the bent-core material C7, as an example. The bend elastic constant, K_{33} is obtained for a fixed temperature from the theoretical fit of the retardation data above the threshold voltage to the parametric equations (2.28)

and (2.36) by an iterative procedure with κ and v as adjustable parameters. The iterative fitting program was written using the MATLAB software.

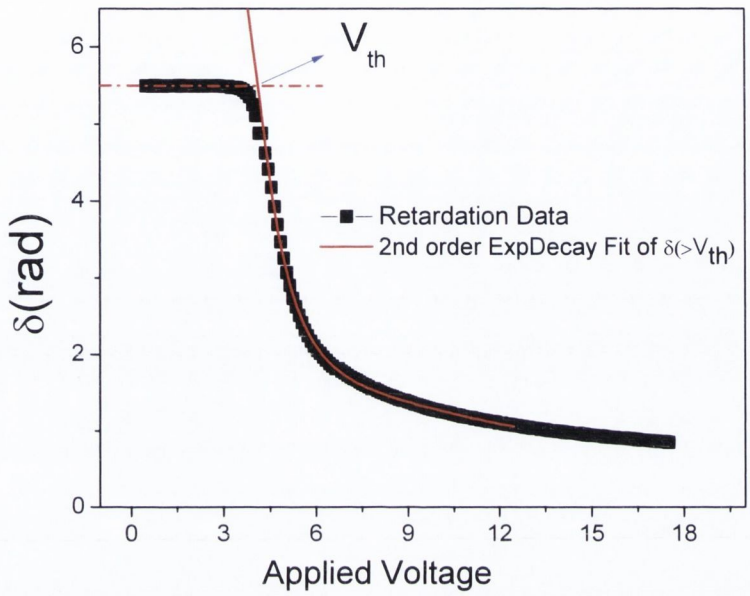

Figure 2.12: Retardation as a function of applied voltage for the material C7 at reduced temperature $T\text{-}T_{NI}$ = - 5°C. The threshold voltage V_{th} is estimated from the intersection of the linear (red dash-dot line; $V < V_{th}$) and curved (solid red line, $V > V_{th}$) part of the plot; solid red line represents the interpolated second order exponential fit of the retardation data at voltages >> V_{th}. The exponential fit has no relation to the actual evaluation of the elastic constants, but was done for the ease of determination of V_{th}.

2.7 Measurement of Effective Flexoelectric Coefficients

The flexoelectric effect in a chiral doped sample was first demonstrated by Patel and Meyer in 1987 [11], wherein flexoelectric polarization induces a tilt in the optic axis when an electric field is applied perpendicular to the cholesteric liquid crystalline helix axis. The basic principal of this effect is demonstrated in Fig. 2.13.

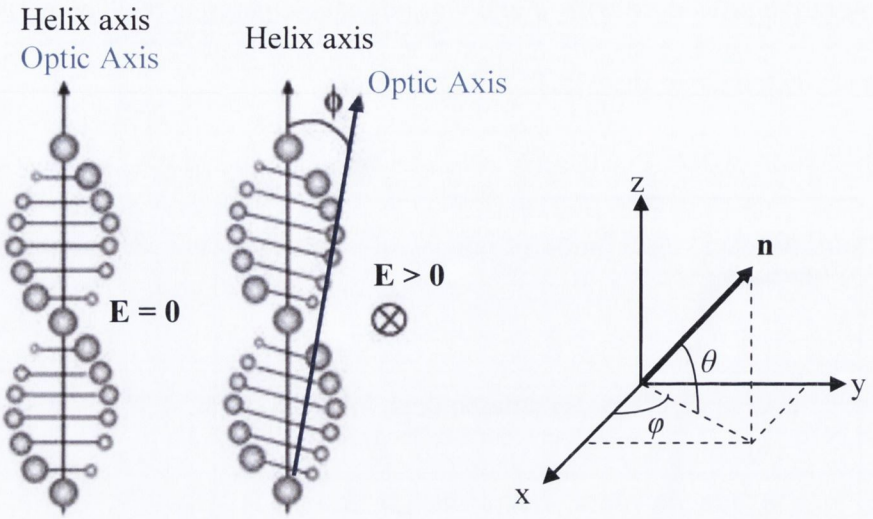

Figure 2.13: Illustration of the rotation of the optic axis with applied electric field. The helix axis is collinear with the z-axis. Image modified from [12].

Generally, when a cholesteric liquid crystal is confined between the substrates of a planar sandwich cell, the chiral nematic layer adopts a Grandjean structure, where the helix axis is perpendicular to the substrates. In order to exploit the converse flexoelectric effect in such configurations, an Ultra Lying Helix (ULH) structure has to be introduced, wherein the helix axis lies along a unique direction parallel to the substrates. The ULH texture is largely unstable as it is not compatible with both homeotropic and planar alignments, as the minimum free energy configuration of CLC is the Grandjean texture. The conventional method to obtain this texture in a material with positive $\Delta\varepsilon'$ involves cooling the sample from the isotropic phase under the application of a moderate field [13]. Additionally, in some cases the device maybe subjected to mechanical shearing in a direction perpendicular to the rubbing direction once the sample is cooled down to the CLC phase.

In the geometry considered (Fig. 2.13), a short pitched chiral nematic is confined between the cell substrates with the helix axis lying along the z direction. When an

electric field **E** = (E, 0, 0) is applied across the sample, the total bulk free-energy density of the system, which includes the elastic, flexoelectric and dielectric contribution is given by [14]:

$$F(E)_f = \frac{1}{2}\left[K_{11}(\nabla\cdot\mathbf{n})^2 + K_{22}(\mathbf{n}\cdot\nabla\times\mathbf{n}+k)^2 + K_{33}(\mathbf{n}\times\nabla\times\mathbf{n})^2\right]$$

$$-\mathbf{E}\cdot\left[e_1\mathbf{n}(\nabla\cdot\mathbf{n}) - e_3\mathbf{n}\times(\nabla\times\mathbf{n})\right] - \frac{\varepsilon_0\Delta\varepsilon'}{2}(\mathbf{E}\cdot\mathbf{n})^2. \qquad (2.37)$$

Here k is the helical wave-vector defined as $k = 2\pi/p$, $\Delta\varepsilon'$ is the dielectric anisotropy and p is the optical pitch. The minimization of the average free energy per unit volume yields [14]:

$$\tan\phi = \frac{(e_1 - e_3)}{2K_{22}k}E - \frac{(K_{11} - 2K_{22} + K_{33})}{2K_{22}}\sin\phi. \qquad (2.38)$$

For materials with small positive dielectric anisotropy, and for small applied electric fields, the tilt of the optic axis is approximated by [13]:

$$\tan\phi = \frac{e'p}{2\pi K}E, \qquad (2.39)$$

where e' and K are the flexoelectric and effective elastic constants, respectively. These are defined as: $e' = \frac{|(e_1 - e_3)|}{2}$, $K = \frac{K_{11} + K_{33}}{2}$; $|(e_1 - e_3)|$ is the effective flexoelectric coefficient, p is the optical pitch. Hence, one can evaluate the value of $|(e_1 - e_3)|$ if the pitch, and the splay and bend elastic constants are known. The effective flexoelectric coefficient $|(e_1 - e_3)|$ governs the flexoelectric properties of a system when constant electric field is applied across the liquid crystalline system [15]. This method has a number of favourable features such as [15]: (a) there are no complications due to surface polarization, (b) the contribution of ionic screening maybe ignored since an AC signal maybe used, (c) the technique does not strongly depend on the surface anchoring

strength, (d) both the sign and magnitude of the bulk flexoelectric coefficient can be determined, (e) the dielectric response does not significantly affect the observations for smaller applied fields. However, one of the major drawbacks of this technique is that requires an intrinsically chiral material, or else a chiral dopant must be added. Addition of large concentration of the chiral agent (> 10-15 %) can modify the properties of the pure nematic material, hence affecting the accuracy of the flexoelectric measurements. However, with recent developments of high twisting chiral dopants, it is now possible to create samples with pitch < 1μm, with much smaller concentration of the additives. In this thesis, two chiral agents S 811 and R5011 (weight concentrations < 4%), with high twisting power (HTP) were used to produce chiral mixtures. Such low concentrations ensure that the properties of the host material are not drastically modified because of the chiral dopant.

2.7.1 Measurement of Optical Pitch

The helical pitch of a cholesteric liquid crystal (CLC) is an important parameter which plays a crucial role in the modelling of LC structures. One of the easiest techniques to measure the helical pitch p is based on determining the wavelength of selective reflection of light. When p is in the range of the wavelength of visible light, this phenomenon is readily visible to the naked eye as an iridescent colour when the chiral LC is confined in a planar cell. For light at normal incidence to the CLC sample cell, i.e. light propagates along the helical axis, the maxima of selective reflection occurs at a wavelength λ_0 [16]. This is related to p as:

$$\lambda_0 = np, \tag{2.40}$$

where n is the effective refractive index defined as $n = (n_o + n_e)/2$; where n_o and n_e

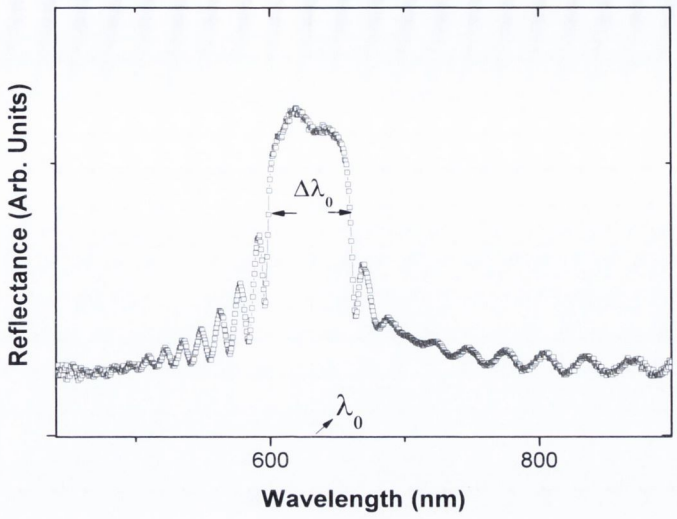

Figure 2.14: UV-Visible Reflectance spectra obtained in a 5μm planar cell filled with the CLC mixture CBC11CB + 3% R5011 (studied in Chapter 4), at a reduced temperature $T\text{-}T_{NI}$ = -4°C. The subsidiary oscillations (or side-lobes) are a result of the interference between the two surfaces of the cell, within which the CLC is confined.

are the ordinary and extraordinary refractive indices respectively. For normal incidence, the bandwidth of the transmittance/reflection spectra $\Delta\lambda_0$ is related to the birefringence Δn by the equation:

$$\Delta\lambda_0 = p\Delta n. \tag{2.41}$$

The reflectance/transmission spectrum is easily obtained by a UV-visible/IR spectrophotometer when the pitch is within the measuring range of the equipment (360 - 2200 nm). An example of the UV-Visible Reflectance spectra obtained in a 5μm planar cell filled with the CLC mixture CBC11CB + 3% R5011, (studied in Chapter 4), at a reduced temperature $T\text{-}T_{NI}$ = -4°C is shown in Fig. 2.14. When p is longer, it is necessary to use another technique. All experiments involving chiral liquid crystals in this thesis (Chapters 3 and 4) are based on short pitch CLCs ($p < 1\mu m$).

2.7.2 Determining the Tilt of the Optic Axis

In order to measure the tilt angle, the hot stage with the sample aligned in ULH structure, regulated by a temperature controller, was fixed onto the polarizing microscope set-up (refer to Fig. 2.2). An electric field was then applied to the device using a signal generator, which causes an in-plane rotation of the optic axis due to the flexoelectric coupling. The response of the device to the field as sensed by a photodiode is recorded by a digitizing oscilloscope (Tektronics TDS 2014) for various angles of the optic axis with respect to the polarizer at step of 10^{o}. An example of the signal produced for the CLC mixture (C4 + 1.5 % S 811), studied in Chapter 3, for an applied field (square wave, frequency: 20 Hz), when the optic axis lies at ~22.5° with respect to the polarizer is shown in Fig. 2.15.

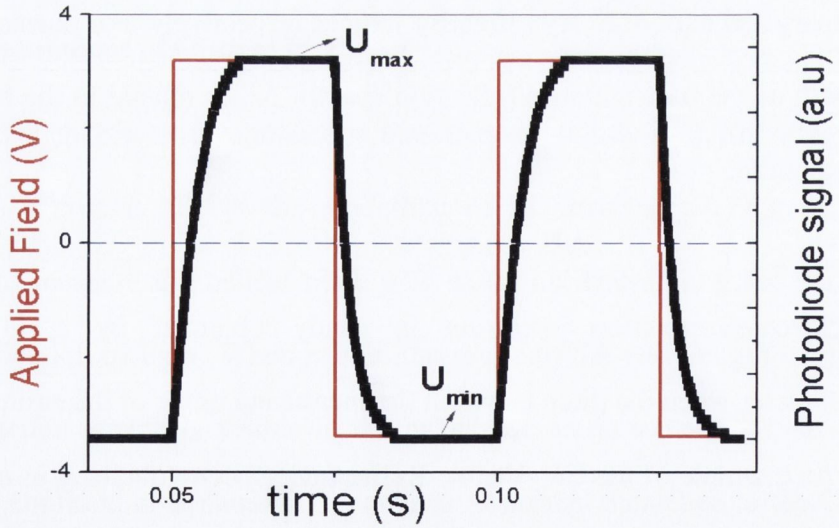

Figure 2.15: The electro-optical response of the ULH obtained for the CLC mixture - C4 + 1.5% S 811 at $T-T_{NI} = -2^{o}C$, measured using a photodiode under the application of a square-wave driving voltage; frequency: 20 Hz. The device is placed between crossed polarizers, with the optic axis oriented at ~22.5° to the polarizer.

The maximum and minimum amplitude of the signal, U_{max}(+E) and U_{min}(-E) at a particular instant in time was then plotted as a function of the rotation angle θ. This generates a periodic wave, which is fitted to a sine-wave function in order to minimize the error in the data collection. The phase difference between the two waves is equal to 2ϕ (as demonstrated in Fig. 2.16), from which the tilt angle can be easily determined. Measurements were carried out at fields much below the helix unwinding. Furthermore, higher fields could also have effect of damaging the cells.

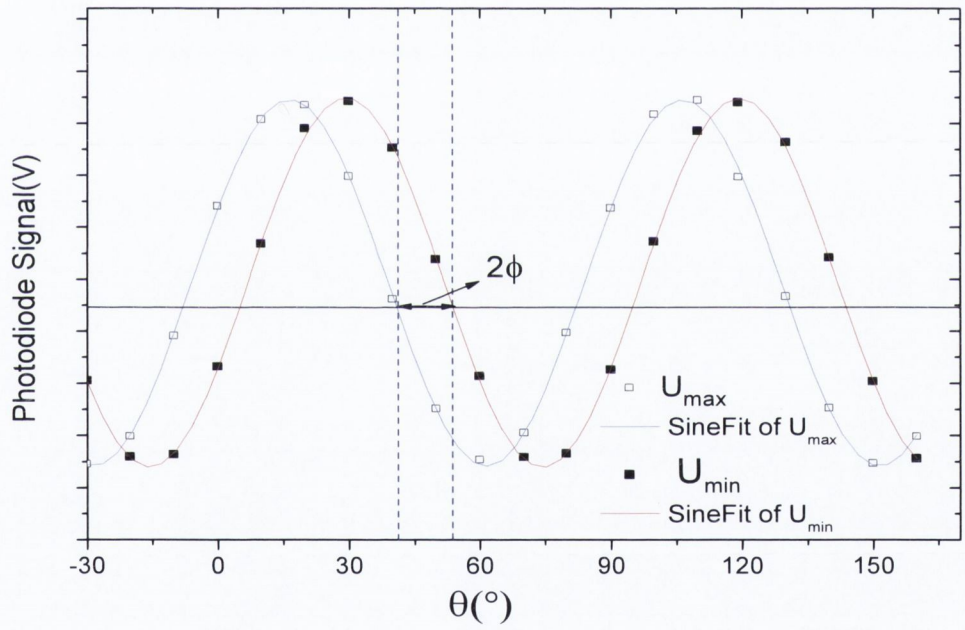

Figure 2.16: The photodiode signal at a fixed point (in our case time) as a function of sample rotation angle θ, for the CLC mixture - C4 + 1.5% S 811 at $T-T_{NI}$ = -2^{o}C, for applied field: 0.6×10^{6} V/m and frequency: 20 Hz. The open square (□) represents the maximum amplitude U_{max} of the ULH signal and the closed square (■) represents the minimum amplitude, U_{min}. The blue and red lines are the best fits of curves for U_{max} and U_{min}, respectively. The difference between the two signals, as marked in the figure, corresponds to 2ϕ.

References

[1] V. Panov, J.K. Vij and N.M. Shytkov, *Liq. Cryst.* **28**, 615 (2001).

[2] B.C. Smith, Fundamental of Fourier Transform Infrared Spectroscopy. (CRC Press, Florida, 1996).

[3] V. M. Vaksman, and Yu. P. Panarin. *Mol. Mats.*, **1**, 147 (1992).

[4] Oriano Francescangeli, Vesna Stanic, Sofia I. Torgova, Alfredo Strigazzi, Nicola Scaramuzza, Claudio Ferrero, Igor P. Dolbnya, Thomas M. Weiss, Roberto Berardi, Luca Muccioli, Silvia Orlandi and Claudio Zannoni, *Adv. Func. Mater.*, **19**, 2592 (2009).

[5] V. Freedericksz and V. Zolina, *Trans. American Electrochem. Soc.*, 55, **85** (1929).

[6] H. J. Deuling, *Mol. Cryst. Liq. Cryst.*, **19**, 273 (1992).

[7] A. Rapini and M. Papoular, *J. de Physique Colloq.*, **30**, 54 (1969).

[8] D. Dunmur and K. Toriyama, in *Handbook of Liquid crystals*, ed. D. Demus, J. Goodby, G.W. Gray, H.W. Speiss and V.Vill, Wiley-VCH: Weinheim Vol. 1, 1988.

[9] G. Vertogen, W.H. de jeu, *Thermotropic Liquid crystals, Fundamentals*, page 94 (1988).

[10] H. Made, S. Kobayashi, *Mol. Cryst. Liq. Cryst.*, **33**, 47 (1976).

[11] J. S. Patel and R. B. Meyer, *Phys. Rev. Lett.*, **58**, 1538 (1987).

[12] F. Castles, S. M. Morris and H. J. Coles, *Phys. Rev. E*, **80**, 031709 (2009).

[13] S.-D. Lee and J. S. Patel, *Phys. Rev. A*, **42**, 997 (1990).

[14] H. Coles, in *Handbook of Liquid crystals*, ed. D. Demus, J. Goodby, G.W. Gray, H-W. Speiss, V.Vill, Wiley-VCH: Weinheim, Vol. 2A, 1998.

[15] F. Castles, S. C. Green, D. J. Gardiner, S. M. Morris and H. J. Coles, *AIP Advances*, **2**, 022137 (2012).

[16] M. Mitov, *Adv. Mater.*, **24**, 6260–6276 (2012).

Chapter 3

Elastic and Flexoelectric Properties of Bent-Core Liquid Crystals

In this chapter, the effect of cybotactic clusters on the elastic and flexoelectric properties are studied in three bent-core LCs belonging to a homologous series. The compound with the shortest terminal chain does not show appreciable presence of clusters; however they are present in the nematic phase of the other materials.

Contents

3.1 Introduction

Bent-core compounds exhibiting nematic phase have aroused a lot of interest due to a range of interesting properties which include induced biaxiality [1], giant flexoelectric effect [2], and sign reversal of the dielectric anisotropy [3-4] etc., which offer opportunities for new technical applications. The structural origin of these properties is not definitely established but various experimental results [2-5] suggest that short range molecular correlations may play an important role in bent-core molecules exhibiting extra-ordinary material properties in comparison to the conventional rod-like mesogens. Though smectic phases of bent-core and calamitic systems offer huge potential for a range of applications, most commercially successful LC based applications, so far, are mostly based on nematics. This is owing to a number of desirable properties of nematics such as their lower viscosity, greater response to external electric, magnetic fields, mechanical distortions, as well as to their fast recovery from defects [6].

The viscoelastic properties of a material significantly influence the performance of nematic liquid crystalline based applications, and its knowledge is therefore important in designing/optimizing LC devices [7]. There is considerable interest in studying the behaviour of the elastic constants as they offer insight into understanding director distortion in samples, fluctuations in order parameter etc. Furthermore, the elastic constants influence the threshold voltage for switching, while the elastic constant ratio governs the steepness of the electrodistortional curves [7]. For conventional calamitics the ratio of K_{33}/K_{11} varies from 2 to 3 and K_{33} is usually greater than K_{11}. However, in some bent-cores this ratio has been determined to be <1 and decreases as the chain length is increased. The decrease in the ratio of K_{33}/K_{11} is attributed to the

presence of smectic like clusters/ underlying smectic phases [8], and in some cases related to the position of the substituent molecules or the position of the double bonds etc [9]. Dodge et al. [10, 11] showed that by mixing a small amount of bent-core systems in a calamitic nematic, K_{33} is significantly reduced. Kundu et al. [12] made similar findings for calamitic 8OCB mixed with different concentrations of bent-core liquid crystal in the nematic phase, but additionally they obtained anomalous temperature dependence of K_{11} and K_{33} close to the nematic-smectic phase transition. During the last few years, measurement of these constants in pure BCN's in nematic phase has also yielded intriguing results, where K_{33} is found in most cases to be lower than K_{11} [13,14]. The temperature dependence of the elastic constants in pure BCNs has been interpreted in terms of: (a) coupling of the bent molecular shape with the bent distortions of the molecules [13] resulting in lower value of K_{33} compared to K_{11}; or (b) presence of nanoscale smectic-like clusters which causes the softening of K_{33} relative to K_{11} [14].

Similar to the elastic constants, the flexoelectric effect is expected to be considerably different, and presumably larger [2], in BCN's than in conventional calamitics. Harden et al. [2] determined the bend flexoelectric coefficient $|e_3|$ for a banana system in its nematic phase, via the current produced by mechanical flexing of the NLCs bounding surfaces, and found $|e_3|$ to be higher by a factor of 10^3 than for calamitic liquid crystals. However the validity of this finding has been debated recently [15, 16] as these results so far cannot be reproduced using other methods [15]. Irrespective of the correctness of this result, the finding in itself has led to intensive investigations. If the results were eventually found to be correct, we would be able to design much more effective devices for converting mechanical energy into electrical energy by employing bent-core liquid crystals in flexoelectric devices.

In this chapter we present the experimental results of the splay (K_{11}) and bend (K_{33}) elastic constants, and the effective flexoelectric coefficients $|(e_1 - e_3)|$ for three BCNs (C4, C6 and C7) belonging to a homologous series. Comparisons are made in the data obtained for materials that show significant presence of Smectic-*C* like clusters in their nematic phase (C6 and C7) to that of a compound (C4) in which these are measurably absent. We investigate whether the clusters have any major influence on the flexo-elastic properties of these materials.

This chapter is divided into two sections: the first part presents the results of dielectric and elastic constant studies in the nematic phase of the materials; the second part discusses the results obtained for the flexoelectric measurements.

3.2 Materials under investigation

The materials studied in this chapter, C4, C6 and C7, are 4-cyanosubstituted resorcinol derivatives that belong to a homologous series. The materials have the same 4-cyanoresorcinol bisbenzoate core but differ in chain-lengths, n = 4 (C4), n = 6 (C6) and n = 7 (C7). The bent-core part of the compound is composed of five phenyl rings, and each ring is connected by an ester link. Both ends of the core part are attached to a terminal group. A cyano group is substituted on the central aromatic ring, which plays an important role in the formation of the nematic phase.

The phase behaviour and transition enthalpy for the compounds were investigated by the Halle group [17]. The generic structure of the series is shown in Fig. 3.1 and the phase transition temperatures are summarized in Table 3.1. The terminology of the phases used in this chapter is also taken from [17]. When cooled from the isotropic phase to lower temperatures the materials exhibit I-N transition; C4

and C7 show a monotropic nematic phase while C6 exhibits an enantiotropic phase. We also found that C4 had a tendency to crystallize at lower temperatures in the nematic phase (this is discussed further in section 3.3.1).

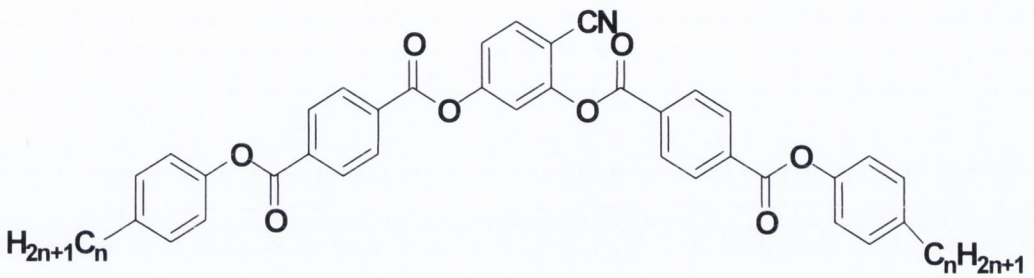

Figure 3.1: Generic structure of the bent-core compound 4-cyanoresorcinol bis benzoates under investigation

n	Phase Transitions		
4	Cr 117 [38.4]	(*N* 107 [0.5])	Iso
6	Cr 98 [37.1]	N_{cybC} 101 [0.5]	Iso
7	Cr 96 [35.5] (Sm*C* 25 [0.3] Cyb*C* 41 [0.2])	N_{cybC} 111 [0.7]	Iso

Table 3.1 : Transition temperature (T / ^{o}C) and the associated enthalpy values (in square brackets, Δ /kJ mol^{-1}) of the materials under study [17].

Peak temperatures obtained in the first DSC heating curves (10 K min^{-1}). Abbreviations: Cr = crystalline solid; Iso = isotropic liquid; *N* = nematic phase with nearest neighbour correlation, similar to ordinary nematic phases; N_{cybC} = nematic phase composed of Sm*C* type cybotactic clusters; The values enclosed in the round brackets refer to the monotropic transitions as observed on cooling [17].

3.3 X-ray Diffraction Studies

XRD studies were carried out in the nematic phase of these compounds, oriented using a magnetic field of medium strength ($B \approx 1$ T, cooling rate 0.1 K min^{-1}) [17]. The diffraction pattern obtained for compounds C4, C6 and C7 is shown in Fig. 3.2 as an example.

The intensity of the small angle scattering (I_s) was observed to increase with increasing chain length. For the material with the shortest chain length, C4, the small angle scattering was similar to that observed for ordinary nematic phases. In the nematic phase, I_s was noted to have lower or almost equal intensity compared to the wide angle scattering (i.e., $I_s \leq I_w$). In C6, on the other hand, I_s was much stronger than the wide angle scattering, which according to de Vries [18] indicates a "cybotactic" nematic phase ($I_s \gg I_w$). Furthermore, with increasing chain length, a continuous decrease of the small angle splitting together with an increase of the scattering intensity was observed. This indicates a continuous growth of the cluster size with chain length. Significant temperature dependence was also noted; at high temperatures the nematic phases have relatively small clusters, and the cluster size grows strongly as the temperature is decreased [17].

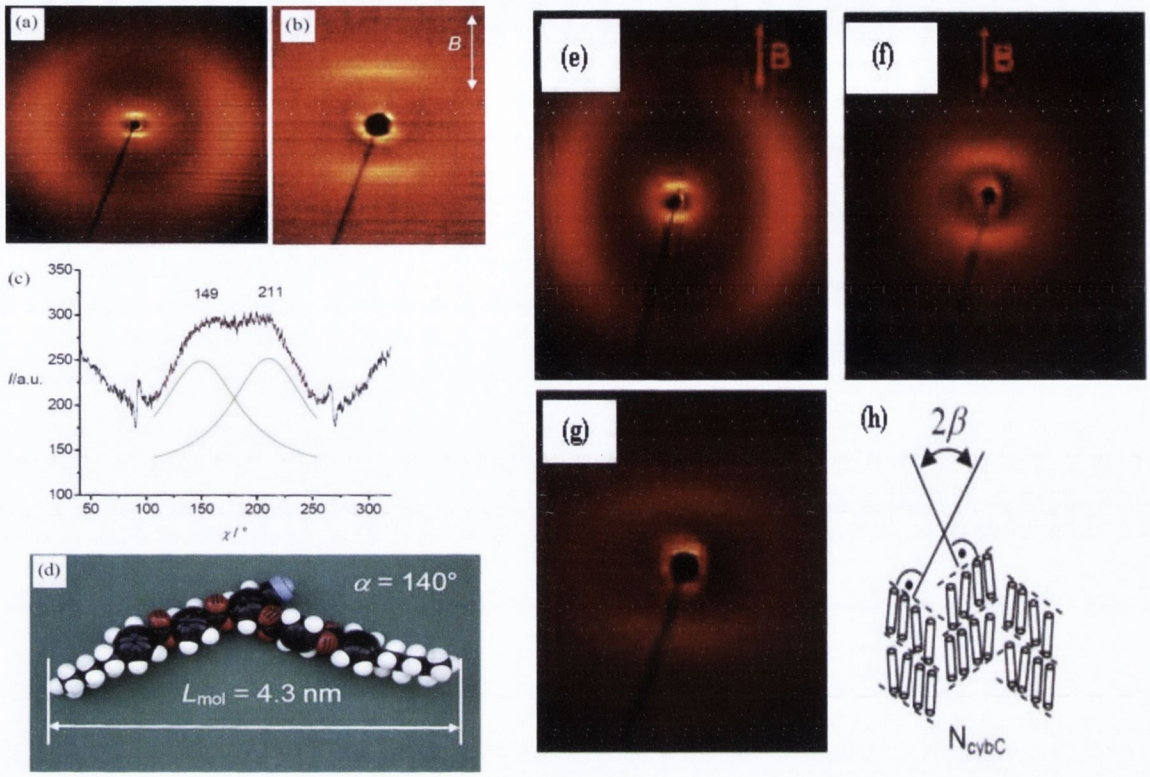

Figure 3.2: Investigation of the XRD patterns. **C6**: (a and b) X-ray diffraction pattern (wide angle and small angle) of a magnetically aligned sample at T = 80 °C; arrow indicates the direction of the magnetic field; (c) χ-scan over the diffuse small angle scattering, indicating the presence of Sm*C* type cybotactic clusters (d) CPK model showing the material in a V-shaped conformation with a bending angle α = 140° and stretched alkyl chains. **C7**: (e) the diffraction pattern at 100°C (f) magnified part of the small angle. **C4**: (g) small angle diffraction patterns of magnetically aligned samples in the nematic phase at 90°C. (h) Organization of the molecules in a skewed cybotactic nematic phase (N_{cybC} phase) aligned under a magnetic field *B* parallel to the molecular long axis. The images for C4 and C6 are reprinted from ref. [17], while that for C7 are taken from the supplementary information of ref [17].

Part I

3.4 Dielectric and Elastic Constant Measurements

3.4.1 Experimental Method

Sandwich liquid crystal cells were prepared by using indium tin oxide (ITO) glass plates. The typical thickness used in the experiments ranged from 5-10 μm.

The parallel and perpendicular components of the dielectric constants, $\varepsilon'_{\parallel}$ and $\varepsilon'_{\perp}$ were obtained from homeotropic and planar cell respectively by using Novocontrol Broadband High Resolution dielectric spectrometer, Alpha-A Frequency Analyzer interfaced with a PC.

The optical retardation, δ was measured with the help of the PEM setup. The retardation data was obtained as a function of temperature and voltage by applying a sinusoidal voltage of ~20 V_{pk} at a frequency of 1 kHz. The splay elastic constant, K_{11} was determined from the threshold voltage (V_{th}) for *Freedericksz* transition by using equation (2.29). The bend elastic constant, K_{33} was obtained from the theoretical fit of the retardation data above the threshold voltage to the parametric equations (2.28) and (2.36) by an iterative procedure.

3.4 Results and Discussion

3.4.2 Cross-over Temperature (C_T) Measured using Dielectric Permittivity

The dielectric data obtained for C4, C6 and C7 at a frequency of 1 kHz as a function of the reduced temperature $T-T_{NI}$ is plotted in Fig. 3.3; where T_{NI} is the nematic-isotropic transition temperature. For all three materials the value of $\Delta\varepsilon'$ is positive at higher temperatures, but as the temperature is reduced further it tends to

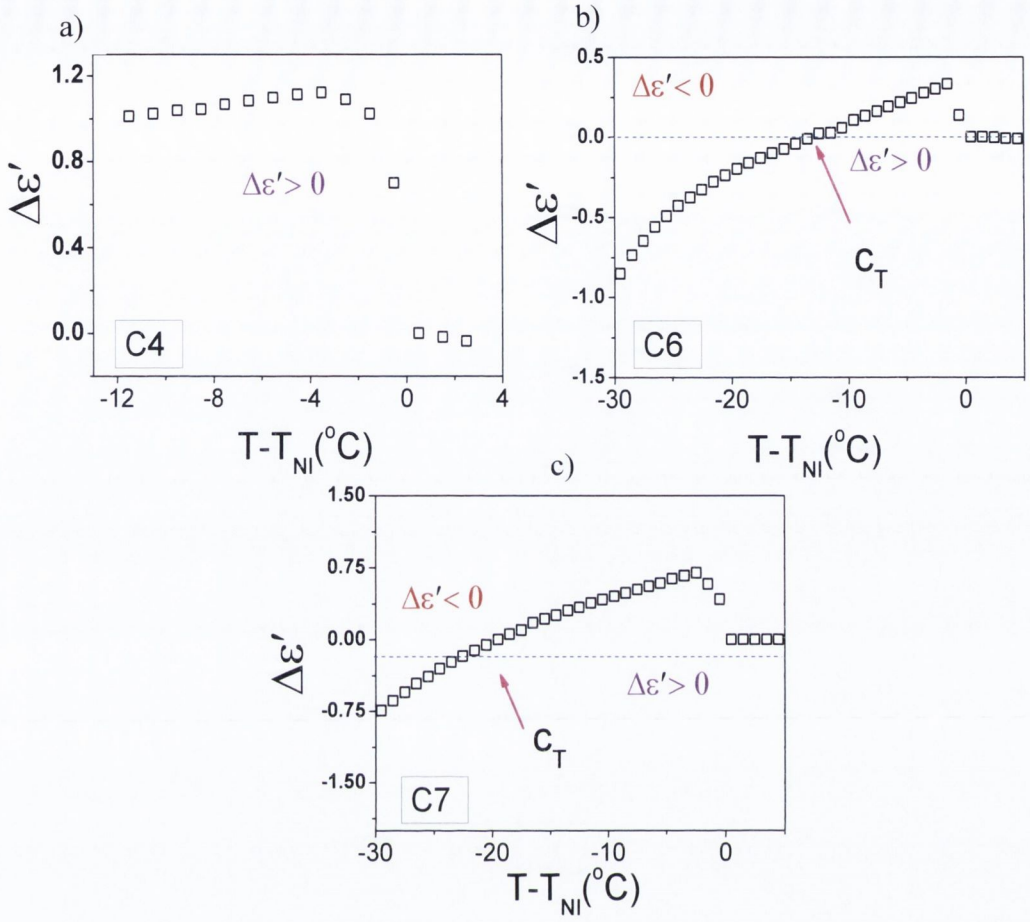

Figure 3.3: Dielectric Anisotropy of C4 (a), C6 (b) and C7 (c) as a function of reduced temperature T-T_{NI} (°C), where T_{NI} is the I-N transition temperature; Frequency: 1 kHz. C_T is the cross-over temperature.

become negative below a certain crossover temperature, C_T. The crossover temperature is easily determined for C6 and C7 from the dielectric data, and the nematic phase is found to extend over a wide range of temperatures. However C4 when kept at lower temperatures (but higher than the nematic-crystalline transition temperature) tends to crystallise with passage of time. Figure 3.4 shows how the perpendicular component of permittivity for C4, determined from a planar cell, decreases at lower temperatures due

to the slow crystallization of the material much before the onset of the crystalline phase. Hence the optical measurements for C4, carried out in planar cells, could only be made at temperatures where it does not crystallize with time. The value of $\Delta\varepsilon'$ is ≤ 1.1 for C4, ≤ 0.3 for C6 and ≤ 0.7 for C7.

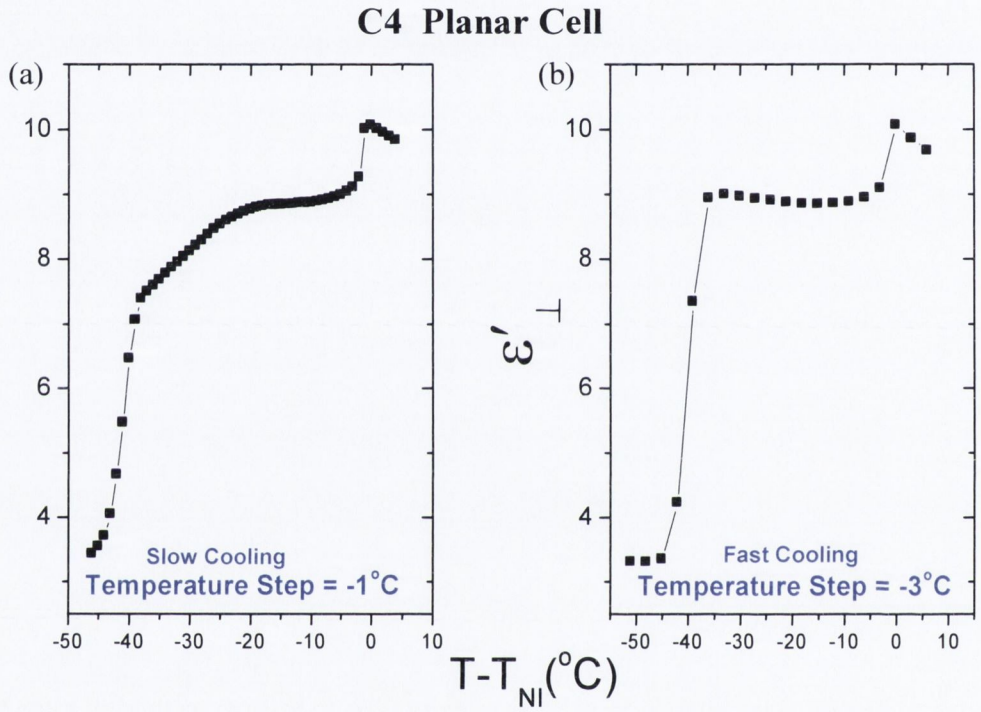

Figure 3.4: Dielectric permittivity of C4 shows a drop in the value of the perpendicular component of ε' at a frequency of 1 kHz due to crystallization of the material at lower temperatures. Data in (a) are recorded with a temperature step of -1°C, and in (b) with a temperature step of -3°C (faster cooling). Each temperature point takes 6 to 8 min to scan.

Detailed dielectric studies by Jang et al. [4] in this series of cyanoresorcinols revealed that the sign reversal of $\Delta\varepsilon'$ in the material with no measurable clusters (C4) was related to the relaxation of the longitudinal component of the dipole moment

occurring at much lower frequencies compared to the transverse component. They ruled out the possibility of conformational change (used to describe the sign reversal phenomena in calamitic molecules) as affecting the value of $\Delta\varepsilon'$ [4]; this is also confirmed by the flexo-elastic results obtained by us in section 3.5.3.

In the materials with longer chain length the temperature dependence of permittivity was found to be related to a change in the strong anisotropic correlations among the molecules taking place with temperature. Results of the dielectric study [4] also showed that C7 exhibits strong short-range polar correlations normal to the director. The correlation lengths of these interactions were found to be similar to those obtained from the X-ray scattering [17].

3.4.3 Cross-over Temperature (C_T) Measured using *Freedericksz* Transition

A change in the sign of the dielectric anisotropy observed using dielectric spectroscopy is also confirmed by the optical contrast spectroscopy technique [3]. This method is known for its higher reliability, especially when ions are present in a liquid crystalline medium. In this technique, the planar cell, kept under crossed-polarizers, is cooled down from the isotropic to nematic phase with a constant field (9.5V, 1 kHz sine wave) applied across it. The change in the transmission is recorded as a function of temperature [3]. The setup for this experiment consists of a Leitz polarizing microscope, photodiode (Hamamatsu C6386), and a data acquisition board (NI-USB-6216) interfaced with a computer, as represented in Fig 3.5. The scanning time for each data point is ~ 2 sec.

When an electric field much greater than the threshold voltage (V_{th}) is applied to the cell in a temperature region where $\Delta\varepsilon' > 0$, *Freedericksz* transition occurs, leading to

a drastic change in the intensity observed through the crossed polarizers. In the temperature ranges where $\Delta\varepsilon' < 0$, no *Freedericksz* transition is observed and the alignment remains planar.

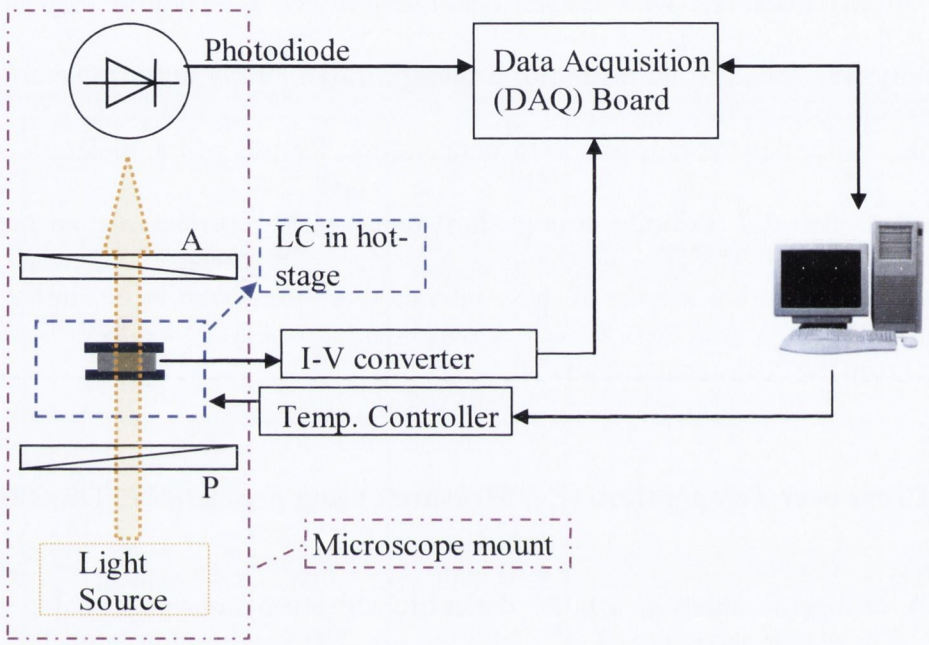

Figure 3.5: Schematic representation of the optical contrast spectroscopy set-up; here, 'A' and 'P' refer to analyzer and polarizer, respectively.

Figure 3.6 shows the transmittance as a function of the reduced temperature for C4, C6 and C7. The dashed line indicates a sharp transmittance change closer to the temperature where the dielectric anisotropy changes its sign. Although this technique may not give the exact crossover temperature and the value of $\Delta\varepsilon'$, it is effective in determining its sign reversal.

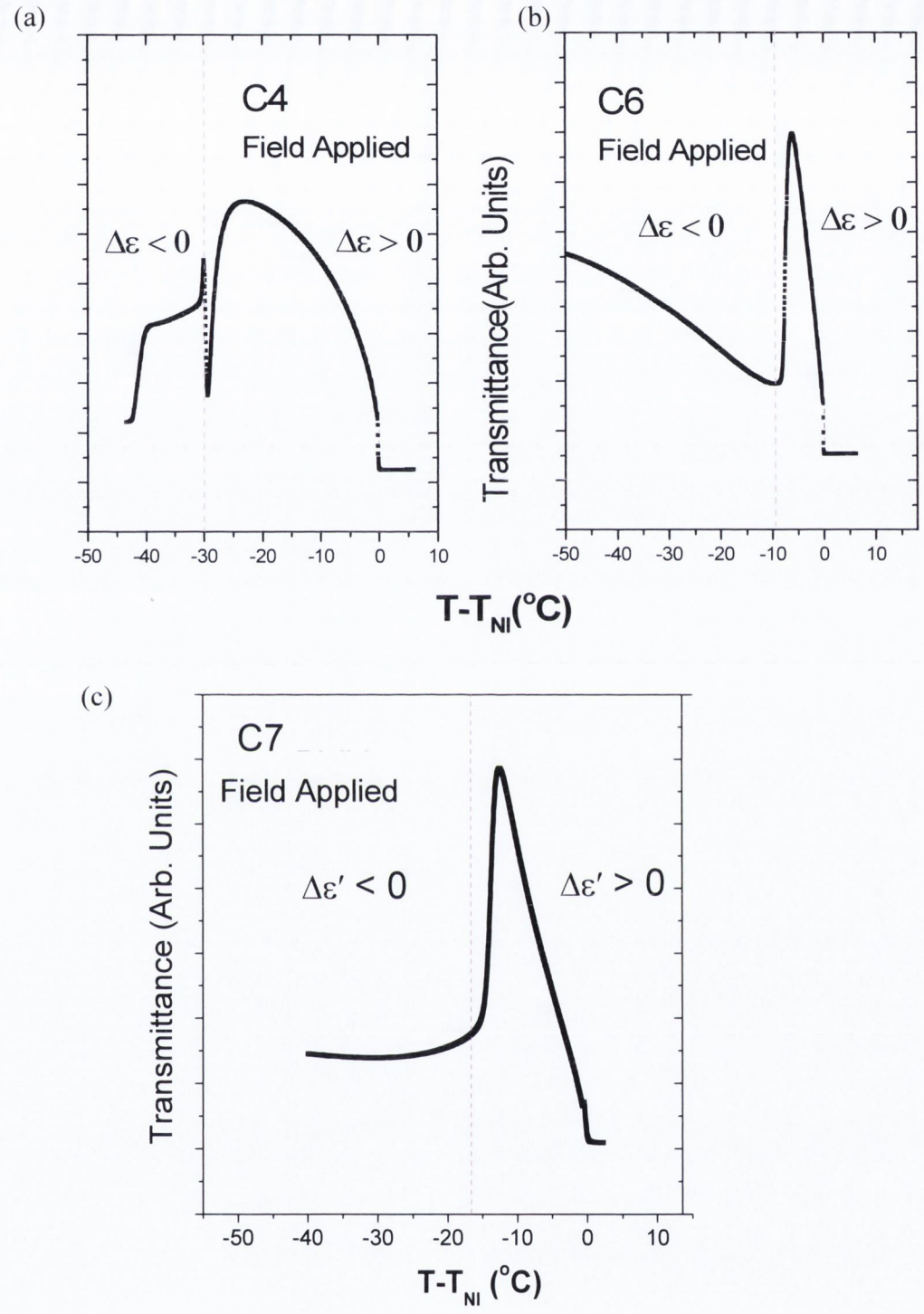

Figure 3.6: The variation of transmittance through a planar cell as a function of the reduced temperature for (a) C4, (b) C6 and (c) C7, with applied field of 9.5 V and 1 kHz sinusoidal signal. Waiting time between each data point was kept ~2 s.

Due to a very small positive value of $\Delta\varepsilon'$ of C6 (Figure 3.3) over a narrow range of temperatures (Fig. 3.6(b)) below the I-N transition, we have restricted our flexo-elastic studies to these temperatures only. The supercooling effect observed in C4 (Fig. 3.4) also restricts our studies at the higher temperature range for this material as well.

3.4.4 Elastic Constants

The splay and bend elastic constants were determined in the ordinary nematic phase from the voltage dependent retardation data using the method described in Section 2.6. An example of the theoretical fit to the retardation curve for a reduced temperature, $T\text{-}T_{NI} = -6^{\circ}C$ for C6 is shown in Fig. 3.7.

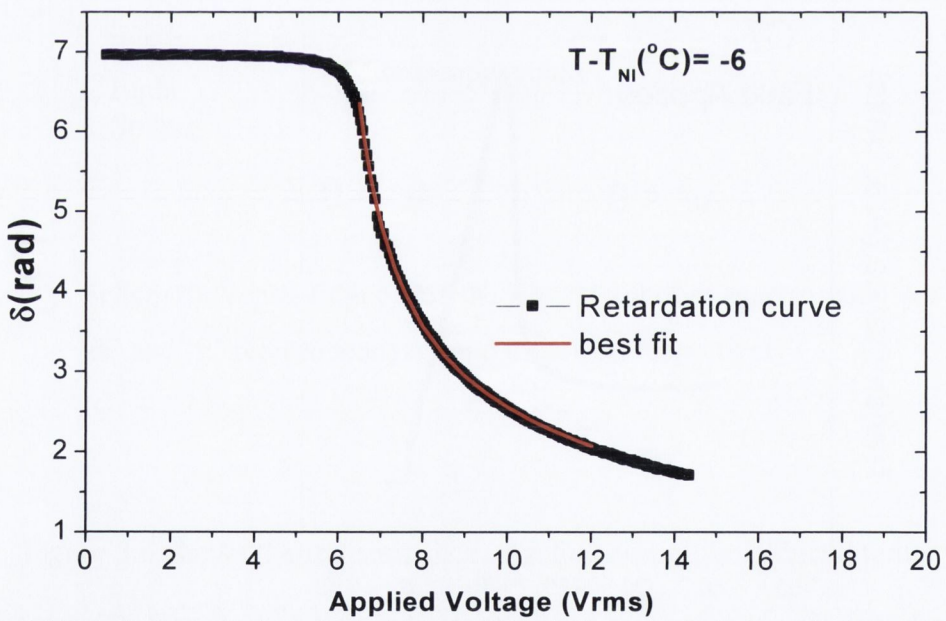

Figure 3.7: Retardation as a function of applied voltage for C6 for $T\text{-}T_{NI} = -6^{\circ}C$; the continuous red-line is the theoretical fit to eqn. (2.28) and (2.36), used to determine K_{33}.

The temperature variation of the splay and bend elastic constants hence obtained is plotted in Figure 3.8. The symbols with the bar denote the possible errors in the calculation due to the absence of a sharp threshold voltage V_{th}, and errors involved in the normalization of temperature; different set-ups are used to obtain the parameters for evaluating K_{11} and K_{33} using the iterative procedure.

For all the materials studied, K_{11} increases with a reduction in temperature; the increase is almost linear for C6, where the value increases from ~3.97 pN at 2 °C below the I-N transition to 8.81 pN at the lowest measured temperature. The changes are much subtle for C4 and C7 where it increases from 3.44 to 5.05 pN and ~ 3.89 to 9.98 pN respectively as the temperature is lowered. The maximum splay elastic constant K_{11} for C6 is found to be almost 2.2 times its lowest value, while for C4 the increase in K_{11} is ~1.5 times and is almost ~ 2.56 for C7 for the lowest temperature measured. On the other hand, K_{33} is lower than K_{11} for all the compounds studied, irrespective of the chain length or presence/absence of clusters. The bend elastic constant is found to be nearly independent of temperature for C6, whereas for C4 and C7 it increases marginally when the temperature is reduced. In general, the temperature dependence of K_{11} and K_{33} agree with other BCN systems [12, 13, 19].

The ratio of K_{33}/K_{11} in the case of C6 is seen to decrease from ~0.8 at $T-T_{NI} = -2$ °C to 0.45 at $T - T_{NI} = -7$ °C; for C4 the ratio only varies slightly from ~0.85 to 0.78 as the temperature is lowered, while for C7 the ratio is seen to be almost temperature invariant, and ranges between ~0.48 to 0.39 in the temperature range measured. The trend nevertheless is different than those observed for calamitic nematics [20].

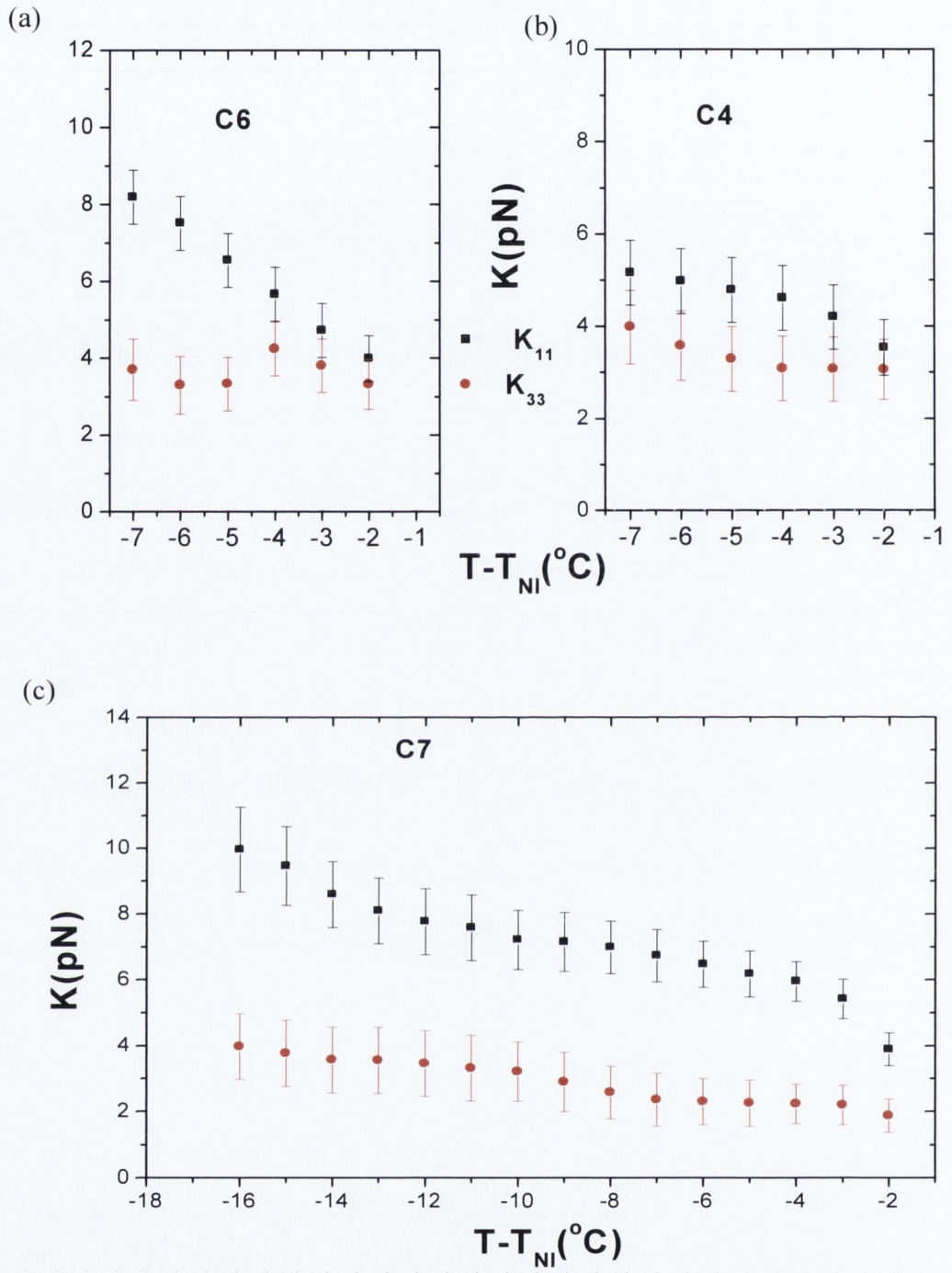

Figure 3.8: The splay and bend elastic constants of (a) C6, (b) C4 and (c) C7 measured as a function of the reduced temperature. The symbols with the bar denote the possible errors present in the calculation due to the absence of a sharp threshold voltage V_{th}, and errors involved in the normalization of temperature; different set-ups are used for calculating different parameters in calculating K_{11} and K_{33} using the iterative procedure.

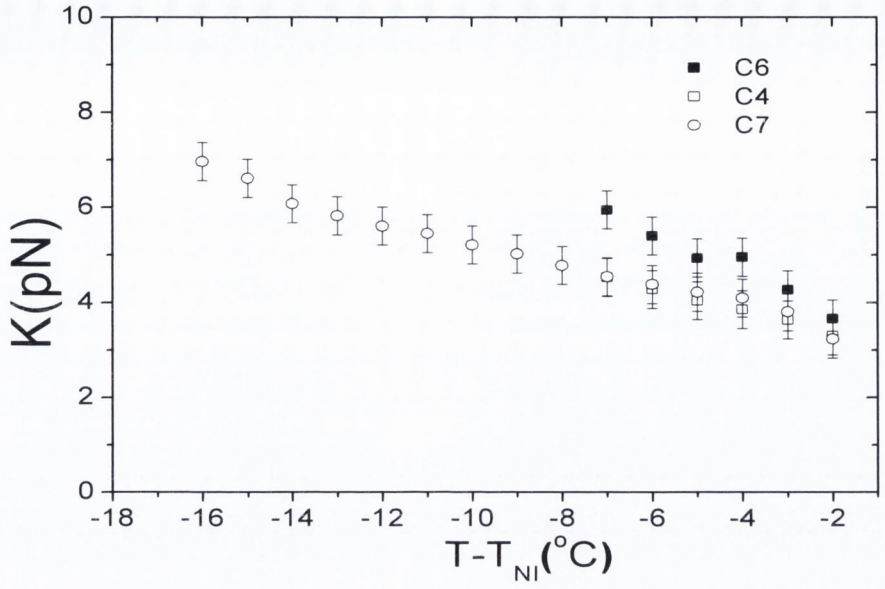

Figure 3.9: Plot of the effective elastic constant K as a function of the reduced temperature. Closed squares (■) represent the data for C6, open squares (□) for C4 and open circles (○) for C7.

The effective elastic constant K is plotted as a function of reduced temperature in Fig. 3.9. The effective elastic constant is an important parameter in the determination of the flexoelectric coefficients as seen from eqn. (2.39), which one can re-arrange to obtain $\tan\phi \propto \frac{e}{K}$, hence, theoretically, a lower K implies a larger value of the flexo-optic tilt angle, ϕ . For all the materials, K is seen to increase with decreasing temperature. The value of K is greater for C6 in comparison to C4 and C7.

The results obtained here in the three bent-core systems show that even in the absence of the cybotactic clusters in C4, K_{33} is lower than K_{11}. We can thus state that $K_{33} < K_{11}$ in BCN's is due to the bent shape of the molecules rather than being due to the presence of clusters.

For an oxadiazole bent core compound, Kaur et al. [21] found $K_{33} < K_{11}$. They explained their observations by the molecular field theory and atomistic modelling

suggesting that K_{11} is almost independent of the molecular conformation whereas K_{33} is sensitive to changes in the molecular curvature - similar to those calculated for odd-dimeric mesogens [21]. The results obtained here likewise can be explained by the theory and modelling proposed by Kaur et al. [21] and Cestari et al. [22]. The bent shape favours the bend distortions of the director as opposed to splay. The increase in K_{11} for C6 compared to C4 seems to arise from the longer molecular length rather than arising from the presence of clusters in C6.

Part II

3.5 Flexoelectric Measurements

3.5.1 Theoretical Background

For molecules with permanent dipole moments and asymmetric shapes, such as pear/drop or crescent/banana, the flexoelectric effect (Fig. 3.10) is caused by mechanical distortions or conversely by the application of electric field, as discussed in Chapter 1. The flexoelectric polarization [23] can be expressed in terms of the splay and bend flexoelectric coefficients as (re-written here for convenience):

$$P_f = e_1\mathbf{n}(\nabla\cdot\mathbf{n}) - e_3\mathbf{n}\times(\nabla\times\mathbf{n}). \qquad (3.1)$$

The flexoelectric coefficients e_1 and e_3 are connected to the splay (K_{11}) and bend (K_{33}) elastic constants, respectively. As an example, for the case when molecules fluctuate independently of each other, $e_1^2 = \varepsilon_{\parallel}' K_{11}^D$; and $e_3^2 = \varepsilon_{\perp}' K_{33}^D$ [24]; $\varepsilon_{\parallel}'$ and $\varepsilon_{\perp}'$ are the permittivities parallel and normal to ± **n**. The superscript D denotes constant electric displacement.

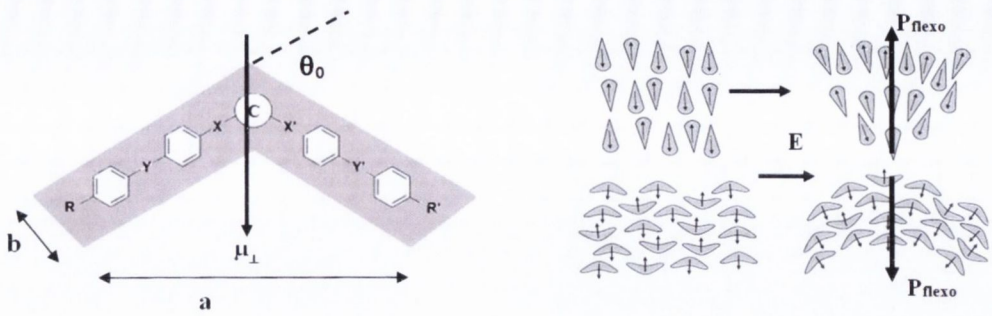

(i) (ii)

Figure 3.10: (i) A model of a bent-core molecule depicting the kink angle and the transverse dipole moment, (a) and (b) are the length and width of the molecule, (ii) illustrates how flexoelectric polarization can be induced in drop-shaped (top-right) and crescent/bend shaped (bottom-right) molecules by splay and bend distortions of the liquid crystalline medium, respectively.

Using the molecular statistical approach, Helfrich [24] also derived an expression for the bend flexoelectric coefficient:

$$e_3 = \mu_\perp \frac{K_{33}}{2k_bT}\theta_o\left(\frac{b}{a}\right)^{\frac{2}{3}} N^{\frac{1}{3}}. \qquad (3.2)$$

Here $\mu_\perp$ is the molecular dipole moment perpendicular to the molecular long axis and is directed along the bow direction, a and b denote the length and the width of a molecule, respectively. T is the absolute temperature, θ_0 is the kink angle and N is the number density. This expression shows that, in principle at least, we can design molecules that exhibit much greater bend flexoelectric coefficients in nematic phase. For bent core systems, θ_0 is ~60^0 and the molecule is designed to have a reasonably large $\mu_\perp$; such LC systems in principle can exhibit much higher bend flexoelectric coefficients provided K_{33} is also not reduced. It is conceivable however that due to the bent structure of the

bent-core or banana molecules, the elastic constants and the flexoelectric coefficients acquire different values compared to calamitics. Equation (3.2) is also applicable to calamitics where the bent-angle θ_0 is of the order of 5^{o}.

Eqn. (3.1) describes the direct flexoelectric effect in NLC's however, studies that deal with the direct effect in nematics is scarce [25-27]. Moreover, a method of finding the direct flexoelectric effect is neither easy to design nor are the experimental results easily interpretable since mechanical distortions can also cause ions to migrate through the medium. The mobility of ions could alter the measuring current as measurement frequencies are often too low, and mobility of ions caused by mechanical deformations will contribute to the measured current. It will hence be difficult to separate out the two currents; one caused by mobility of ions and the second by flexoelectric polarization. Instead most experiments revolve around the converse flexoelectric effect [25] where measurement frequencies can be higher and secondly, ions do not significantly influence the electro-optical effects as much as they affect the current measurements. The converse effect is related to the bulk flexoelectric torque, τ, arising from the director deformation caused by the electric field, and is concerned with measurement of this torque. The bulk flexoelectric torque acting on the director can be expressed as $\tau = (\mathbf{n} \times \mathbf{h})$, where $\mathbf{h}$ is the bulk flexoelectric component of the molecular field [25-27] and is defined as:

$$\mathbf{h} = e_1[\mathbf{E}(\nabla \cdot \mathbf{n}) - \nabla(\mathbf{E} \cdot \mathbf{n})] + e_3[\mathbf{E} \times \nabla \times \mathbf{n} - \nabla \times (\mathbf{E} \times \mathbf{n})]. \qquad (3.3)$$

Eqn. (3.3) can be re-written by substituting the well-established standard vector identities for $\nabla(\mathbf{E} \cdot \mathbf{n})$ and $\nabla \times (\mathbf{E} \times \mathbf{n})$, as:

$$\mathbf{h} = e_1[\mathbf{E}(\nabla\cdot\mathbf{n}) - \mathbf{E}\times\nabla\times\mathbf{n} - \mathbf{n}\times\nabla\times\mathbf{E} - (\mathbf{E}\cdot\nabla)\mathbf{n} - (\mathbf{n}\cdot\nabla)\mathbf{E}]$$
$$+ e_3[\mathbf{E}\times\nabla\times\mathbf{n} - \mathbf{E}(\nabla\cdot\mathbf{n}) + \mathbf{n}(\nabla\cdot\mathbf{E}) - (\mathbf{n}\cdot\nabla)\mathbf{E} + (\mathbf{E}\cdot\nabla)\mathbf{n}]. \qquad (3.4)$$

Now we know that $\nabla\times\mathbf{E} = 0$ (since $\mathbf{E} = -\nabla V$, where V is the scalar potential and using the vector identity $\nabla\times\nabla V = 0$). We can also ignore the terms in $\mathbf{h}$ which are parallel to $\mathbf{n}$, because when the torque is determined from $\tau = (\mathbf{n}\times\mathbf{h})$, any terms parallel to $\mathbf{n}$ in the molecular field will not lead to the torque, as the cross product of the parallel vectors is zero. Hence, these two simplifications can be made to eqn. (3.4). This leads to:

$$\mathbf{h} = e_1[\mathbf{E}(\nabla\cdot\mathbf{n}) - \mathbf{E}\times\nabla\times\mathbf{n} - (\mathbf{E}\cdot\nabla)\mathbf{n} - (\mathbf{n}\cdot\nabla)\mathbf{E}]$$
$$+ e_3[\mathbf{E}\times\nabla\times\mathbf{n} - \mathbf{E}(\nabla\cdot\mathbf{n}) - (\mathbf{n}\cdot\nabla)\mathbf{E} + (\mathbf{E}\cdot\nabla)\mathbf{n}]. \qquad (3.5)$$

Eqn. 3.5 can be re-grouped in terms of the sum and difference of e_1 and e_3 by re-arranging the terms, yielding:

$$\mathbf{h} = (e_1 - e_3)[\mathbf{E}(\nabla\cdot\mathbf{n}) - \mathbf{E}\times\nabla\times\mathbf{n} - (\mathbf{E}\cdot\nabla)\mathbf{n}] - (e_1 + e_3)[(\mathbf{n}\cdot\nabla)\mathbf{E}]. \qquad (3.6)$$

The second and third parts of the (e_1 - e_3) term can be further simplified, by writing them out in the Cartesian co-ordinates. Writing $\mathbf{n}$ in terms of the x, y and z components n_x, n_y and n_z (and similarly for the electric field), we have:

$$\nabla\times\mathbf{n} = \begin{pmatrix} \dfrac{\partial n_z}{\partial y} - \dfrac{\partial n_y}{\partial z} \\ \dfrac{\partial n_x}{\partial z} - \dfrac{\partial n_z}{\partial x} \\ \dfrac{\partial n_y}{\partial x} - \dfrac{\partial n_x}{\partial y} \end{pmatrix}, \qquad (3.7)$$

Hence,

$$\mathbf{E}\times\nabla\times\mathbf{n}=\mathbf{E}\times\begin{pmatrix}\dfrac{\partial n_z}{\partial y}-\dfrac{\partial n_y}{\partial z}\\ \dfrac{\partial n_x}{\partial z}-\dfrac{\partial n_z}{\partial x}\\ \dfrac{\partial n_y}{\partial x}-\dfrac{\partial n_x}{\partial y}\end{pmatrix}=\begin{pmatrix}E_y\left(\dfrac{\partial n_y}{\partial x}-\dfrac{\partial n_x}{\partial y}\right)-E_z\left(\dfrac{\partial n_x}{\partial z}-\dfrac{\partial n_z}{\partial x}\right)\\ E_z\left(\dfrac{\partial n_z}{\partial y}-\dfrac{\partial n_y}{\partial z}\right)-E_x\left(\dfrac{\partial n_y}{\partial x}-\dfrac{\partial n_x}{\partial y}\right)\\ E_x\left(\dfrac{\partial n_x}{\partial z}-\dfrac{\partial n_z}{\partial x}\right)-E_y\left(\dfrac{\partial n_z}{\partial y}-\dfrac{\partial n_y}{\partial z}\right)\end{pmatrix}, \tag{3.8}$$

And

$$(\mathbf{E}\cdot\nabla)\mathbf{n}=\left(E_x\frac{\partial}{\partial x}+E_y\frac{\partial}{\partial y}+E_z\frac{\partial}{\partial z}\right)\mathbf{n}=\begin{pmatrix}E_x\dfrac{\partial n_x}{\partial x}+E_y\dfrac{\partial n_x}{\partial y}+E_z\dfrac{\partial n_x}{\partial z}\\ E_x\dfrac{\partial n_y}{\partial x}+E_y\dfrac{\partial n_y}{\partial y}+E_z\dfrac{\partial n_y}{\partial z}\\ E_x\dfrac{\partial n_z}{\partial x}+E_y\dfrac{\partial n_z}{\partial y}+E_z\dfrac{\partial n_z}{\partial z}\end{pmatrix}. \tag{3.9}$$

On combining the results for $(\mathbf{E}\times\nabla\times\mathbf{n})$ and $(\mathbf{E}\cdot\nabla)\mathbf{n}$ we obtain:

$\mathbf{E}\times\nabla\times\mathbf{n}$ + $(\mathbf{E}\cdot\nabla)\mathbf{n}$ =

$$\begin{pmatrix}E_y\left(\dfrac{\partial n_y}{\partial x}-\dfrac{\partial n_x}{\partial y}\right)-E_z\left(\dfrac{\partial n_x}{\partial z}-\dfrac{\partial n_z}{\partial x}\right)\\ E_z\left(\dfrac{\partial n_z}{\partial y}-\dfrac{\partial n_y}{\partial z}\right)-E_x\left(\dfrac{\partial n_y}{\partial x}-\dfrac{\partial n_x}{\partial y}\right)\\ E_x\left(\dfrac{\partial n_x}{\partial z}-\dfrac{\partial n_z}{\partial x}\right)-E_y\left(\dfrac{\partial n_z}{\partial y}-\dfrac{\partial n_y}{\partial z}\right)\end{pmatrix}+\begin{pmatrix}E_x\dfrac{\partial n_x}{\partial x}+E_y\dfrac{\partial n_x}{\partial y}+E_z\dfrac{\partial n_x}{\partial z}\\ E_x\dfrac{\partial n_y}{\partial x}+E_y\dfrac{\partial n_y}{\partial y}+E_z\dfrac{\partial n_y}{\partial z}\\ E_x\dfrac{\partial n_z}{\partial x}+E_y\dfrac{\partial n_z}{\partial y}+E_z\dfrac{\partial n_z}{\partial z}\end{pmatrix}. \tag{3.10}$$

$$=\begin{pmatrix}E_x\dfrac{\partial n_x}{\partial x}+E_y\dfrac{\partial n_y}{\partial x}+E_z\dfrac{\partial n_z}{\partial x}\\ E_x\dfrac{\partial n_x}{\partial y}+E_y\dfrac{\partial n_y}{\partial y}+E_z\dfrac{\partial n_z}{\partial y}\\ E_x\dfrac{\partial n_x}{\partial z}+E_y\dfrac{\partial n_y}{\partial z}+E_z\dfrac{\partial n_z}{\partial z}\end{pmatrix}, \tag{3.11}$$

$$= \begin{pmatrix} \frac{\partial n_x}{\partial x} & \frac{\partial n_y}{\partial x} & \frac{\partial n_z}{\partial x} \\ \frac{\partial n_x}{\partial y} & \frac{\partial n_y}{\partial y} & \frac{\partial n_z}{\partial y} \\ \frac{\partial n_x}{\partial z} & \frac{\partial n_y}{\partial z} & \frac{\partial n_z}{\partial z} \end{pmatrix} \mathbf{E}, \tag{3.12}$$

$$= (\nabla \otimes \mathbf{n})\mathbf{E}. \tag{3.13}$$

On substituting eqn. (3.13) into eqn. (3.6) we obtain:

$$\mathbf{h} = (e_1 - e_3)[\mathbf{E}(\nabla \cdot \mathbf{n}) - (\nabla \otimes \mathbf{n})\mathbf{E}] - (e_1 + e_3)[(\mathbf{n} \cdot \nabla)\mathbf{E}]. \tag{3.14}$$

From equation (3.14) it can be deciphered that bulk deformations can be obtained when there is a gradient in the distribution of either the nematic director or an external electric field, E or both [25]. This expression suggests that in some cases, where a uniform electric field is present, only the $(e_1 - e_3)$ part contributes to the torque. Some of the common techniques used for finding $(e_1 - e_3)$ are through the measurement of the tilt of the optic axis of chiral nematic LC when the molecules are aligned in an ULH arrangement [28], or in a TN/HAN cell, while the sum can be determined using HAN or π-cells [29]. In this thesis, we use the standard chiral flexoelectric optic effect to determine the effective magnitude of the flexoelectric coefficients $|(e_1 - e_3)|$ (described in section 2.7).

3.5.2 Experimental Method

In order to obtain ϕ and hence $|(e_1 - e_3)|$ from the ULH technique, the LC samples C4, C6 and C7 were doped with a chiral dopant (S 811, E. Merck, Korea). The dopant has a helical twisting power of 58 μm^{-1}. The concentration range of the dopant was ~1.0 and 1.5% by weight. These concentrations were chosen so as not to alter the properties of the compounds by the addition of the dopant. It was also found that with higher weight percentage of the chiral additive ($\geq$ 2.5%), the optic axis especially in the case of C6 did not respond to the electric field. The optical pitch of the helix was determined in a 15μm planar cell by the measurement of the selective reflection using a UV/Vis/IR spectrometer (Section 2.7.1). These were determined to be $p \sim$ 498, 917 and 930 nm for C4, C6 and C7 respectively. The pitch values were found to be almost independent of temperature in the temperature window used for measurements.

The ULH texture was obtained by cooling a planar cell at a rate of 0.1 °C/min from the isotropic into the cholesteric phase, under the application of an alternating electric field of ~1V/μm, at a frequency of 100 Hz. It was observed that the materials readily aligned into a ULH structure on cooling from the isotropic phase under the influence of a moderate field, and no mechanical shearing was required to induce the texture. The texture of the ULH structure, observed in a 6μm planar cell filled with chiral sample C4 + 1.5% S 811, using a polarizing optical microscope at a reduced temperature of $T\text{-}T_{NI}$ = - 4°C, is shown in Figure 3.11 (b, c, d) for various positions of the optic axis with respect to the polarizer.

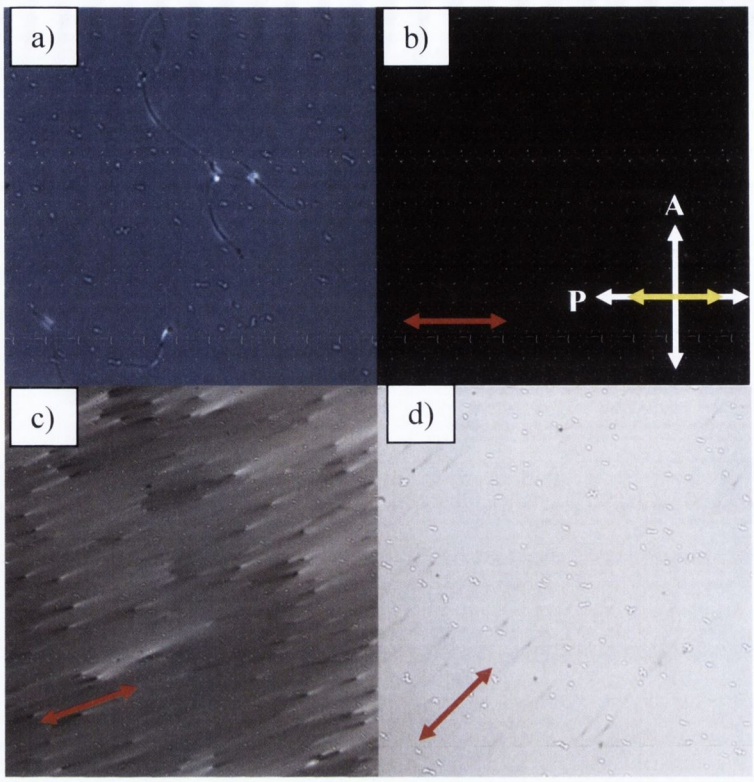

Figure 3.11: Textures obtained in a 6μm planar cell filled with (C4 + 1.5 % S 811): (a) classic cholesteric texture, obtained on cooling from the isotropic phase without field applied, at $T-T_{NI} = -4^{o}C$. (b) , (c) and (d) depict the ULH texture obtained on cooling the cell from the isotropic phase under the application of a moderate field (E = 1V/μm); the optic axis of the ULH lies parallel to the substrate in the direction of rubbing (depicted by the yellow arrow); the optic axis (depicted by the red arrow) in each case is aligned at angles of 0^{o} (b), 20^{o} (c) and 45^{o} (d) with respect to the polarizer P.

3.5.3 Results and Discussion

The tilt angle of the optic axis of ULH as a function of the applied electric field, at a frequency of 20 Hz, is plotted in Fig. 3.12 for C4, C6 and C7. The tilt angle is found to vary linearly with the field and is nearly invariant with temperature for all materials studied, irrespective of the chain length.

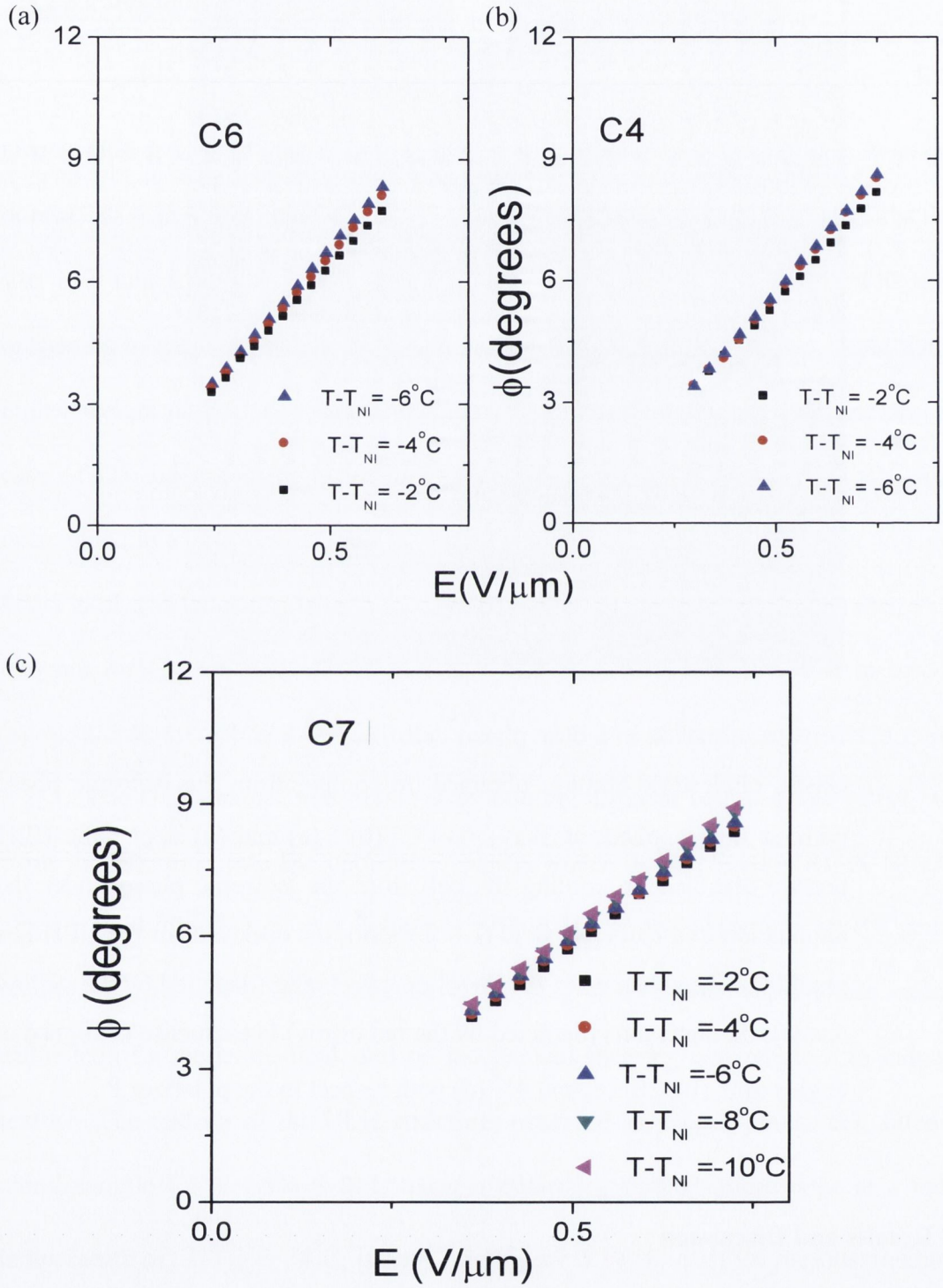

Figure 3.12: The magnitude of the tilt of the optic axis in the ULH structure of C6 (a), C4 (b) and C7 (c) as a function of the applied electric field E at a frequency of 20 Hz, for a range of reduced temperatures.

The magnitude of the effective flexoelectric coefficient $|(e_1 - e_3)|$ obtained using eqn. (2.39), by utilizing the experimental values of the pitch and tilt angle of the optic axis ϕ for an applied E, is shown in Fig. 3.13.

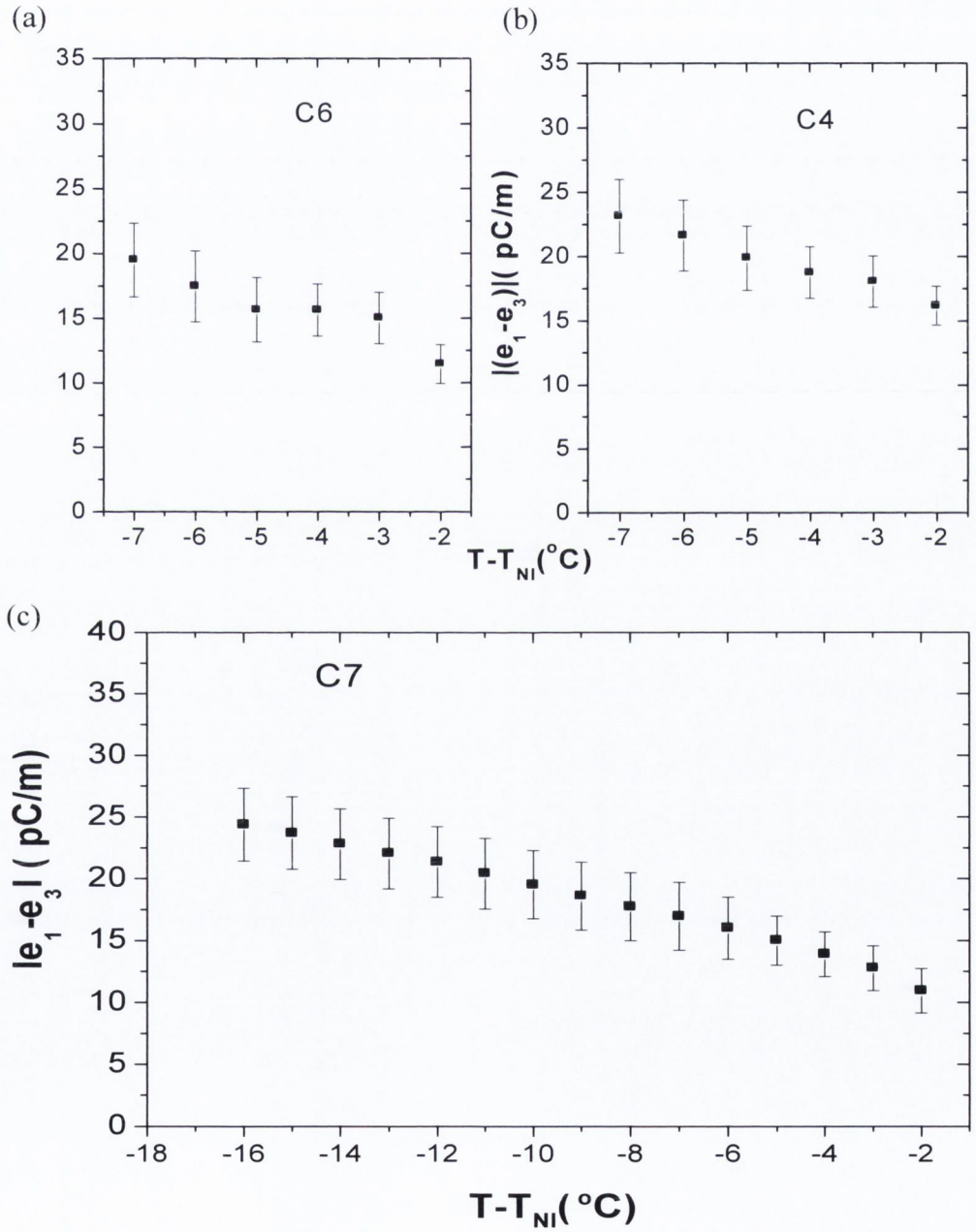

Figure 3.13: The magnitude of the effective flexoelectric coefficients $|(e_1 - e_3)|$ plotted as a function of the reduced temperature: (a) C6, (b) C4 and (c) C7.

For all the materials, it is found that the magnitude of $|(e_1 - e_3)|$ increases with a reduction in temperature. For C4, $|(e_1 - e_3)|$ increases from 14 pC/m for T-T_{NI} = - 2°C to ~ 23 pC/m at the lowest reduced temperature, while for C6 it increases from 11 to 19.5 pC/m and for C7 it increases from ~10.89 at T-T_{NI} = - 2°C to 24.4 pC/m at T-T_{NI} = - 16°C.

The sign of the effective flexoelectric coefficients [30] was determined by referring to eqn. (2.39), where a positive ϕ corresponds to a rotation in the positive sense around an axis in the direction of the applied field. The chiral agent S 811, used for the flexoelectric experiments in this chapter, is known to produce a left-handed helix, such that $p < 0$. Since K_{11}, $K_{33} > 0$ for all the materials, this implies that $(e_1 - e_3) < 0$; hence setting the sign to be negative.

The flexoelastic ratio e'/K as a function of the reduced temperature is shown in Fig. 3.14. e'/K is seen to be almost temperature invariant for all the materials. The ratio is greatest for C4, and lowest for C6, with values ~2.50, 1.6 and 1.8 $CN^{-1}m^{-1}$ for C4, C6 and C7, respectively. The temperature independence of e'/K also implies that both e and K depend on temperature similarly, and follow S^2 dependence, where S is the orientational order parameter. Such a dependence on the order parameter is as expected for a dipole mechanism of the flexoelectric effect [31]. Furthermore, the results indicate that the conformational freedom of the molecules is restricted, and this is in agreement with the conclusions derived by Jang et al. [4] for the dielectric studies in this series of bent-core materials.

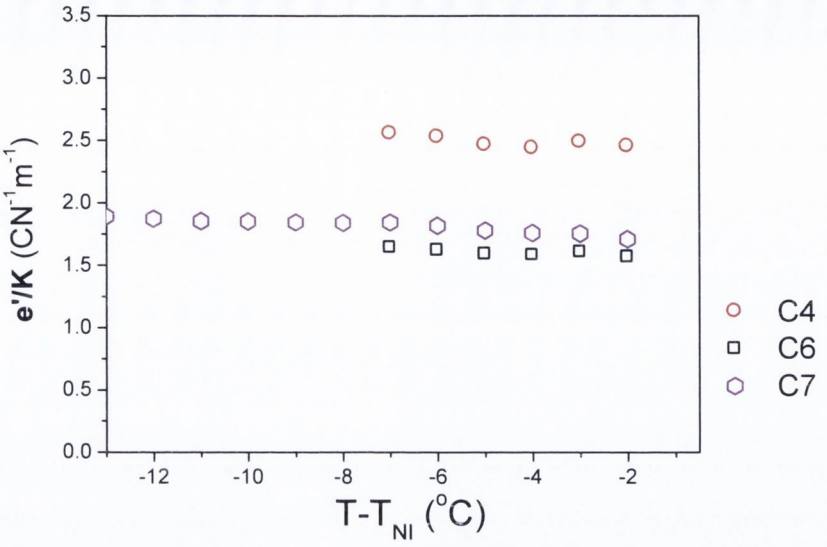

Figure 3.14: Flexo-elastic ratio e'/K ratio as a function of the reduced temperature.

The effective flexoelectric coefficient for C4, C6, and C7 is greater than that reported for conventional rod-like molecules that have similar magnitudes of the dipole moments [30], but its order of magnitude is comparable to other BCNs [19,21,32]. However, it is much lower than that found by Harden et al. [2]. Kumar et al. [32] found the value of $|e_3|$ comparable to those of the conventional nematics; nevertheless they proposed a model of non-polar clusters that would yield quadrupolar flexoelectricity [32] to explain the giant flexoelectricity in bent-core systems observed by Harden et al. [2]. They state that a giant value of the flexoelectric coefficient if confirmed can, in principle, be attributed to the non-polar clusters formed in the nematic phase. The flexoelectric coefficient should scale as the second power of the number of clustered molecules.

Due to the presence of Sm*C* like clusters in the entire nematic phase of C6 and C7, and their size increasing with a reduction in temperature, we should expect larger values for $|(e_1 - e_3)|$ in comparison to C4, following the model stated above. The

experimental results presented here, however, disagree with their conjecture. A possible explanation for this is that the quadrupolar cluster contributions to flexoelectricity may not be significant in the geometry used by us. Our measurement technique determines $|(e_1 - e_3)|$ by using a uniform electric field, while an electric field gradient is required to observe quadrupolar effects. Nonetheless, we surmise that the flexoelectric coefficient in BCN systems, though larger by a factor of up to four than calamitics [31], is not giant. Experimental results on the bent-core systems C4, C6, and C7 show that the clusters do not affect the elastic constants or the effective flexoelectric coefficients to a significant extent.

3.6 Conclusion

We studied the elastic and flexoelectric behaviour in the nematic phase of C4, C6 and C7 belonging to a homologous series of bent-core liquid crystals. Experimental results show that K_{33} is lower than K_{11} for all three compounds, irrespective of the chain length or presence/absence of clusters. Such low values of K_{33} seem to arise from the bent-shape of the molecules rather than been caused by the clusters. The effective flexoelectric coefficients $|(e_1 - e_3)|$ in the BCNs are obtained to be greater than those for conventional calamitics. The effective flexoelectric coefficient is found to be higher for C4 than for C6 and C7, by 20 to 25% in the common temperature range, even though the clusters are measurably absent in the nematic phase of this material. If clusters are thought to be responsible for increasing the effective flexoelectric coefficient, then our results contradict these. The shape of the bent-core molecule and its transverse dipole moment when considered together can account for the results obtained.

References

[1] M. Nagaraj, Y. P. Panarin, U. Manna, J. K. Vij, C. Keith and C. Tschierske, *Appl. Phys. Lett.*, **96**, 011106 (2010).

[2] J. Harden, B. Mbanga, N. Éber, K. Fodor-Csorba, S. Sprunt, J.T. Gleeson, A. Jákli, *Phys. Rev. Lett.*, **97**, 157802 (2006)

[3] Y. Jang, V. P. Panov, C. Keith, C. Tschierske, and J. K. Vij, *Appl. Phys. Lett.*, **97**, 152903 (2010).

[4] Y. Jang, V. P. Panov, A. Kocot, A. Lehmann, C. Tschierske and J. K. Vij, *Phys. Rev. E*, **84**, 060701(R) (2011).

[5] A. Jákli, M. Chambers, J. Harden, M. Madhabi, R. Teeling, J. Kim, Q. Li, G. G. Nair, N. Éber, K. Fodor-Csorba, J. T. Gleeson, S. Sprunt, *Emerging Liquid Crystal Technologies III*. Edited by L.C. Chen, Proceedings of the SPIE, **6911**, 691105-691105 (2008).

[6] S. H. Hong, R. Verduzco, J. C. Williams, R. J. Twieg, E. DiMasi, R. Pindak, A. Jákli, J. T. Gleeson and S. Sprunt, *Soft Matter*, **6**, 4819-4827 (2010).

[7] Pochi Yeh and Claire Gu, *Optics of liquid crystal displays*, Second Ed., Wiley Publications.

[8] W.H. de Jeu and W.A.P. Claassen, The Journal of Chem. Phys. **67**, 8 (1977); A. Scharkowski, H. Schmiedel, R. Stannarius and E. Weisshunn, *Mol. Cryst. Liq. Cryst.*, **191**, 1 (1990).

[9] M. Schadt, R. Buchecker, F. Leenhouts, A. Boller, A. Villiger and M. Petrzilka, *Mol. Cryst. Liq. Cryst.*, **139,** 1 (1986).

[10] M. R. Dodge, C. Rosenblatt, R. G. Petschek, M. E. Neubert and M. E. Walsh, Phys. Rev. E **62**, 5056 (2000).

[11] M. R. Dodge, R. G. Petschek, C. Rosenblatt, M. E. Neubert and M. E. Walsh, *Phys. Rev. E*, **68**, 031703 (2003).

[12] B. Kundu, R. Pratibha and N.V. Madhusudana, *Phys. Rev. Lett.*, **99**, 247802 (2007).

[13] P. Sathyanarayana, M. Mathew, Q. Li, V. S. S. Sastry, B. Kundu, K. V. Le, H. Takezoe and S. Dhara, *Phys. Rev. E*, **81**, 010702 (R) (2010).

[14] M. Majumdar, P. Salamon, A. Jakli, J. T. Gleeson and S. Sprunt, Phys. Rev. E **83**, 031701 (2011).

[15] F. Castles, S. M. Morris, and H. J. Coles, *AIP Advances*, **1**, 032120 (2011).

[16] F. Castles, S. M. Morris, and H. J. Coles, *AIP Advances*, **3**, 019102 (2013).

[17] C. Keith, A. Lehmann, U. Baumeister, M. Prehm, and C. Tschierske, *Soft Matter*, **6**, 1704 (2010).

[18] A. de Vries, *J. Mol. Liq.*, **31**, 193 (1986).

[19] P. S. Salter, C. Tschierske, S. J. Elston, and E. P. Raynes, *Phys. Rev. E*, **84**, 031708 (2011).

[20] G. P. Chen, H. Takezoe and A. Fukuda, *Liq. Cryst.*, **5**, 341 (1989).

[21] S. Kaur, J. Addis, C. Greco, A. Ferrarini, V. Görtz, J. W. Goodby, and H. F. Gleeson, *Phys. Rev. E*, **86**, 041703 (2012).

[22] M. Cestari, E. Frezza, A. Ferrarini, and G. R. Luckhurst, *J. Mater. Chem.*, **21**, 12303 (2011).

[23] R. B. Meyer, *Phys. Rev. Lett.*, **22**, 918 (1969).

[24] W. Helfrich, Phys. Lett. **35A**, 393 (1971); Z. Naturforsch., **26a**, 833 (1971).

[25] D. Dunmur, A Fukuda, G. R. Luckhurst, *Physical Properties of Liquid Crystals: Nematics*, Institution of Engineering and Technology, 2001.

[26] A. Derzhanski, A. G. Petrov, M. D. Mitov, *J. Phys. (France)*, **39**, 273 (1978).

[27] F. C. Frank, *Discuss. Faraday Soc.*, **25**, 19 (1958).

[28] J. S. Patel and R. B. Meyer, *Phys. Rev. Lett.*, **58**, 1538 (1987).

[29] P. J. Bos and K. R. Koehler/beran, *Mol. Cryst. Liq. Cryst.*, **113,** 329 (1984).

[30] F. Castles, S. C. Green, D. J. Gardiner, S. M. Morris and H. J. Coles, *AIP Advances*, **2**, 022137 (2012).

[31] I. Dozov, Martinot-Largarde and G. Durand, *J. de Phys. Lett.*, **44**, L-817(1983).

[32] P. Kumar, Y. G. Marinov, H. P. Hinov, U. S. Hiremath, C. V. Yelamaggad, K. S. Krishnamurthy, and A. G. Petrov, *J. Phys. Chem. B*, **113**, 9168 (2009).

Chapter 4

Elastic and Flexoelectric Properties of a Bimesogen

In this chapter, the dielectric, electro-optic and flexo-elastic properties of a bimesogen CBC11CB, exhibiting a second nematic phase, the twist-bend or N_{tb}, are investigated.

Contents

4.1 Introduction

Bimesogens or dimers are liquid crystals composed of two mesogenic units connected via flexible spacers. Altering the parity of the alkyl chain [1] in bimesogens has been reported to give rise to significant odd-even effects in these materials. For example, bimesogenic LC molecules composed of two rod-like molecules connected via an odd number of carbon spacer have a smaller value of the bend elastic constant compared to its even counterpart [2]. They also possess a larger flexo-elastic ratio [2]. The strong odd-even effects are often linked to the dependence of the molecular shape on the spacer linking the two mesogenic units, and by considering the spacer to exist in its all-*trans* conformation [1]. An even- spaced bimesogen has a zig-zag shape, while the odd-spaced dimer has a bent shape [1]. The molecular structure of liquid crystals can thus have a profound effect on the molecular shape, which can in turn trigger the advent of many peculiar properties, making the nematic phases of such molecules different from that formed by a conventional rod-like LCs.

In some odd bimesogens there also exists a second nematic phase in addition to the higher temperature ordinary nematic phase (N). Recent studies [3, 4] have indicated that this phase could indeed be the twist bend (N_{tb}), similar to the ones predicted by R.B. Meyer [5] and I. Dozov [6]. Theoretical studies by Dozov [6] showed that a twist-bend phase could arise if the bend elastic constant becomes negative, in which case in the ground state, the director would no longer be uniformly aligned as is in a conventional nematic, but is bent. He further predicted that the bend deformation does not exist on its own but requires an accompanying twist for the case of the twist-bend nematic phase (or splay for the splay-bend phase). Though the phase N_{tb} was initially proposed for

bent-core systems, it may be reasonable to extend it to LC bimesogens with odd spacers due to an overall bent shape of the molecules. The twist-bend nematic and some of its properties will be discussed in Chapter 5.

The theoretical studies pertaining to the mysterious yet fascinating N_{tb} phase is still in its initial stages. However, the parameters of ordinary nematic phase in these materials, the equations for which are well established, could also reveal useful information related to the underlying N_{tb} phase. Recently, Borsch al. [3] determined the elastic constants of a bimesogenic mixture possessing a negative value of $\Delta\varepsilon'$ and exhibiting the N_{tb} phase. They found the value of K_{33} to be as low as 0.77 pN when the temperature is lowered towards the N-N_{tb} phase. Similar results have also been found for other bimesogens [7]. Additionally, an electroclinic effect of flexoelectric origin was also demonstrated recently [4] in the N_{tb} phase.

In this chapter we determine the elastic constants K_{11} and K_{33}, effective flexoelectric coefficients $|(e_1 - e_3)|$ in the nematic phase, and the flexoelectric polarization P_f in the N and N_{tb} phase of a bimesogen CBC11CB. Furthermore, we investigate how the flexo-elastic parameters differ from rod-like and bent-core molecules, and other bimesogens that do not exhibit the second nematic phase.

The chapter is divided into three sections: the first part presents the results of dielectric and elastic constant studies conducted in the N phase; the second part discusses the results obtained for the effective flexoelectric measurements in the N phase; the third part concentrates on the flexoelectric polarization measured in both the N and N_{tb} phase.

4.2 Material under Study and XRD Results

The material under investigation in this chapter, CBC11CB is a symmetric dimer, synthesized in Hull, which consists of two cyanobiphenyl units linked by an alkyl chain of eleven methylene groups. The chemical structure and phase transition temperature of the sample is shown in Fig. 4.1. The material, on cooling from the isotropic phase, exhibits a transition to the ordinary nematic phase (*N*) and to the second nematic phase (N_{tb}) on further lowering the temperature.

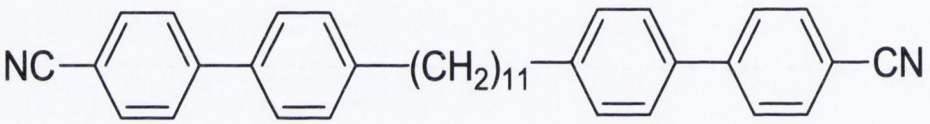

N_{tb} 108.7 N 125.3 Iso

Figure 4.1: Chemical structure and transition temperature of the material under study: CBC11CB.

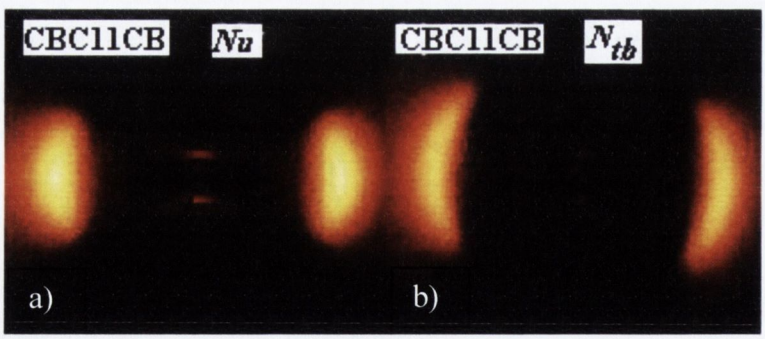

Figure 4.2: XRD patterns of the sample aligned by a 1T magnetic field on cooling. (a) ordinary nematic phase, T =120°C (b) N_{tb} phase, T =100°C. For more clarity, intensity from the isotropic phase was subtracted from both patterns.

The XRD patterns of CBC11CB were obtained by Dr. Mehl's group in Hull (Fig. 4.2). They found that the X-ray diffraction patterns showed typical features of a nematic phase: a diffuse wide angle scattering located around the equator, and a diffuse like scattering on the meridian in the small angle region. Furthermore, the position and intensity of the small angle scattering only changed slightly as temperature was decreased from the N to the N_{tb} phase. No significant increase in the small angle intensity was found to occur on transition into the low temperature N_{tb} phase; this confirmed the absence of layer formation and excluded the lower temperature phase to be a smectic phase.

Part I

4.3 Dielectric and Elastic Properties

4.3.1 Experimental Method

The experimental setup to evaluate the real part of the dielectric permittivity includes an optical microscope (Leitz laborlux 12 POL S) with crossed polarizers, a data acquisition board (NI-USB 6216), a photodiode with an I-V converter and a software lock-in amplifier (refer to Figure 3.5). The setup measures the AC current response from which it evaluates the capacitance; the capacitance is then converted into the respective permittivity values using the equation $\varepsilon' = C/C_0$, where C_0 is the capacitance of the empty cell.

The parallel and perpendicular components of the dielectric constants, $\varepsilon'_{\parallel}$ and $\varepsilon'_{\perp}$ were obtained by applying an AC field of up to $10V_{pk}$ (~1.5V/μm) at a frequency of 1 kHz to a planar cell of thickness 6.7 μm. A field of $10V_{pk}$ was found sufficient to enable complete switching of the cell to the homeotropic state (Fig. 4.3). This allowed

the determination of both $\varepsilon'_{\parallel}$ and $\varepsilon'_{\perp}$ from a single homogeneous cell for the maximum applied field possible from the set-up ($10V_{pk}$). $\varepsilon'_{\perp}$ was obtained as the permittivity value much below the *Freedericksz* transition, while $\varepsilon'_{\parallel}$ corresponds to the value at higher voltages when the molecules are aligned perpendicular to the substrate and the permittivity value is saturated. The setup waits 30 seconds between consequent measurement points at a given temperature, in order to ensure that the molecules are completely switched on field application, or reverted to their original state on field removal. For the maximum applied voltage capable from our setup ($10V_{pk}$) and measurement conditions used for the *N* phase, no noticeable switching was observed on transition into the N_{tb} phase; hence the dielectric data for the N_{tb} phase has been excluded in our studies.

The splay and bend elastic constants were determined at frequency 1 kHz in the ordinary nematic phase from the voltage dependent retardation data using the method described in Section 2.6.

4.3.2 Results and discussion

4.3.2.1 Dielectric Constant Measurements

The plot of the real part of dielectric permittivity as a function of voltage at frequency 1 kHz is plotted in Fig. 4.3 for a reduced temperature $T-T_{NI} = -4^{o}C$. A field of $10V_{pk}$ is sufficient to align the cell homeotropically and the dielectric constant tends to saturate at this voltage, as seen from the figure. The value of $\varepsilon' << V_{th}$ corresponds to $\varepsilon'_{\perp}$ and the value at voltages much higher than V_{th} corresponds to the parallel component of the dielectric permittivity, $\varepsilon'_{\parallel}$.

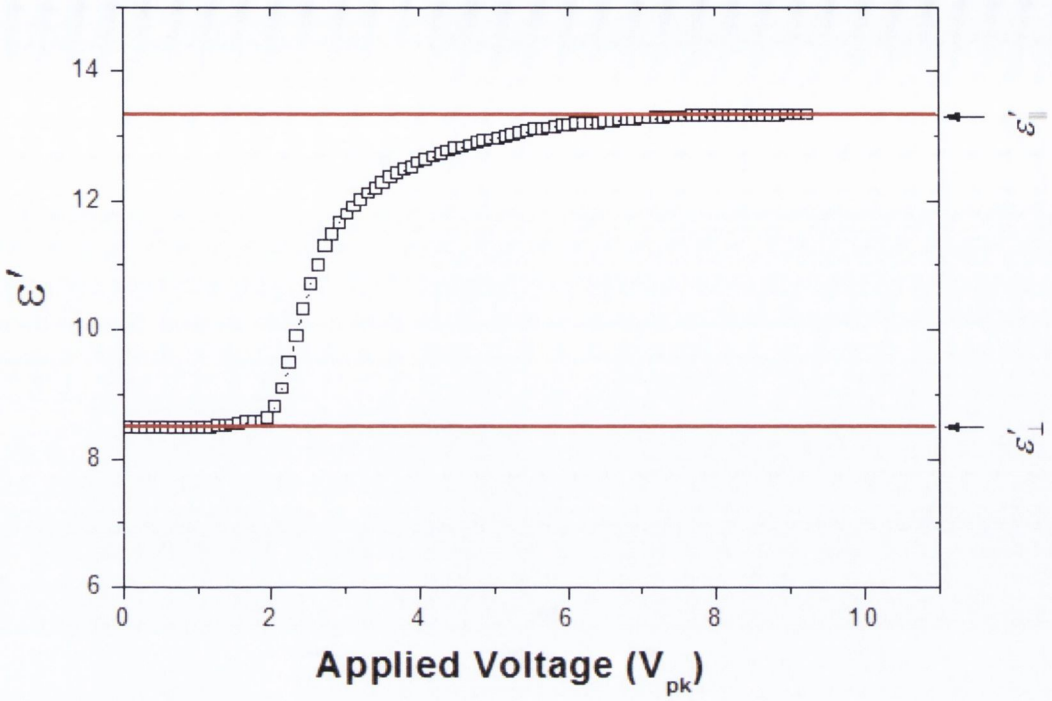

Figure 4.3: Real part of dielectric permittivity as a function of applied voltage for reduced temperature $T-T_{NI}= -4^{o}C$ at frequency of 1 kHz.

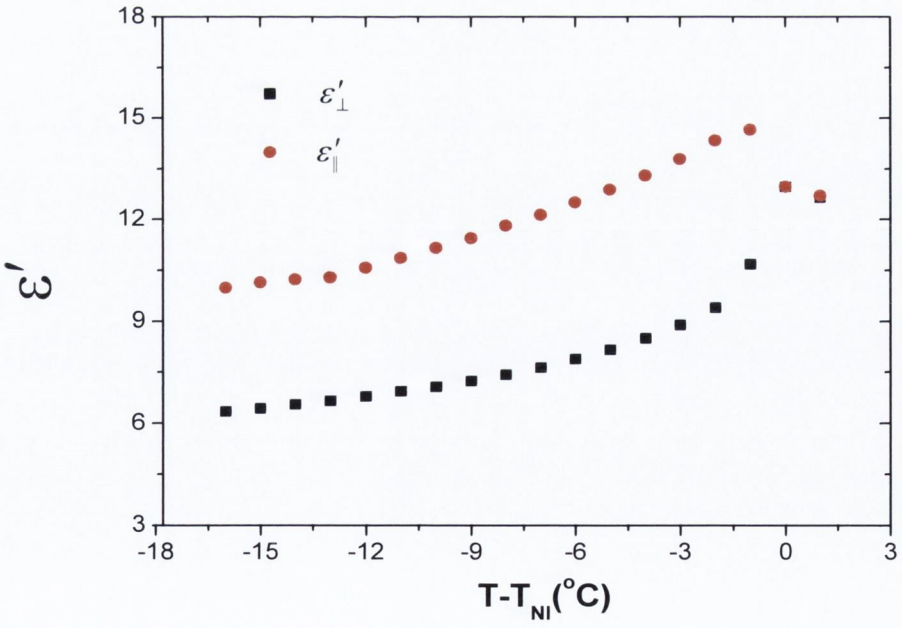

Figure 4.4: Permittivity as a function of reduced temperature for frequency of 1 kHz.

The variation of dielectric constants as a function of the reduced temperature is plotted in Figure 4.4. The value of $\Delta\varepsilon'$ is positive throughout the nematic phase and shows no sign reversal as a function of decreasing temperature. The parallel component of the permittivity shows an increase on cooling from the isotropic phase, as expected in a material with positive $\Delta\varepsilon'$, however it is seen to decrease as the temperature is reduced further. The perpendicular permittivity drops sharply on transition to the nematic phase, and decreases steadily as the temperature is further reduced. The value of $\Delta\varepsilon'$ is ≤ 4.9 in the *N* phase. Similar trends were observed for other odd-symmetric bimesogens [8, 9], where the temperature dependence of the permittivities was linked to a change in conformational distribution caused by the increase in the orientational order with decreasing temperature.

4.3.3 Elastic Constants

An example of the theoretical fit to the retardation curve for a reduced temperature, $T\text{-}T_{NI} = -9^{o}C$ is shown in Figure 4.5. The temperature variation of the splay and bend elastic constants hence obtained is plotted in Fig. 4.6.

It can be clearly seen that K_{11} increases as the temperature is reduced. However K_{33} shows a slight increase at higher temperature and progresses to fall much below K_{11} as the temperature is further reduced. At the lowest temperature for which the elastic constants were measured, the bend elastic constant is seen to decrease by a factor of almost 3 below K_{11}.

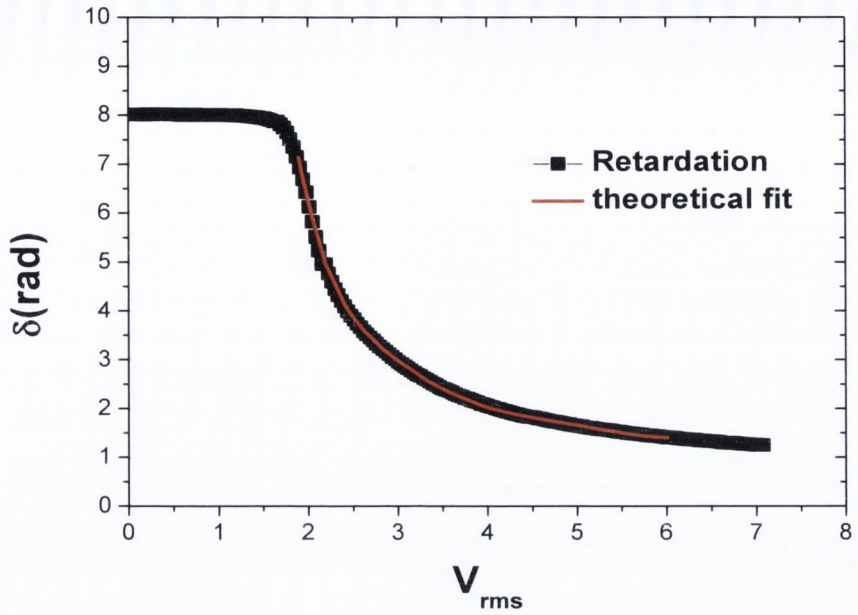

Figure 4.5: Retardation as a function of applied voltage for $T-T_{NI}= -9^{o}C$ at frequency of 1 kHz.

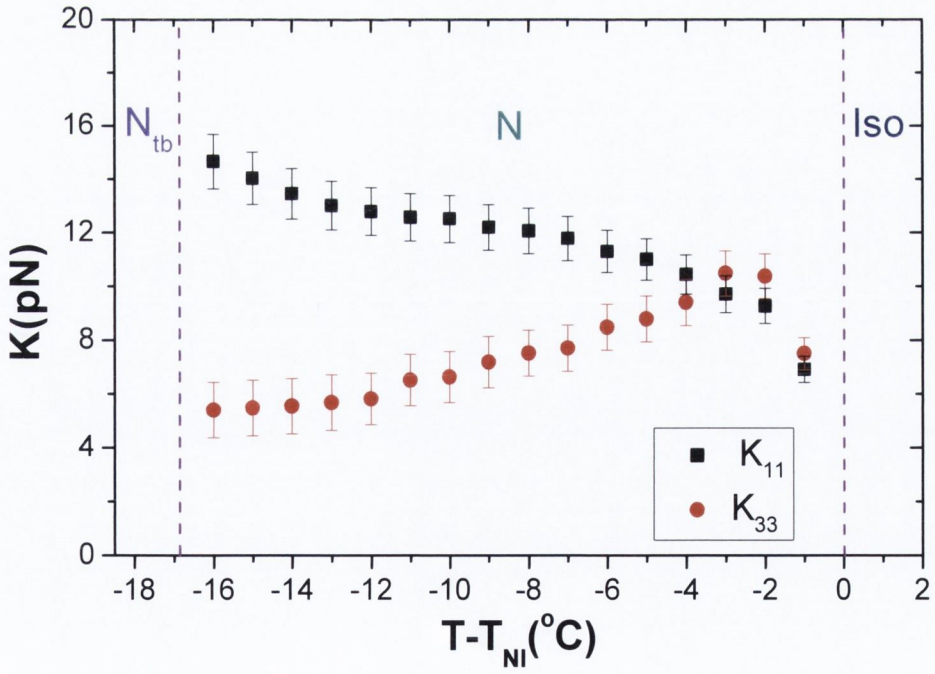

Figure 4.6: Elastic constants as a function of reduced temperature. The experimental errors in the estimation of the elastic constants are shown by vertical arrows.

Interestingly, a feature similar to pre-transitional divergence is observed for K_{11} close to the N-N_{tb} transition temperature, while no such change is observed for the bend elastic constant. The value of K_{33} at higher temperatures is particularly intriguing as it tends to increase slightly above K_{11} after transition to the nematic phase, only to fall steadily with decreasing temperatures as it approaches the N-N_{tb} transition. Within the measured temperature range, even though K_{33} decreases as the temperature is lowered, the sign of K_{33} is still positive.

The ratio of splay to bend elastic constant K_{33}/K_{11} is shown in Fig. 4.7. Its value is seen to increase to just above 1.0 after transition to the nematic phase. However, the ratio decreases steadily as the temperature is further lowered in the nematic phase. As the N_{tb} transition temperature is approached, the value of K_{33}/K_{11} decreases to as little as ~0.36.

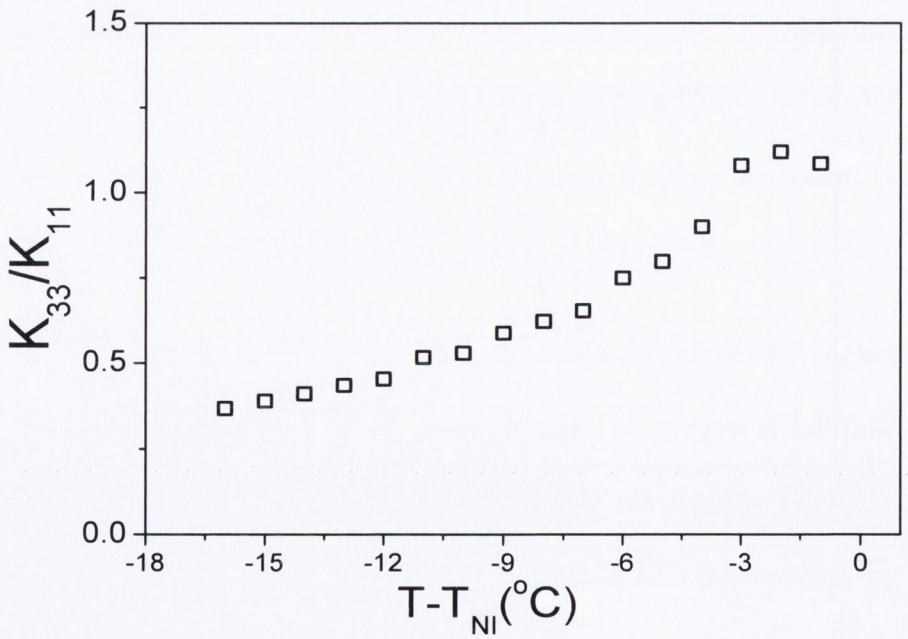

Figure 4.7: Ratio of K_{33}/K_{11} as a function of the reduced temperature.

Figure 4.8 shows the effective elastic constant K, defined as $(K_{11}+K_{33})/2$. It can be seen that after an initial increase close to the isotropic-nematic transition K becomes nearly invariant at lower temperatures.

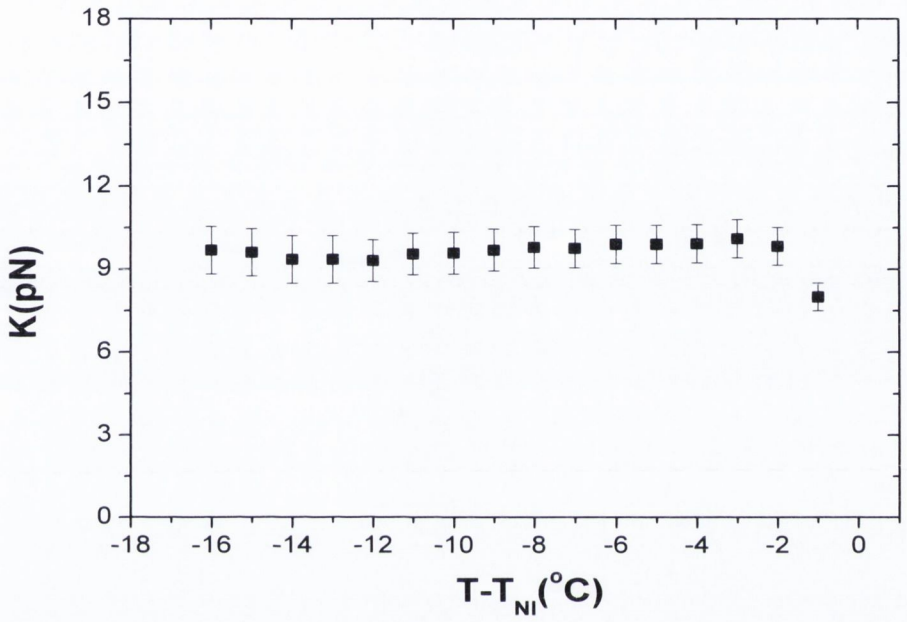

Figure 4.8: The effective elastic constant as a function of reduced temperature.

The temperature behaviour of K_{11} in CBC11CB is typical of that found in nematic materials, whereas that of K_{33} is not. The initial increase of K_{33} near the transition and subsequent decrease with temperature is vaguely reminiscent of the BCNs where an initial increase is thought to be due to an increasing orientational order (S), and with deceasing temperatures coupling of the bend distortion with S increases leading to a decrease in the value of K_{33} [10]. Calculations by Cesstari et al. [11] have found similar results for the elastic constants of odd fluorinated bimesogens, with K_{33} decreasing as the orientation order is increased. They concluded that there is a strong influence of the molecular curvature on the bend elastic constants of odd dimers.

Experimental results on an odd ether linked bimesogen [2], which does not exhibit the N_{tb} phase, also revealed that $K_{33} < K_{11}$. The temperature dependence of K_{11} is similar to our results obtained for CBC11CB; however the bend elastic constant, though smaller than K_{11}, is found to be almost temperature independent. For CBC11CB, the behaviour of K_{33} with decreasing temperature is similar to the results obtained in refs. [3] and [7]. In reference [7] the authors found a small increase in K_{33} just prior to the transition to the twist-bend nematic phase. Though we did not observe any increase in its value close to the transition, we find that the value tends to become nearly temperature independent close to the N-N_{tb} transition temperature.

The value of K_{33} obtained by us, for temperatures down to 0.6°C above the N-N_{tb} transition, do not seem to go to zero or fall below it. Hence, it is deviating from one of the conditions required for the formation of the N_{tb} phase, as predicted by Dozov [6]. However, our experimental findings suggest that a small value of K_{33} is important for the existence of the N_{tb} phase. In addition, it also requires $K_{11} > 2K_{22}$ for the twist-bend nematic phase to be stable [6]. Our measurement technique does not allow for the evaluation of K_{22}, however it is possible that this condition might be fulfilled, as has already been calculated for bimesogens based on molecular field approach [8] and using dynamic light scattering [7].

Part II

4.4 Flexoelectric Measurements

4.4.1 Experimental Technique

In order to obtain the effective flexoelectric coefficients using the converse electro-optic technique, a cholesteric mixture of CBC11CB was prepared by introducing a small concentration (~ 3%) of a high-twisting power chiral dopant R5011 (Merck, Korea) to the original sample, and this produced a short pitch mixture. The chiral agent is a right handed dopant with a helical twisting power (HTP) of ~100 μm^{-1}. Such low concentration of the additive ensures that the properties of the host sample are not drastically modified because of the introduction of the chiral dopant. The sample was filled via capillary action by heating the empty cells into the isotropic phase using a temperature controller (Eurotherm 2604). The optical pitch was obtained by measuring the wavelength band for selective reflection for light normally incident on a 5μm planar cell by a UV/Vis Spectrometer (Avaspec-2048).

Since the ULH structure is not formed spontaneously on cooling a planar cell from the isotropic phase due to the minimum free energy configuration of a chiral nematic being a Grandjean texture, the cell was cooled at a rate of 0.1^{o}C/min under the influence of a moderate electric field (E ~ 2 V/μm) at a frequency of 100 Hz. As with the BCNs studied in Chapter 3, we noted that the materials readily aligned into a ULH structure on cooling from the isotropic phase under the influence of the applied field, and no mechanical shearing was required to induce the texture.

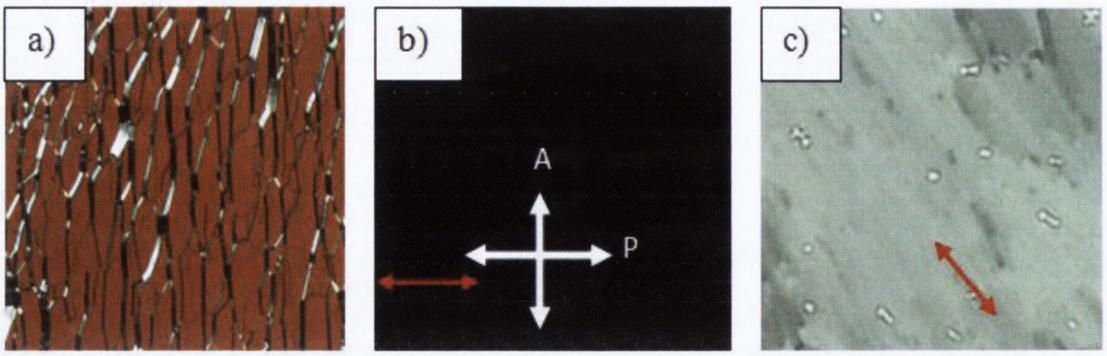

Figure 4.9: (a) Cholesteric texture obtained in a planar cell under crossed polarizers, on cooling from the isotropic phase without field applied, at $T\text{-}T_{NI} = -3^{o}C$. (b) and (c) depict the ULH textures captured by a 20x lens, obtained on cooling the cell from the isotropic phase under the influence of a moderate electric field; the optic axis (depicted by the red arrow) in each case is aligned at angles of 0^{o} (b) and 45^{o} (c) with respect to the polarizer P.

The texture obtained in the ordinary nematic phase of the chiral mixture (Fig. 4.9(a)) is typical of classical cholesteric liquid crystals in a planar aligned cell. Hence the technique of obtaining the effective flexoelectric coefficient using the ULH technique is valid for the higher temperature N^* phase. However in the N_{tb} phase, rather non-uniform rope like textures were observed (POM texture is given in the Appendix), which are very different from the higher temperature N^* phase. This implies that the ULH method cannot be employed to evaluate $|(e_1 - e_3)|$ in this phase. The characterization of the N_{tb} phase in the chiral mixture is a topic for future investigation, and hence, is not discussed further in this chapter.

The texture of the ULH structure observed in the N^* phase using a polarizing optical microscope (Olympus BX51) for a reduced temperature of $T\text{-}T_{NI} = -3^{o}C$ is shown in Figure 4.9 (b, c) for various positions of the optic axis with respect to the

polarizer. Once a reasonable ULH texture was obtained, the tilt angle was measured by using the method described in Section 2.7.2.

4.4.2 Results and Discussion

Figure 4.10 shows the variance of the optical pitch p in the N^* phase as a function of the reduced temperature. The pitch was seen to increase from ~ 420 to ~ 535 nm as the temperature was reduced. The divergence of the pitch in the N^* phase on cooling is presumably an intrinsic property of the chiral agent R5011, as the same material when introduced in a bent-core system [12] produced a pitch that varied significantly with reduced temperature.

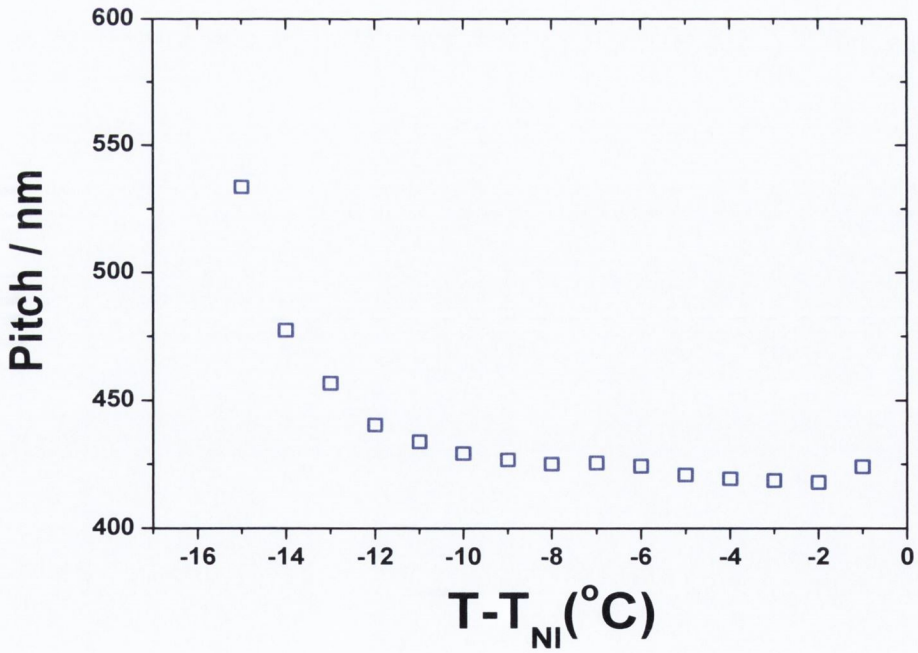

Figure 4.10: Variation of the optical pitch length in the N^* phase as a function of reduced temperature.

Figure 4.11 presents tan ϕ plotted as a function of the electric field for several reduced temperatures. A linear relationship between tan ϕ and the electric field is observed, as predicted by equation (2.39), for the measured temperatures.

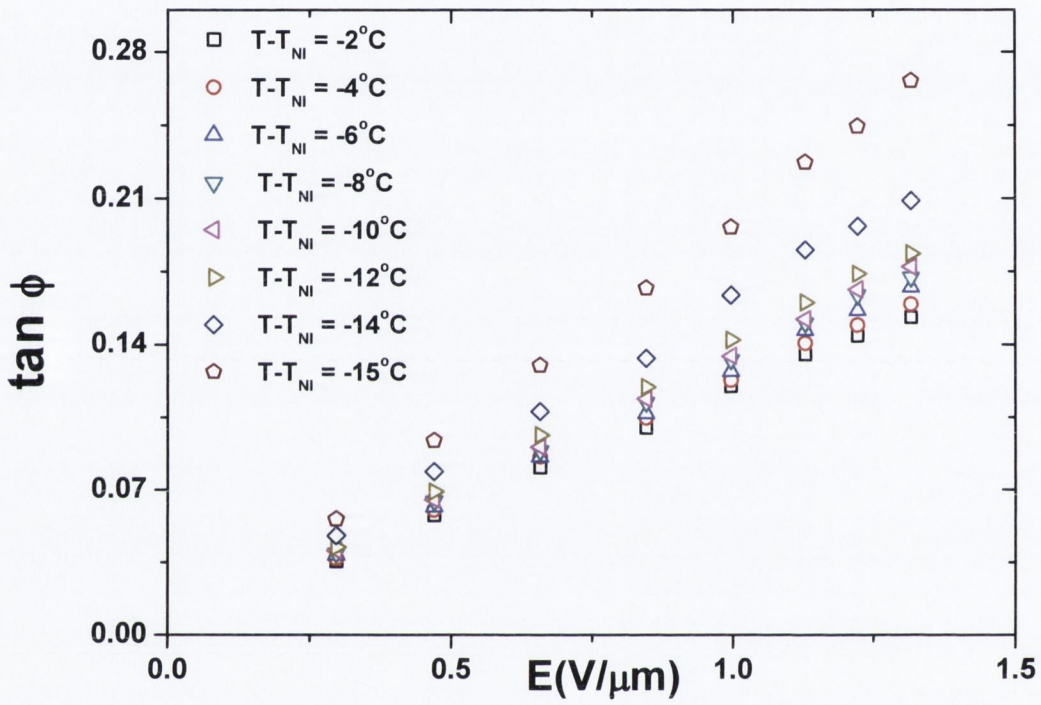

Figure 4.11: Variation of tan ϕ as a function of the applied field for a range of reduced temperatures.

As seen from the Figure, ϕ shows noticeable increase for temperatures close to the N-N_{tb} phase. The temperature dependence of the flexoelectrically induced rotation angle at lower temperatures is presumably due to the increase in the helical pitch as the temperature decreases (see Fig. 4.10); the tangent of the tilt angle is directly proportional to p, as seen from Eqn. (2.39).

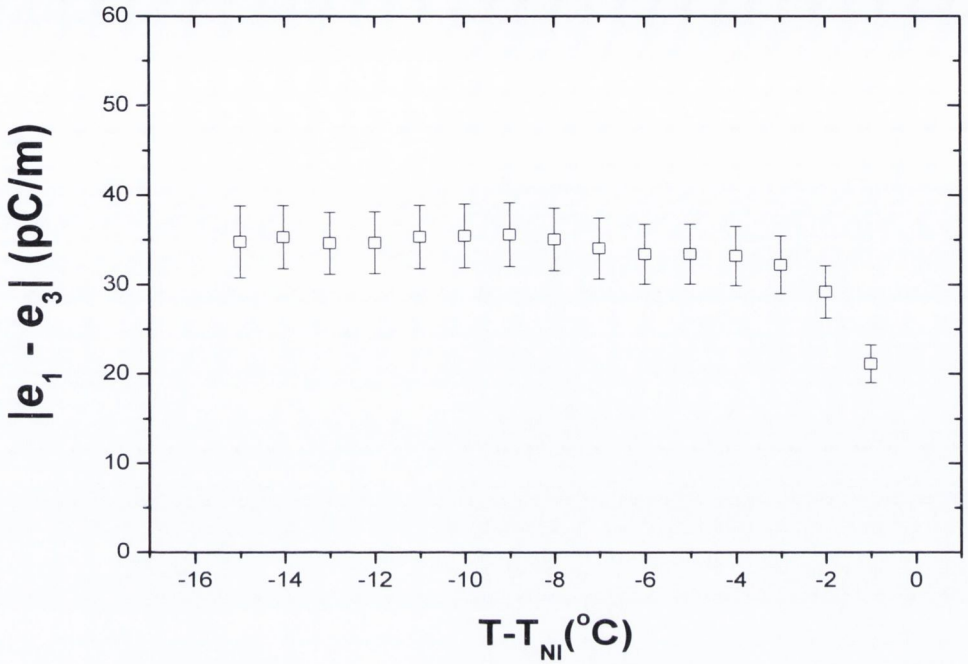

Figure 4.12: Effective flexoelectric coefficient as a function of the reduced temperature.

Figure 4.12 presents the temperature dependence of the effective flexoelectric coefficient $|(e_1 - e_3)|$. The sign of the effective flexoelectric coefficients [13] is determined by referring to Eqn. (2.39), where a positive ϕ corresponds to a rotation in the positive sense around an axis in the direction of the applied field. The chiral agent R5011 is known to produce a right-handed helix, such that $p > 0$. Since K_{11}, $K_{33} > 0$ for CBC11CB, this implies that $(e_1 - e_3) > 0$; hence setting the sign to be positive.

From Fig. 4.12 it can be seen that the value of $|(e_1 - e_3)|$ increases from 21 pC/m at $T-T_{NI} = -1^{o}C$ to ~35 pC/m at the lowest temperature for which these measurements were performed. $|(e_1 - e_3)|$ increases marginally at higher temperatures and becomes nearly independent of it as the temperature is decreased further. It would have been very

interesting to obtain data at temperatures very close to the N_{tb} phase; however the quality of alignment and the resulting signal was seen to degrade significantly at these temperatures, rendering it nearly impossible to carry out measurements at these points.

The temperature dependence of the flexo-elastic ratio e'/K is plotted in Fig. 4.13. e'/K is seen to be slightly temperature dependent at higher temperatures, and becomes nearly independent of it at lower temperatures. The ratio is observed to increase from ~1.46 to ~1.85 $CN^{-1}m^{-1}$ as the temperature is reduced.

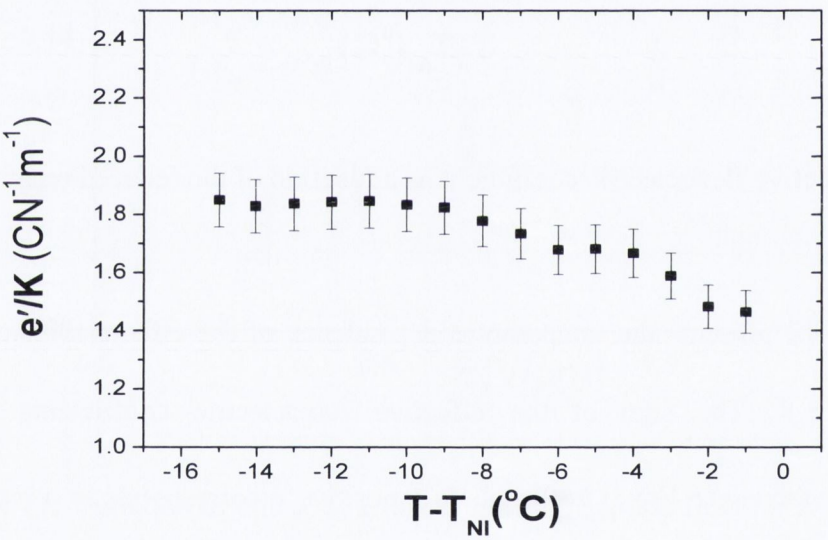

Figure 4.13: Flexo-elastic ratio as a function of reduced temperature.

Flexoelectric studies in the nematic phase of bimesogenic molecules exhibiting a lower temperature twist-bend phase have not been reported yet, hence making it difficult to draw comparisons with similar systems; however the value of $|(e_1 - e_3)|$ obtained here are much greater than that reported for calamitic molecules [13].

For a well known liquid crystal 5CB, the effective flexoelectric coefficient was determined to be 7.10 pC/m at T = 25°C [13], which is smaller by a factor of almost 5 in comparison to the value obtained for CBC11CB. Due to the average bent shape of the molecules, the bend flexoelectric coefficient is expected to be greater in odd bimesogens. This possibly results in higher values of the effective flexoelectric coefficients in CBC11CB when compared to conventional calamitics.

For an odd symmetric bimesogen FFO9OCB [2], $|(e_1 - e_3)|$ was estimated to be in the range of ~ 12- 16 pC/m (e' ~ 6-8 pC/m). Our values are determined to be almost twice of that. In some ester linked asymmetric bimesogens, e' ($=|(e_1 - e_3)|/2$) was estimated to be as high as ~16 for the compound F3FE9ECB at temperature T/T_{NI} ~0.94 [14], which is similar to the results obtained by us. The difference in the value of the effective flexoelectric coefficient from other bimesogenic systems at comparable temperatures may arise from the different electric structure of the dimers, as well as their geometry or flexibility [15].

If a direct comparison is possible with BCNs on account of the bent shape of the odd bimesogenic molecules and similar temperature dependence of the elastic constants (especially K_{33}), the values for $|(e_1 - e_3)|$ presented here are slightly higher than that estimated by us in the homologous series of the bent core molecules, studied in Chapter 3. This difference could have arisen due to an increased flexibility of the bimesogens which allows for a range of different conformers, hence deviating from a true bent structure.

Part III

4.5 Flexoelectric Polarization Measurement using Pyroelectric Technique

4.5.1 Theoretical Background

The pyroelectric technique is an extremely sensitive method used to measure the flexoelectric polarization P_f in a hybrid aligned nematic (HAN) cell. In a HAN cell, one of the substrate is coated for planar alignment and the other for homeotropic. In such a configuration the director field has a permanent splay-bend deformation, which generates a flexoelectric polarization P_f.

The pyroelectric technique yields measurements of very low values of P_f with zero external fields applied to a LC cell. In general for a LC, the pyroelectric coefficient γ is defined as [16]:

$$\gamma = \frac{dP_s}{dT}, \tag{4.1}$$

where dP_s/dT is the rate of change of the spontaneous polarisation P_s with temperature. For a hybrid aligned (HAN) cell, the flexoelectric polarization P_f takes the place of P_s [16]. Hence Eqn (4.1) can be re-written as:

$$\gamma = \frac{dP_f}{dT}. \tag{4.2}$$

When a HAN cell is irradiated by a short pulse of light, a pyroelectric current i_p is produced by the sample:

$$i_p = S\frac{dP_f}{dt} = S\frac{dP_f}{dT} \times \frac{dT}{dt}, \tag{4.3}$$

where dT/dt is the time rate of change of temperature of the sample due to the heating by the light pulse and S is the area of the electrodes. On re-arranging the terms we get:

$$dP_f = \frac{1}{S(dT/dt)} i_p dT. \tag{4.4}$$

Integrating both sides yields the following equation for P_f:

$$P_f(T) = -\frac{1}{S(dT/dt)} \int_{T_0}^{T} i_p dT, \tag{4.5}$$

where T_0 is the temperature above the isotropic to nematic phase transition and T is the temperature for which P_f is to be calculated.

Since the quantity dT/dt is unknown, the absolute value of P_f (T) cannot be calculated by the measurements alone. It requires calibration by another method in order to provide an absolute value of polarization at a certain temperature. In this thesis, we use the current reversal technique (Section 2.3.1) [17] in conjunction with the pyroelectric technique to determine the necessary calibration factor.

4.5.2 Experimental Setup

The schematic representation of the pyroelectric setup used to obtain the flexoelectric polarization is shown in Fig. 4.14. The temperature controller allowed the sample temperature to be regulated with steps of 0.1°C.

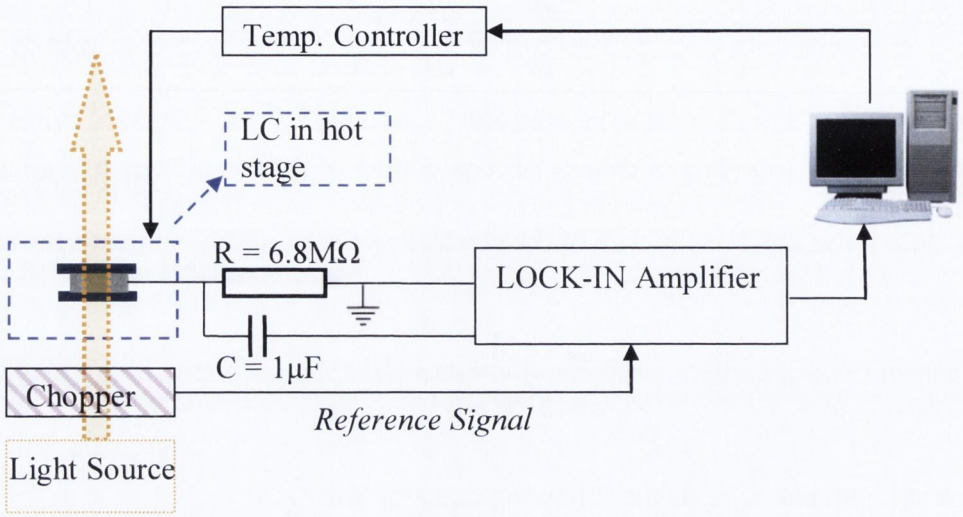

Figure 4.14: Pyroelectric Set-up.

A light of constant intensity with time was chopped at a fixed frequency. The pyroelectric signal usually has a very low level (of the order of microvolts), hence a Lock-in Amplifier (Stanford Research System / Model SR830 DSP) triggered at the light modulation frequency has to be used in order to obtain reasonable accuracy of the measurements. The modulation frequency of 170 Hz was chosen as it was noted to produce the best signal to noise ratio. The measurements for CBC11CB were made in the absence of an electric field, hence potential effects such as ionic screening and coupling of dielectric anisotropy to the electric field were neglected.

The calibration of the pyroelectric signal, required to obtain the absolute value of the pyroelectric coefficient for CBC11CB, was provided by a well-known ferroelectric LC 120F1M7 (chemical structure and phase transition temperature is provided in the Appendix), whose spontaneous polarization was determined independently using the well-known current repolarization technique (results are shown in Fig. 4.15). For the pyroelectric effects to appear in this material, the helix of the

smectic-C^* phase has to be unwound. For this purpose, we applied an electric field of 1V/μm to the planarly aligned sample from an arbitrary waveform generator (HP 33120 A). The pyroelectric signal generated for 120F1M7 was then recorded using the same measurement conditions as for CBC11CB. The integrated pyroelectric signal was then scaled to the value of P_s (evaluated using the field reversal method) at a particular temperature. We used the value of P_s = 64 nC/cm^2 at T = 77°C and this yielded the necessary calibration factor. Fig. 4.15 represents the temperature dependence of the pyrolectric signal and P_s in the 120F1M7 liquid crystal. The sharp peak that appears at 93°C in the pyroelectric signal corresponds to the SmA → SmC^* phase transition. The integrated pyroelectric signal (green line) for 120F1M7 was found to be in good agreement with the temperature dependence data of the spontaneous polarization measured using the field reversal technique (black hollow squares). In the nematic phase of the classical calamitic 5CB, the value for P_f obtained using our setup is similar to that reported in literature [16], thus confirming the validity of our results.

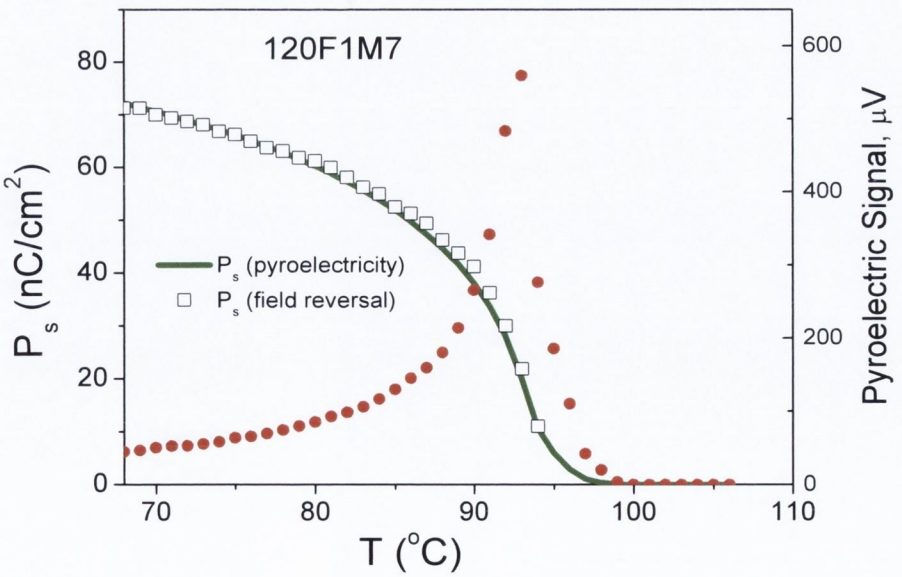

Figure 4.15: Temperature dependence of the pyroelectric signal (red circles), and spontaneous polarization of 120F1M7 measured using field reversal (black squares) and pyroelectric technique (green line).

4.5.3 Results and Discussion

Figure 4.16 shows the temperature dependence of the pyroelectric signal and the absolute value of flexoelectric polarization P_f (obtained by integrating the pyroelectric coefficient) for a 7.7 μm hybrid cell filled with CBC11CB. The peaks that appears at T = 126.6 ^{o}C and 107 ^{o}C (on cooling the liquid crystal) correspond to the *Iso-N* and *N-N$_{tb}$* phase transitions, respectively

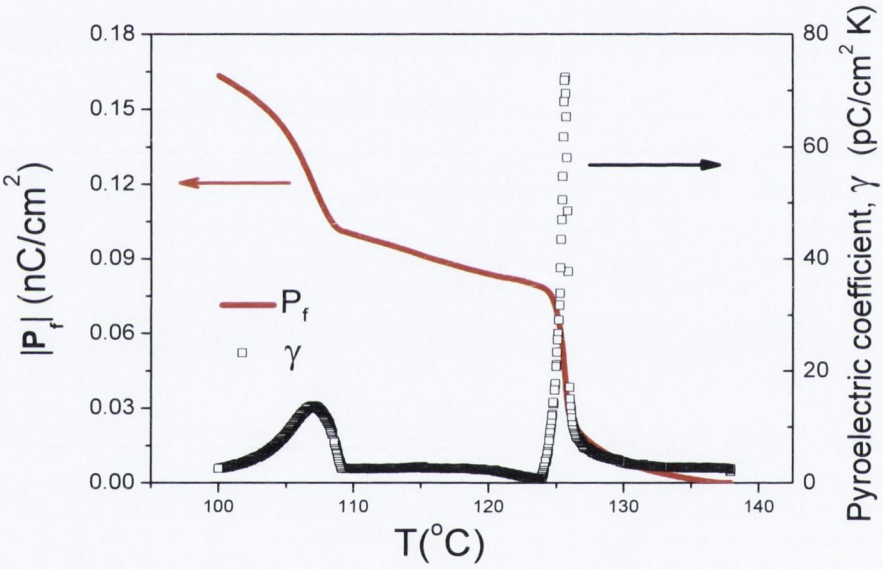

Figure 4.16: Temperature dependence of the pyroelectric signal (black squares) and flexoelectric polarization (red line) of CBC11CB.

The pyroelectric signal in the isotropic phase is not zero, presumably due to a strong surface polarization present in the sample [18]. This vector was subtracted when calculating the P_f. The magnitude of P_f increases on transition from the isotropic phase and is seen to grow marginally from 0.08 to 0.10 nC/cm^2 as the temperature is further reduced in the nematic phase. It is observed to increase steadily on cooling at the

transition into the N_{tb} phase. The value reaches almost 0.17 nC/cm^2 at the lowest temperature for which the measurements were carried out. Our results show that the N_{tb} phase has a large flexoelectric polarization compared to the classical nematic phase, by a factor of almost 2. This is also possibly the source of the electroclinic effect observed in this phase by Meyer et al. [3].

In the literature, flexoelectric polarization has been determined for a calamitic system in the nematic phase of 5CB [16]. This was found to be 0.04 nC/cm^2. By comparison, $|P_f|$ determined for CBC11CB is larger by a factor of almost 2.5 times in the N phase and ~ 4 times in the N_{tb} to that obtained for conventional rod-like mesogens. Due to the overall bent shape of the odd-bimesogens, the magnitude of the bend flexoelectric coefficient can be higher in the N phase of these materials. This possibly gives rise to high values of P_f in CBC11CB in comparison to rod-like molecules. The large values of K_{11} and $|(e_1 - e_3)|$ in the N phase and P_f in the N and N_{tb} phase indicate that not only bend, but splay deformations may also influence the macroscopic effects exhibited by the N_{tb} phase.

4.6 Conclusion

We have obtained the splay and bend elastic constants, the effective flexoelectric coefficient, $|(e_1 - e_3)|$, in the nematic phase and flexoelectric polarization in both the ordinary nematic and twist nematic phase of a bimesogen CBC11CB. We found that K_{11} increases with decreasing temperature, but the value of K_{33} tends to fall steadily after an initial increase on transition from the isotropic phase. Though the bend

elastic constant was seen to fall by a factor of almost 3, the sign of the constant was still positive and does not seem to go to zero or fall below it for the temperature range measured. The trend more or less agrees with other bimesogens exhibiting the N_{tb} phase. The value of $(e_1 - e_3)$ ranged from ~21 to 35 pC/m, and was observed to be nearly independent of temperature after an initial increase below the isotropic-nematic transition. The effective flexoelectric coefficients for CBC11CB were obtained to be much larger in comparison to conventional calamitics and almost twice higher for CBC11CB than that reported for another odd symmetric bimesogen. The flexoelectric polarization in the N phase was found to be almost 2.5 times higher than in rod-like molecules. Additionally, P_f was obtained to be much larger in the N_{tb} phase than in the nematic phase. This is possibly the source of electroclinic effect observed in this phase.

References

[1] C. T. Imrie and P. A. Henderson, *Chem. Soc. Rev.* **36**, 2096 (2007).

[2] K. L. Atkinson, S. M. Morris, F. Castles, M. M. Qasim, D. J. Gardiner, and H. J. Coles, *Phys. Rev. E.*, **85**, 012701 (2012).

[3] V. Borshch, Y-K Kim, J. Xiang, M. Gao, A. Jákli, V. P. Panov, J. K. Vij, C. T . Imrie, M.G. Tamba, G. H. Mehl and O. D. Lavrentovich, *Nature Communications*, **4**, 2365 DOI: 10.1038/ncomms3635 (2013).

[4] C. Meyer, G.R. Luckhurst and I. Dozov, *Phys. Rev. Lett.*, **111**, 067801 (2013).

[5] R.B. Meyer, in Molecular Fluids (ed. Balian, R., Weill, G.), Gordon and Breach, London, 271-343 (1976).

[6] I. Dozov, *Euro. Phys. Lett.*, **56**, 247 (2001).

[7] K. Adiem, M. Copic, G. R. Luckhurst, A. Mertelj, O. Parri, R. M. Richardson, B. D. Snow, B. A. Timimi, R. P. Tuffin and D. Wilkes, *Phys. Rev. E* , **88**, 022503 (2013).

[8] M. Cestari, S. Diez-Berart, D. A. Dunmur, A. Ferrarini, M. R. de la Fuente, D. J. B. Jackson, D. O. Lopez,G. R. Luckhurst, M. A. Perez-Jubindo, R. M. Richardson, J. Salud, B. A. Timimi, and H. Zimmermann, *Phys. Rev. E,* **84,** 031704 (2011).

[9] D. A. Dunmur, G. R. Luckhurst, M. R. de la Fuente, S. Diez, and M. A. Perez Jubindo, *J. Chem. Phys.*, **115**, 8681 (2011).

[10] P. Sathyanarayana, M.Mathew, Q. Li, V. S. S. Sastry, B. Kundu, K. V. Le, H. Takezoe, and S. Dhara, *Phys. Rev. E* , **81**: 010702 (2011).

[11] M. Cestari, E. Frezza, A. Ferrarini, and G. R. Luckhurst, *J. Mater. Chem.*, **21**, 12303 (2011).

[12] P. S. Salter, C. Tschierske, S. J. Elston, and E. P. Raynes, *Phys. Rev. E*, **84**, 031708 (2011).

[13] F. Castles, S. C. Green, D. J. Gardiner, S. M. Morris and H. J. Coles, *AIP Advances*, **2**, 022137 (2012).

[14] K. L. Atkinson, S. M. Morris, M. M. Qasim, F. Castles, D. J. Gardiner, P. J. W. Hands, S. Choi, W. Kim and H.J. Coles, *Phys. Chem. Chem. Phys.*, **14**, 16377 (2012).

[15] M. Cestari, E. Frezza, A. Ferrarini and G.R. Luckhurst, *J. Mater. Chem.*, **21**, 12303 (2011).

[16] L. M. Blinov, M. I. Barnik, M. Ozaki, N. M. Shtykov, and K.Yoshino, *Phys. Rev. E*, **62**, 8091 (2000).

[17] Yu. P. Panarin, O. E. Kalinovskaya, J. K. Vij and J. W. Goodby, *Phys. Rev. E*, **55**, 4345 (1997).

[18] N.M. Shtykov, M.I. Barnik, V.P. Panov, *JETP*, **91**, 126 (2000).

Chapter 5

Electro-Optical Investigations at the Nematic-N_{tb} Interface

In this chapter, the pre-transitional effects observed close to the N-N_{tb} phase transition is investigated through polarizing optical microscopy.

Contents

5.1 Introduction

The presence of a second nematic phase below the ordinary nematic phase in some odd bimesogenic liquid crystals composed of two rod-like mesogens was discussed briefly in Chapter 4. This phase has attracted significant attention because of a number of novel properties [1-4] exhibited by it in comparison to the higher temperature nematic phase. In earlier studies [1-2], this phase was referred to as N_x as the details of the molecular structure were unknown. However, most recent works [5, 6] provide rather clear evidence of the presence of a nano-scale structure similar to the ones predicted by R.B. Meyer [7] and I. Dozov [8].

Dozov [8] predicted the existence of two nematic phases, differing in their director distribution, in bent core systems. According to his studies, if the bend elastic constant becomes negative, then the director would no longer be aligned as in the conventional nematic phase but would become bent and produce spontaneous distortions. The bend deformation would not exist on its own but would require a stabilizing splay or twist deformation [8]. In the splay-bend nematic, the director always remains in one plane, but the local bend changes its sign periodically. The director in the twist-bend nematic however rotates around a cone, allowing the local bend to remain at its spontaneous value [8]. The twist-bend nematic differs from the conventional chiral nematic in that, the director follows an oblique helicoid, maintaining a constant oblique angle with the helix axis; whereas in N^* the director twists in space, drawing a right angled helicoid. Furthermore, for the twist-bend phase to be stable with respect to the splay-bend it is necessary for $K_{11}>2K_{22}$ [8].

The twist-bend nematic phase is of particular interest as its chirality appears spontaneously even though the constituent molecules are achiral. As a result of the

molecular achirality the phase may require to be composed of two chiral degenerate domains of opposite handedness. Though this model was initially proposed for bent-core systems, it may be reasonable to extend it to LC bimesogens with odd spacers due to an overall bent shape of the molecules, as mentioned previously in Chapter 4. Furthermore, recent investigations [5-6, 9] have also more or less confirmed that the second nematic phase occurring in these materials is indeed the N_{tb} phase.

In this chapter, the electro-optical studies performed close to the transition temperature of the ordinary nematics and the second nematic phase, now classified as N_{tb}, is discussed. Prior to introducing the studies performed at temperatures close to the N-N_{tb} transition, an overview of the striped patterns observed previously and the properties [1-4] exhibited by the N_{tb} phase is discussed in the next section.

5.2 An Overview of the Properties of the N_{tb} Phase

The twist bend or N_{tb} phase, occurring in bimesogens connected by an odd number of carbon atoms, is classified by the presence of spontaneous periodic patterns in a homogeneously aligned cell, in addition to the absence of the thermal fluctuations characteristic to the usual nematic [1]. The POM images obtained for one such bimesogenic material CBC11CB for cell thicknesses 7.7 and 13μm are presented in Fig. 5.1 (a, b, c) and 5.1 (d), respectively. At higher temperature (Fig. 5.1(a)) the conventional nematic phase is observed. Fig. 5.1(b) shows the uniform N_{tb} phase at the phase transition. The thermal fluctuations, characteristic of ordinary nematics, are invisible in the N_{tb} phase. On further cooling the sample, Fig. 5.1(c), the striped pattern appears, and gradually fills the entire area of the sample. The spontaneous appearance of self-deformation pattern in planar aligned cells was one of the first phenomena which

attracted attention to the N_{tb} phase. The periodicity of the pattern is defined by the cell geometry and in planar cells is found to be equal to double the cell gap [1]. In cells with thicknesses greater than ~8μm a focal-conic pattern is observed (Fig. 5.1(d)). The appearance of the striped and focal-conic patterns is likely to be determined by a delicate interplay among surface conditions, material constants, thermal and electric field history of the sample [10].

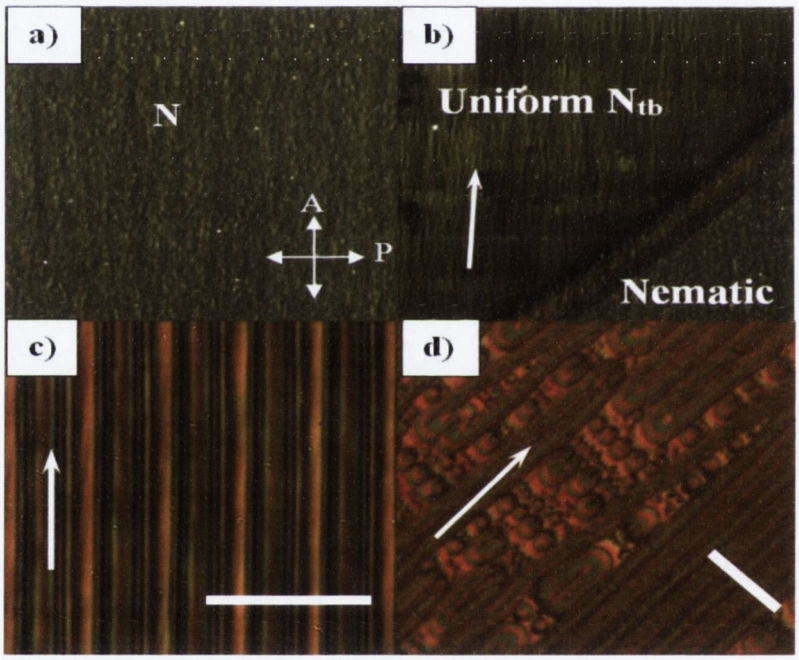

Figure 5.1: POM textures obtained in planar aligned cells filled with the material CBC11CB. In a 7.7μm cell on cooling from isotropic phase: a) the *N* phase, b) shows the *N*-N_{tb} transition, c) magnified image of the striped texture at lower temperatures in the N_{tb} phase, length of the white bar is 30 μm, (d) focal-conic domains in 13μm thick cell, white bar length is 55μm. White arrows represent the rubbing direction.

Apart from the spontaneous appearance of stripes, this phase also exhibits a microsecond linear response to an applied electric field in a manner similar to that observed in chiral materials [2]. The experimental studies were conducted on both pure dimers and their mixtures with 5CB [2]. For materials with positive $\Delta\varepsilon'$ the signal was seen to degrade rapidly, as the applied voltage caused transition to the homeotropic state. In materials with negative $\Delta\varepsilon'$ the fast and linear response was observed up to the breakdown voltages, with the switching time being of the order of 5 μs [10]. An example of this fast, linear optical response is shown in Fig. 5.2, for a 5 μm cell filled with an odd dimer material (M2 – chemical structure and phase transition temperature is provided in the Appendix), in the N_{tb} phase. A perfect linear response and switching time of the order of 4 μs was observed [2].

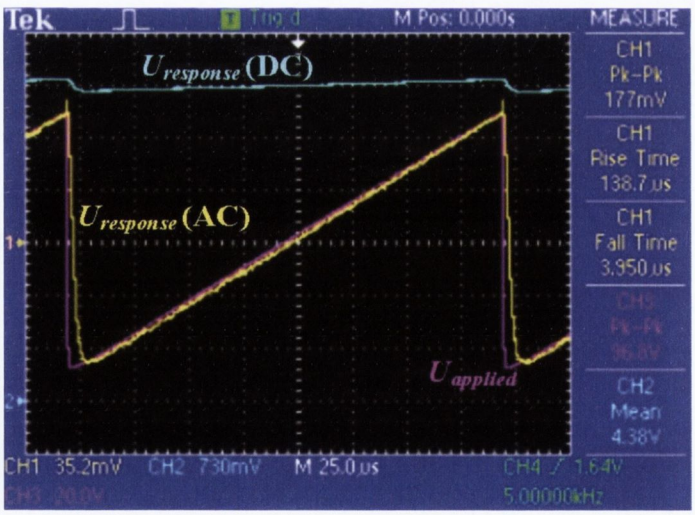

Figure 5.2: Oscillogram of the optical response in the N_{tb} phase of an odd bimesogen (M2), in a 5μm planar cell. $U_{applied}$ = 96.8 $V_{Pk\text{-}Pk}$ [2]. Here, channel 3 (pink) represents the applied voltage, channel 1 (yellow) is the optical response, magnified utilizing the AC input mode of the oscilloscope, and channel 2 (blue) is the same response signal acquired with DC mode. Image taken from [2].

The nature of the response closely resembles an electroclinic or ULH effect; both of which were originally attributed to chiral materials, while all the bimesogenic molecules used in the experiment were non-chiral. However, NMR studies [11, 12] show the presence of chirality in the N_{tb} phase. This was suggested to be a consequence of the odd-spacer linked molecules having, on average, a bent structure. The chirality of the phase then produces a small chiral biasing of the conformer distribution [12]. Recently, in an independent study conducted by two groups[5, 6], a 8 nm helical pitch was determined in the N_{tb} phase using freeze-fracture transmission electron microscopy (FFTEM); a technique which allows direct visualization of the microstructure of the LC phase.

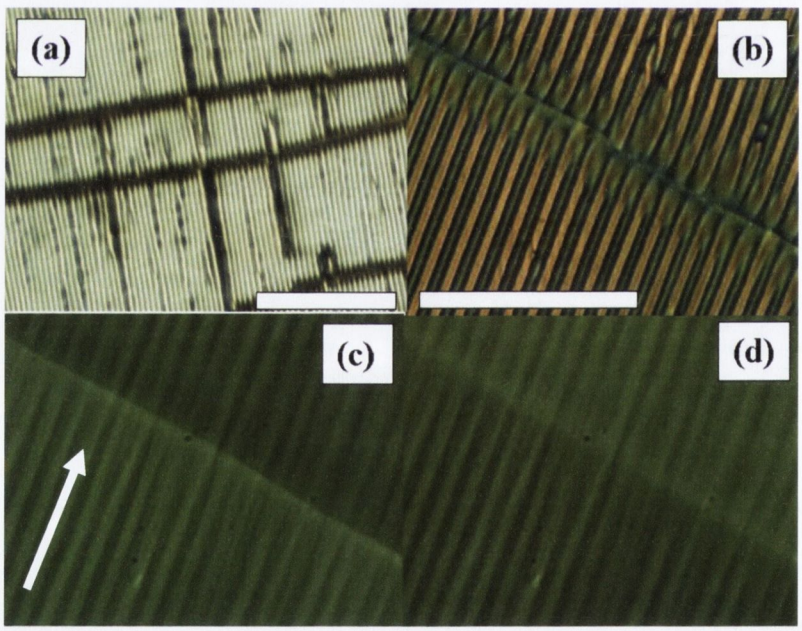

Figure 5.3: POM textures of an odd dimer in planar cells of 2 μm (a) and 5 μm (b,c,d). Domain boundary at 0 V (a,b); +200 V_{DC} (c), and -200 V_{DC} (d). White arrow represents the rubbing direction; bar length is 100 μm. Image taken from [2].

In addition to the polar switching, domains with opposite sign of switching in the N_{tb} phase [2] were observed, as demonstrated in Fig. 5.3. These domains are separated by a discontinuity in the striped pattern (Figs. 5.3 (a) and (b)). The domains remain stable in the N_{tb} phase; however, on heating the sample to the nematic phase these disappear, and re-appear randomly on cooling the sample back. While no visible difference was observed between the domains in the absence of an electric field, however on application of a DC electric field (Figs. 5.4 (c) and (d)) it was observed that the optical axis in neighbouring domains deviate from the rubbing axis in opposite directions; indicating that the optical axis exhibits two directions of deviation. This deviation of the optical axis from the rubbing direction is similar to the electroclinic effect or ULH switching [2]. For small applied fields the domain configuration was rather random and was determined by the surface irregularities and the thermal history of the sample [2, 10]. In some cells a mono-domain area could be observed as large as the microscope field of view, i.e. a few millimeters in diameter [4].

Further investigation revealed that application of high alternating current (AC) electric fields and high frequencies produced periodic striped domains in the N_{tb} phase [4], as shown in Fig. 5.4. This pattern was obtained by applying an AC electric field of ~16 V/μm at frequency of 5 kHz, at temperature ~ 0.5°C below the N-N_{tb} phase transition. The image was captured with a DC field of the same amplitude applied. This is a completely different striped pattern from the one observed in planar cells at lower temperatures in the N_{tb} phase without electric field. In Fig. 5.4, a periodic striped pattern formed by the domains of opposite switching can easily be seen. When the parameters of the applied field were changed gradually, the periodicity of the domains were observed to change via "sliding in" or "sliding out" of a domain along the domain boundaries as marked in Fig 5.4 by circles [4].

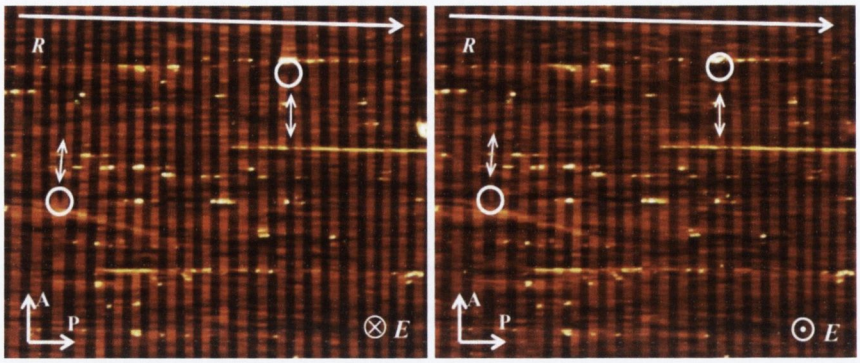

Figure 5.4: POM image of a 5 μm EHC cell, E = 16 V/μm, frequency 5 kHz. The domain boundaries are perpendicular to the alignment direction (R). Darker areas: the optical axis deviated from the rubbing direction towards the polarizer axis (P), and is almost parallel to it. Brighter areas: the optical axis deviates in opposite direction and forms a larger angle (a few degrees) with the polarizer axis. Right and left images differ in the sign of the applied DC field. Image taken from [4].

The opposite switching in the adjacent domains hence suggests the presence of opposite chiral handedness. Further investigations revealed that the periodicity of the domains ranged from ~2 to 12μm, depending on the frequency and the amplitude of the applied voltage for a 4 μm planar cell, enabling controlled production of periodic structures [4].

Recently Meyer et al. [9] extended the twist-bend nematic model to describe the electro-optics of this phase. They predicted that an electroclinic effect of flexoelectric origin, analogous to the ULH effect observed in chiral nematics, should exist in the N_{tb} phase. They also mentioned that the electro-optical effect in this phase, first observed by Panov et al. [2], could be a result of the electroclinic effect.

In materials exhibiting positive $\Delta\varepsilon'$, a considerable hysteresis is seen in homogeneous cells when the N_{tb} sample is subjected to *Freedericksz* transition; the

hysteresis is seen to increase rapidly on cooling the sample. Figure 5.5 demonstrates the difference between the transmittance-curve exhibited by ordinary nematic and twist-bend nematic at temperatures 69.5°C and 68.5°C, respectively, of the odd dimer mixture (CBC9CB + 30 % 5CB) in a 2.4 μm planar cell when subject to an electric field (~4V/μm).

The *Freederickz* transition phenomenon in the N_{tb} phase takes much longer time, nearly tens of seconds, in comparison to the nematic phase (few milliseconds) indicating that the phase is quite viscous. The coexistence of such a dramatic viscosity increase together with the appearance of the microsecond response in the N_{tb} phase is extremely intriguing.

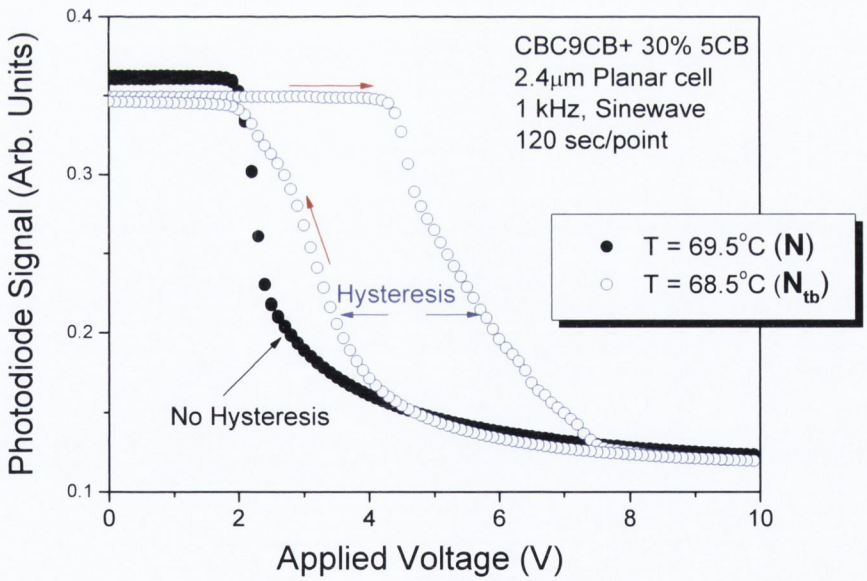

Figure 5.5: *Freedericksz* transition in a 2.4 μm planar cell filled with an odd dimer mixture (CBC9CB + 30% 5CB) having positive dielectric anisotropy. The ordinary nematic phase exhibits conventional behaviour, while considerable hysteresis is observed in the N_{tb} phase.

In addition to the spontaneous striped patterns observed in planar cells: spontaneous deformation patterns – Stripe-1, and the field induced patterns – Stripe-2, we discovered a new set of stripes very close the N-N_{tb} transition. In this chapter we present the results of the electro-optical experiments performed at the boundary of the N-N_{tb} phase. The condition for the appearance of the new striped pattern is studied for various cell gaps and concentrations of the sample.

5.3 Materials under Study

The bimesogens CBC7CB and CBC9CB and their mixtures with 5CB were used to investigate the pre-transitional effects. The chemical structure of the compounds investigated in this chapter is given in Fig. 5.6 and the transition temperatures are given in the figure caption. The pure bimesogens together with the mixtures containing 20 and 30% by wt. of 5CB were synthesized by Dr. Mehl's group in Hull; while the mixtures with concentrations of 34 and 42% 5CB were prepared in Dublin. The lower temperature twist-nematic phase existed in all the mixtures composed of varying concentrations of 5CB. The existence of N_{tb} phase in the mixtures with 5CB allows the phase to extend to a wide temperature range including room temperature. All the materials studied in this chapter have positive $\Delta\varepsilon'$. The phases in the mixture were found to be relatively stable, and no phase separation was seen to occur during the experiments. POM studies in homogenous cells confirmed that N_{tb} phase occurs in all the dimer mixtures studied.

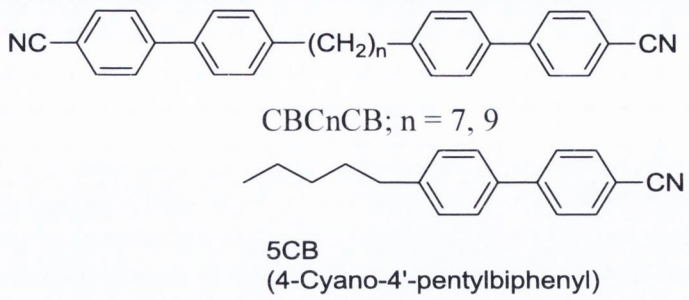

Figure 5.6: Chemical formula of liquid crystalline materials studied. Mixtures of CBC7CB and CBC9CB with 5CB were prepared for up to 42 % by wt. of the monomer, in order to investigate the pre-transitional effects. All mixtures with 5CB exhibit both the ordinary nematic phase and the lower temperature twist-bend nematic phase. No phase separation was found to occur during the experiments.

% 5CB	0	20	30	34	42
CBC7CB	N_{tb} 103N 116 I	N_{tb} 72 N 92 I	N_{tb} 53 N 80 I	N_{tb} 51 N 75 I	N_{tb} 42 N 65 I
CBC9CB	N_{tb} 109 N 124 I	N_{tb} 78 N 102 I	N_{tb} 65 N 93 I	N_{tb} 56 N 83 I	N_{tb} 45 N 74 I

Table 5.1: Transition temperatures in Degree Celsius for the pure bimesogens and their mixtures with 5CB.

5.4 Experimental Technique

In order to study the pre-transitional phenomenon, homemade cells of thickness varying from 5-8 μm, and commercial planar cells of thicknesses 5, 15 and 25 μm were used. The electro-optical set-up described in Section 2.3 was used to carry out detailed investigations of the bimesogenic samples.

5.5 Results and Discussion

POM studies performed by us in cells of thicknesses greater than 8μm and certain concentrations of 5CB in the dimer mixture, revealed the appearance of fine stripes very close to the N-N_{tb} transition. These stripes are often accompanied by the appearance of 'rainbow- colours' and appear spontaneously at a narrow temperature range close to the transition region. These patterns are positioned perpendicular to the rubbing direction, hence making them quite distinct from Stripe-1, observed at lower temperatures in the N_{tb} phase.

Figure 5.7 shows the textures obtained using a polarizing microscope in a 25 μm planar cell filled with the material (CBC7CB + 30% 5CB), for temperatures close to the N-N_{tb} transition. The region with the stripes along with the 'rainbow-colours' is easily distinguishable from those of the other two nematic phases. This region is also seen to have fluctuations similar to those observed in the nematic phase. The periodicity of the striped pattern in this particular sample is obtained to be 2.94 μm, which is much lower than the cell thickness.

When an electric field (10V, 10 kHz, square-wave) is applied across this region, [see Figure 5.7 (b)], the stripes tend to lose their uniformity and become wider. However they look very different from those in N or N_{tb} phase. It is seen that the nematic phase almost switches to the homeotropic state at this field, as the material has positive dielectric anisotropy, while N_{tb} phase remains planar.

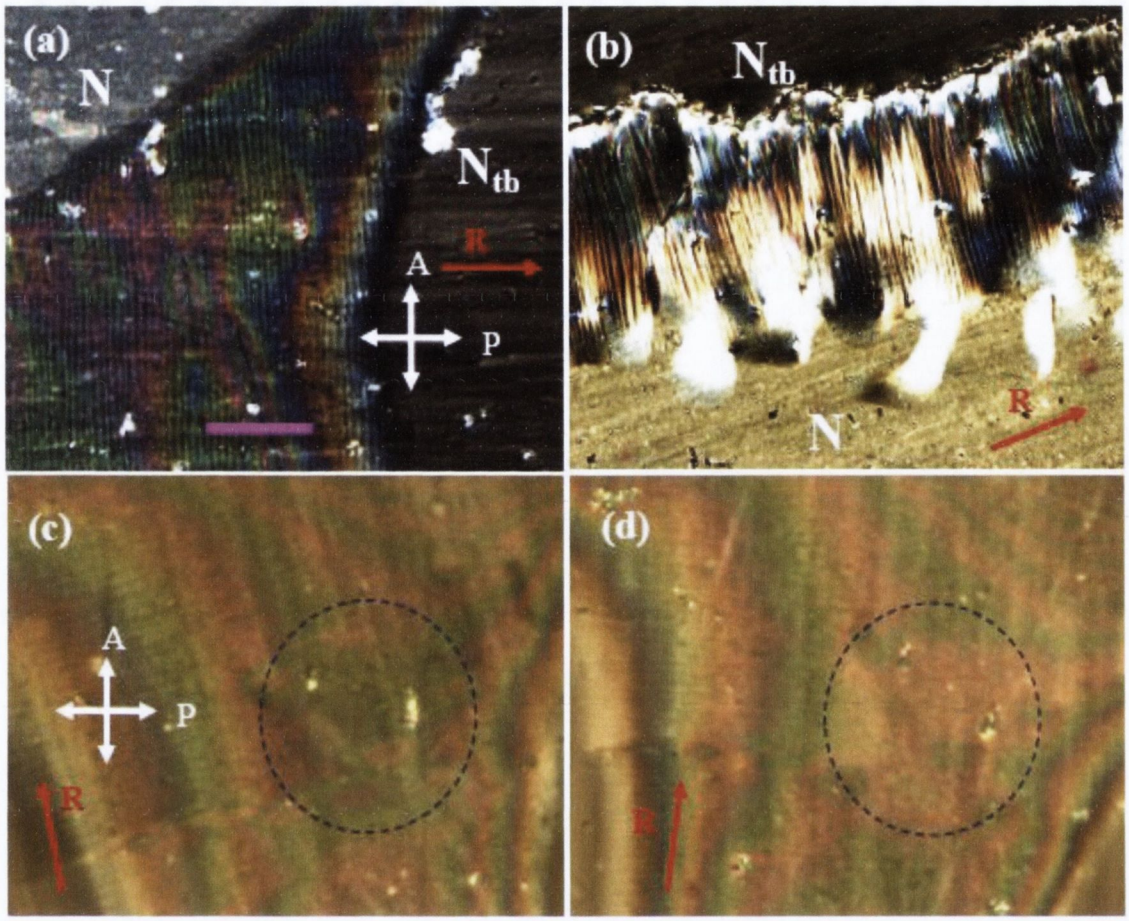

Figure 5.7: POM textures obtained in a 25μm cell filled with the sample (CBC7CB + 30% 5CB) when viewed under cross-polarizers on slowly cooling the cell from the nematic phase. (a) the observed striped region between the *N* and N_{tb} phase for a 10X lens magnification observed at temperature 52.75°C (length of the magenta bar is 24 μm). The stripes are uniform and have a periodicity of 2.94 μm. The red arrows depicts the rubbing direction; (b) the effect of an electric field (10 V with frequency of 10 kHz at temperature: of 52.82°C) applied across the cell in this narrow temperature range. In (c) and (d) colours obtained are compared when the rubbing direction is rotated left (c) and right (d) from the axis of the crossed polarizers. The circle diameter is 80μm.

When the rubbing direction is rotated slightly from the axis of the crossed polarizer to the left (Fig. 5.7(c)) and right (Fig. 5.7(d)), the colours of the texture obtained seem to be interchanged. For ease of observance this is demonstrated by the area enclosed by the blue-dashed circle. This complimentary exchange of colours between the textures is indicative of a certain extent of spontaneous chirality in the system.

The periodicity of the new stripes varies as a function of both concentration and the cell gap. In the pure materials, the stripes are not readily visible but as the concentration of 5CB is increased these are more detectable. However, beyond a certain concentration of 5CB ($\geq$ 34%), the stripes disappear completely in some of the samples. This effect is not seen under fast heating or cooling, and is observed in cells with thicknesses > 8 μm, which indicates that this effect is not caused by the cell surfaces. The periodicity of the stripes together with a temperature range of the rainbow colours for various cell thicknesses and concentrations have been studied for both sets of dimers CBC7CB and CBC9CB, and their mixtures with 5CB. The results are summarized in Table 5.2. For the mixtures, at a fixed concentration of 5CB, the periodicity of the pattern is seen to increase slightly as the cell gap is increased. For example, in the CBC7CB + 20% 5CB mixture, the periodicity increases from 1.93 to 2.2 μm as the cell thickness is increased from 15 to 25μm. Similarly, for a fixed cell gap, the periodicity is seen to increase as the concentration of 5CB is increased. The cell gap and concentration dependence of these striped patterns is particularly intriguing. However the theoretical reasoning pertaining to the trend exhibited by the stripes needs more detailed investigations, and is thus, beyond the scope of this thesis.

The temperature range associated with the 'rainbow-colours' is estimated to be less than 0.1 ^{o}C, and appears primarily to be a function of the temperature gradient in the particular experiment, the cell gap and to a certain extent the concentration of 5CB

in the mixture. When a second heater was introduced on the top of the sample, the temperature range of the 'rainbow colours' was found to decrease significantly, and in some cases vanished altogether, making evident its relevance to the temperature gradient across the cell. The periodicity of the striped pattern, however, remains unaffected, suggesting that the rainbow colours are related to the temperature gradient, while the stripes are independent of it. (Note Table 5.2 summarizes the temperature ranges for the bimesogenic mixtures in the absence of the second heater.)

% of 5CB		0%	20%	30%	34%	42%
CBC7CB 15μm		0.08°C no	0.03°C **1.93** μm	0.06°C 2.74 μm	0.06°C no	0.03°C no
CBC7CB 25μm		0.16°C no	0.08°C **2.20** μm	0.25°C 2.94 μm	0.12°C no	0.06°C no
CBC9CB 15μm		0.08°C no	0.1°C **2.94** μm	0.08°C no	0.03°C no	0.0°C no
CBC9CB 25μm		0.1°C no	0.2°C **3.27** μm	0.13°C no	0.08°C no	0.04°C no

Table 5.2: The periodicity of the striped patterns (**bold**) and the temperature ranges associated with rainbow-like colours for the various mixtures and cell gaps.

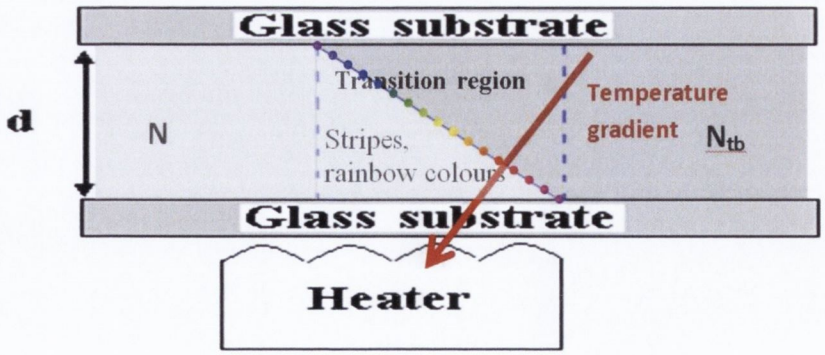

Figure 5.8: The temperature gradient in a heating stage causes the interface between N_{tb} and nematic phases to form wedge-like confinement for each phase.

To explain the observed phenomenon, we refer to the geometry shown in Fig 5.8. The temperature gradient in the heating stage can cause the interface between the nematic and twist-bend nematic to form a wedge like confinement. The 'rainbow colours' and their behaviour as a function of the cell cap can then be explained by the interference on the wedge made with the materials with different birefringence and refractive indices (i.e. N and N_{tb} phases). However, the interchange of the colours on rotating the sample between the crossed polarizers (Figure 5.7 (c, d)) implies that not only birefringence, but some optical rotation is also involved. This indicates some degree of self-deformation and spontaneous chirality in the system. The fluctuations seen in the transition region appear to originate from a thin layer of the nematic phase present at the bottom (warmer) glass substrate, while the N_{tb} phase is present closer to the top substrate (colder surface), see Fig. 5.8. The periodic pattern can be attributed to the interface between the two phases; the electric field switches the ordinary nematic phase by *Freedericksz* transition, whereas it causes the stripes to become non-uniform and wider, as seen in Fig. 5.7 (b). It is likely that the presence of a thin film of aligned nematic phase improves the visibility of an intrinsic pattern of the N_{tb} phase.

It is also noted that the observed phenomenon does not arise from the Grandjean texture, likely to be seen on confining a material with a short helical pitch in wedge geometry. In our case the stripes appear normal to the rubbing direction and these are independent of the magnitude and direction of the temperature gradient (visualized by the rainbow-colors), i.e. these are not caused by the wedge shape (Fig. 4.9) of the N_{tb} (or N) sections of the sample.

These new stripes, which appear normal to the rubbing direction, are reminiscent of the patterns predicted by Dozov [8] for the twist-bend nematic phase. The values and sign of the elastic constants, especially bend, was anticipated to have a significant role

in the formation of the N_{tb} phase [8]. Hence, it is quite likely that a change in the elastic constant values very close to the N-N_{tb} phase transition may have a key role to play in the emergence of the new stripes. Large flexoelectric polarization also appears to be a plausible explanation of the observance of the new stripes close to the N_{tb} phase, as recent studies by Meyer et al. [9] suggests the twist-bend phase to have a spontaneous flexoelectric polarization due to the conical helix structure of the N_{tb}. An electroclinic effect of flexoelectric origin was also demonstrated in this phase [9]. Additionally, our experimental findings for the bimesogen CBC11CB, presented in Chapter 4, revealed that P_f increases steadily close to the N-N_{tb} phase transition and is ~ 2.5 times higher in N_{tb} than in the N phase.

5.6 Conclusions

In a narrow temperature range close to the N-N_{tb} phase transition, a new type of striped pattern is observed under a polarising microscope, in bimesogens CBC7CB and CBC9CB and their mixtures with the monomer (5CB) in a temperature gradient cell, indicating yet another mysterious chiral self-assembly phenomenon observed in this class of materials. These micrometer scale stripes are accompanied by the appearance of rainbow colours, and are present only in a narrow temperature range close to the N-N_{tb} phase transition temperature. This effect is not seen under fast heating or cooling and observed in cells with a thickness > 8 μm, which indicates that this effect is not caused by the cell surfaces. The appearance of 'rainbow colours' is found to be related to the temperature gradient, while the stripes are independent of it.

References

[1] V.P. Panov, M. Nagaraj , J.K. Vij , Y.P. Panarin, A. Kohlmeier, M.G. Tamba, R.A. Lewis and G.H. Mehl, *Phys. Rev. Lett.*, **105** 167801 (2010).

[2] V.P. Panov, R. Balachandran, M. Nagaraj, J.K. Vij, M.G. Tamba, A. Kohlmeier, and G.H. Mehl, *Appl. Phys. Lett.*, **99**, 261903 (2011).

[3] M. Cestari, S. Diez-Berart, D. A. Dunmur, A. Ferrarini, M. R.de la Fuente, D. J. B. Jackson, D. O. Lopez, G. R. Luckhurst, M. A. Perez-Jubindo, R. M. Richardson, J. Salud, B. A. Timimi and H. Zimmermann, *Phys. Rev. E*, **84**, 031704 (2011).

[4] V.P. Panov, R. Balachandran, J.K.Vij , M.G. Tamba, A. Kohlmeier, and G.H. Mehl, *Appl. Phys. Lett.*, **101**, 234106 (2012).

[5] V. Borshch, Y.-K. Kim, J. Xiang, M. Gao, A. Jákli, V. P. Panov, J. K. Vij, C. T . Imrie, M.G. Tamba, G. H. Mehl and O. D. Lavrentovich, *Nature Communications,* **4**, 2635 DOI: 10.1038/ncomms3635 (2013).

[6] D. Chen, J. H. Porada, J. B. Hooper, A. Klittnick, Y. Shen, M. R.Tuchband, E. Korblova, D Bedrov, D. M. Walba, M. A. Glaser,J. E. Maclennan, and N. A. Clark, *PNAS,* **110**, 15931 (2013).

[7] R.B. Meyer, in *Molecular Fluids* (ed. Balian, R., Weill, G.), Gordon and Breach, London, 271-343 (1976).

[8] I. Dozov, *Euro. Phys. Lett.,* **56**, 247 (2001).

[9] C. Meyer, G.R. Luckhurst and I. Dozov, *Phys. Rev. Lett.*, **111**, 067801 (2013).

[10] V. P. Panov, J. K. Vij, R. Balachandaran, V. Borshch, O. D. Lavrentovich, M. G. Tamba, and G. H. Mehl, *Proc. SPIE, Liquid Crystals*, XV11 **8828**, 88280X (2013).

[11] J.W. Emsley, P. Lesot, G.R. Luckhurst, A. Meddour, D. Merlet, *Phys. Rev. E.*, **87**, 040501 (2013).

[12] J.W. Emsley, M. Lelli, A. Lesage, G.R. Luckhurst, *J. Phys. Chem. B*, **117**, 6547 (2013).

Chapter 6

Dielectric and Electro-optical Studies of a Dimesogen

In this chapter, the properties of a dimesogen composed of a bent-core and rod-like mesogen are investigated through dielectric and electro-optical techniques.

Contents

6.1 Introduction

Connecting two bent-core mesogens or calamitic units with a flexible spacer has given rise to many novel and complex phase sequences, which in turn exhibit very interesting properties. Dantlgraber et al. [1] reported the first example of a dimesogen combining two bent-core molecules linked by dimethylsiloxane units. Various ferroelectric and anti-ferroelectric polar Sm*C* phases were observed in some of these compounds depending on the spacer length. It is also possible to combine a bent-core molecule and a rod-like mesogen to form a dimesogen. A number of studies have been performed on the terminal combinations of such dimesogens [2-5]. Some of these dimesogens were reported to have unusual liquid crystalline properties by Tamba et al. [2], with the mesophase behaviour being strongly dependent on the size and structure of the calamitic unit as well as the length and parity of the spacer.

There has been a continued interest in the dielectric studies of the nematic phase formed by dimesogens as the dielectric properties are sensitive to both the dipole moment and the ordering of molecules. The dielectric anisotropy $\Delta\varepsilon'$ is one of the important parameters of a LC material that needs to be determined for designing LC based devices as it plays an important role in the governing the electric field effects on such systems. Depending on the sign of $\Delta\varepsilon'$ and the cell-configuration, the director can be realigned by the electric field. The reorientation of the director via *Freedericksz* transition causes the optical properties of the sample to change – this phenomenon is exploited in many commercial LC applications. The sign of $\Delta\varepsilon'$ can be positive or negative, and may even change sign at some frequency. Such a change in the sign of $\Delta\varepsilon'$ as a function of frequency has been reported for many calamitics [6] and BC [7, 8]

systems, and these nematics are often labelled as dual frequency nematic (DFN) LCs. In conventional DFNs, $\Delta\varepsilon'$ is positive at lower frequencies and negative at higher frequencies, and the frequency at which the sign reversal occurs is called the crossover frequency f_c. DFNs are of particular interest as the sign reversal of $\Delta\varepsilon'$ provides a vast improvement in the switching on and off response of the LCs in comparison to the conventional nematics [9], achieved by simply varying the frequency of the driving signal. In most calamitics the frequency at which sign reversal of $\Delta\varepsilon'$ occurs is too high for applications, whereas in BCNs [7, 8] this occurs at much lower frequencies.

In this chapter, we investigate the dielectric and electro-optical properties of a dimesogen, BR1 composed of a bent-core and calamitic mesogen, linked laterally via a flexible spacer [10]. We find that the material exhibits DFN mode at much lower frequencies compared to conventional rod-like materials and BCNs.

6.1.1 Theoretical Background

The electric permittivity of a material determines the polarization induced in the material by an electric field, as discussed in Chapter 1. If the applied frequency varies with time, then the frequency dependence of the permittivity is an additional property of the material [11]. As with any time-dependent response, the measured permittivity may not be in phase with the applied field. In order to describe the frequency dependent dielectric response of a material, the amplitude and phase of the induced polarization must be determined. A convenient way of describing the phase and amplitude is through complex notation: $\varepsilon^* = \varepsilon'(\omega) - i\varepsilon''(\omega)$, so that ε' (real-part) measures the in-phase response and ε'' (imaginary part) measures the 90^o out-of-phase response [11].

For uniaxial LCs in the absence of measurable local biaxiality, the frequency dependent dielectric permittivity can be analyzed in terms of the Maier and Meier (M-M) model [11].The strengths of the relaxations associated with the different processes can be related to the dipole components using the M-M model:

$$\varepsilon'_{||} - n_{||}^{\,2} = \frac{NhF^2 g_{||}}{3\varepsilon_0 k_B T}\left[\mu_l^{\,2}(1+2S) + \mu_t^{\,2}(1-S)\right], \qquad (6.1)$$

$$\varepsilon'_{\perp} - n_{\perp}^{\,2} = \frac{NhF^2 g_{\perp}}{3\varepsilon_0 k_B T}\left[\mu_l^{\,2}(1-S) + \mu_t^{\,2}(1+\tfrac{1}{2}S)\right], \qquad (6.2)$$

$$\langle\varepsilon'\rangle - n^2 = \frac{NhF^2}{\varepsilon_0}\left(\frac{g_N \mu^2}{3k_B T}\right). \qquad (6.3)$$

Here S is the order parameter, $\mu_l = \mu\cos\beta$ and $\mu_t = \mu\sin\beta$ are the longitudinal and transverse components of the molecular dipole moment μ; β is the angle made by the dipole moment with respect to the director **n**. $n_{||}$ and $n_{\perp}$ are the parallel and perpendicular refractive indices respectively. $A = \dfrac{NhF^2}{3\varepsilon_0 k_B}$ is the multiplying/scaling factor for each dipolar contribution to the dielectric relaxation strength. N is the number density, T is the absolute temperature, ε_o is the permittivity of vacuum, F and h are the internal field factors for the reaction and cavity field, and $g_{||}$ and $g_{\perp}$ are the anisotropic Kirkwood correlation factors defined for the director parallel and perpendicular to the electric field respectively. k_BT is the thermal energy; with k_B being the Boltzmann constant and g_N is the net dipole correlation factor. While the quantitative behaviour of

the permittivity can be explained in terms of these equations, they do not provide a quantitative analysis of the dielectric data.

For isotropic fluids, the Kirkwood correlation factor can be interpreted as the ensemble average of the cosine of the angle (θ_{pair}) between the dipole moment vectors of the interacting pair of molecules:

$$g_{iso} = 1 + \left\langle \cos\theta_{pair} \right\rangle . \tag{6.4}$$

Therefore in the case of constant g_N, the average permittivity, $\left\langle \varepsilon' \right\rangle \left(= \frac{\varepsilon'_{\parallel} + 2\varepsilon'_{\perp}}{3} \right)$, expressed in Eqn. (6.3) should vary in a continuous manner on decreasing temperature from the isotropic to the nematic phase. However, for many liquid crystals, especially those containing strongly polar molecules, the temperature dependence of the dielectric behaviour often varies from that predicted by the above equations, where there is either an increment or decrease in the value of the mean permittivity at the isotropic to nematic transition due to local dipole-dipole correlations. The net dipole correlation factor (g_N) in the nematic phase is a function of S and is expressed as [12]:

$$g_N = \frac{g_{\parallel}}{3\mu^2}\left[\mu_l^2(2S+1) + \mu_t^2(1-S)\right] + \frac{2g_{\perp}}{3\mu^2}\left[\mu_l^2(1-S) + \mu_t^2(1+\frac{1}{2}S)\right] . \tag{6.5}$$

The short range correlations between the dipolar molecules can be described in terms of the anisotropic Kirkwood g-factors defined for different directions in the sample. These are defined in terms of the appropriate dipole correlation functions as [11]:

$$g_i = 1 + V^{-1}\int G_i(\mathbf{r})d\mathbf{r} , \tag{6.6}$$

$$G_i(\mathbf{r}) = \frac{\langle \mu_i(0)\mu_i(\mathbf{r}) \rangle}{\langle \mu_i(0)\mu_i(0) \rangle}, \tag{6.7}$$

where *i* refers to the parallel and perpendicular directions. Thus, $g_{\parallel}$ and $g_{\perp}$ measure the extent to which the projections of the molecular dipole moments are correlated along the principal axis of an anisotropic fluid, assumed to be uniaxial in this case. Dielectric studies of many LC samples indicate that the dipole-dipole associations play an important role in the determining the dielectric properties of the material in the nematic and isotropic phases [13]. For materials exhibiting anti-parallel correlation with the longitudinal dipoles, $g_{\parallel} < 1$. For parallel correlation with transverse dipoles, $g_{\perp} > 1$. With increasing temperature the g-factors go to unity, although antiparallel correlations can persist in the isotropic phase as well [13].

The dielectric anisotropy $\Delta\varepsilon'$ $(=\varepsilon'_{||} - \varepsilon'_{\perp})$ can be obtained from Eqns (6.1) and (6.2) and is given by [11]:

$$\Delta\varepsilon' = \frac{NFH}{\varepsilon_0}[\Delta\alpha - \frac{\mu^2(1-3\cos^2\beta)}{2kT}]S \ . \tag{6.8}$$

Here $\Delta\alpha$ $(\propto n_{\parallel}^2 - n_{\perp}^2)$ is the anisotropy in polarizability and β is the angle between the long molecular axis and the dipole moment. It follows from Eqn. (6.8) that $\Delta\varepsilon'$ roughly follows the order parameter if β is constant and short range correlations are weak. Thus, if the dipole moment is predominantly perpendicular to the alignment axis, then $\Delta\varepsilon'$ is negative.

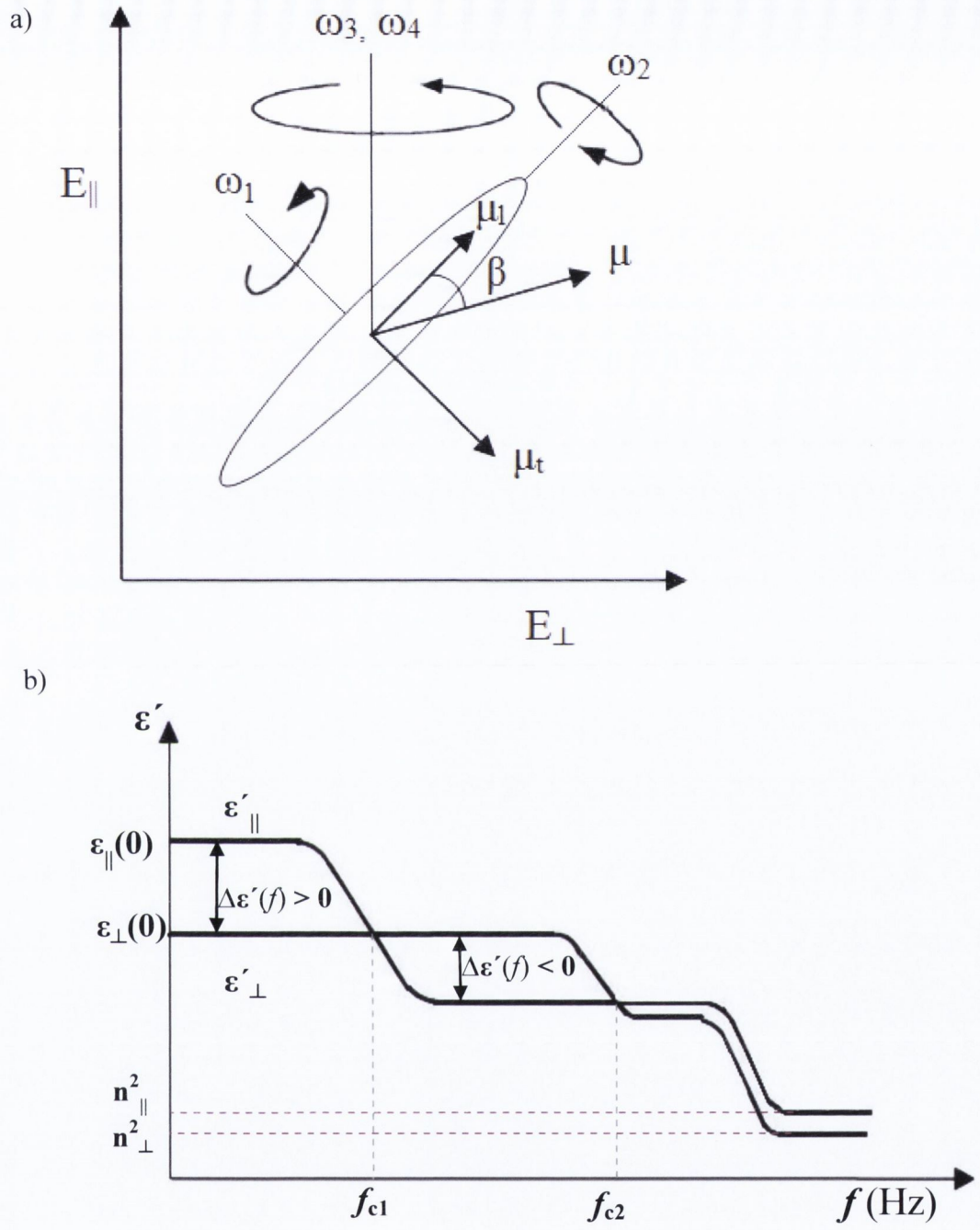

Figure 6.1: (a) Illustration of the molecular rotational modes that contributes to the dielectric relaxation. (b) Representation of the frequency variation of $\varepsilon'(\omega)$ of a uniaxial nematic.

For the nematic phase, each component of ε' given in eqn. (6.1) and (6.2) contains two contributions from the molecular dipole moment, and these are expected to show at least two relaxation processes due to the different dependency of a component of the dipole moment to the two permittivities. Figure [6.1(a)] shows the possible rotational modes for the general case of a molecule with a permanent dipole moment which makes an angle β with the molecular long-axis. The parallel and perpendicular axes represent the direction of the electric field with respect to the director **n**. The molecular dynamics can be approximately described by four rotational modes as shown in Fig. 6.1(a): (a) the end-over-end rotation ω_1, (b) the precessional motion of the long molecular axis around the director of the phase ω_3 and the combination of precessional motion and rotational motion around the long molecular axis ω_4, and (c) the rotation about its own long molecular axis ω_2. Assuming that molecules are rigid and intermolecular relaxations are forbidden, only a single dipole moment contributes to the dielectric permittivity. However, in cases where a number of dipolar groups are present and these are not connected rigidly to each other, then they may make separate contributions to the dielectric permittivity.

The temperature dependency of the dielectric relaxation strength for each component is primarily determined by the temperature variation of the order parameter, S [see Eqns. (6.1) and (6.2)]. More information can be obtained about the nature of the rotational dynamics in LCs by employing suitable microscopic models. Nordio et al.[14] developed a general theory for the dielectric relaxation of rigid dipolar moments in nematic fluids, wherein the frequency dependent components of the complex permittivity can be related to the Laplace transform of the time auto-correlations

functions for projections of the molecular dipole moment parallel and perpendicular to the director:

$$\langle \mu_{\parallel}(0)\mu_{\parallel}(t)\rangle = \frac{1}{3}[\mu_l^2(1+2S)\Phi_{00}(t) + \mu_t^2(1-S)\Phi_{01}(t)], \tag{6.9}$$

$$\langle \mu_{\perp}(0)\mu_{\perp}(t)\rangle = \frac{1}{3}[\mu_l^2(1-S)\Phi_{10}(t) + \mu_t^2(1+\frac{1}{2}S)\Phi_{11}(t)], \tag{6.10}$$

where μ_l and μ_t are the longitudinal and transverse components of the molecular dipole, and Φ_{mn} are time correlation functions of the first order Wigner rotation matrix. The subscripts m and n are the indices of the Wigner function. The time correlation functions can be described by the characteristic relaxation times τ_{mn} of each component, and a relation can approximately be established between these times and the four rotational modes, such that $\omega_1 \sim\tau_{00}^{-1}$, $\omega_2 \sim\tau_{01}^{-1}$, $\omega_3 \sim\tau_{10}^{-1}$ and $\omega_4 \sim\tau_{11}^{-1}$, where $\tau_{00}, \tau_{01}, \tau_{10}$ and τ_{11} are the corresponding relaxation times [12].

Figure 6.1 (b) shows a schematic representation of the real part of permittivity as a function of frequency. The sign of $\Delta\varepsilon'$ is dependent on the applied frequency, as demonstrated in the figure 6.1(b) as an example. In this particular example, the sign of dielectric anisotropy changes from $\Delta\varepsilon' > 0$ at $f < f_{c1}$ to $\Delta\varepsilon' < 0$ at $f > f_{c1}$ as a function of the frequency of the applied field f. The frequencies f_{c1} and f_{c2} are referred to as the crossover frequencies, and correspond to the frequency at which $\Delta\varepsilon'$ changes sign. The frequency dependence of the sign of the dielectric anisotropy can be used to align the liquid crystal directors parallel or perpendicular to the direction of the applied electric field by simply varying the frequency of the driving signal. Such nematics are often referred to as dual frequency nematics (DFNs).

6.2 Material under Investigation and XRD Results

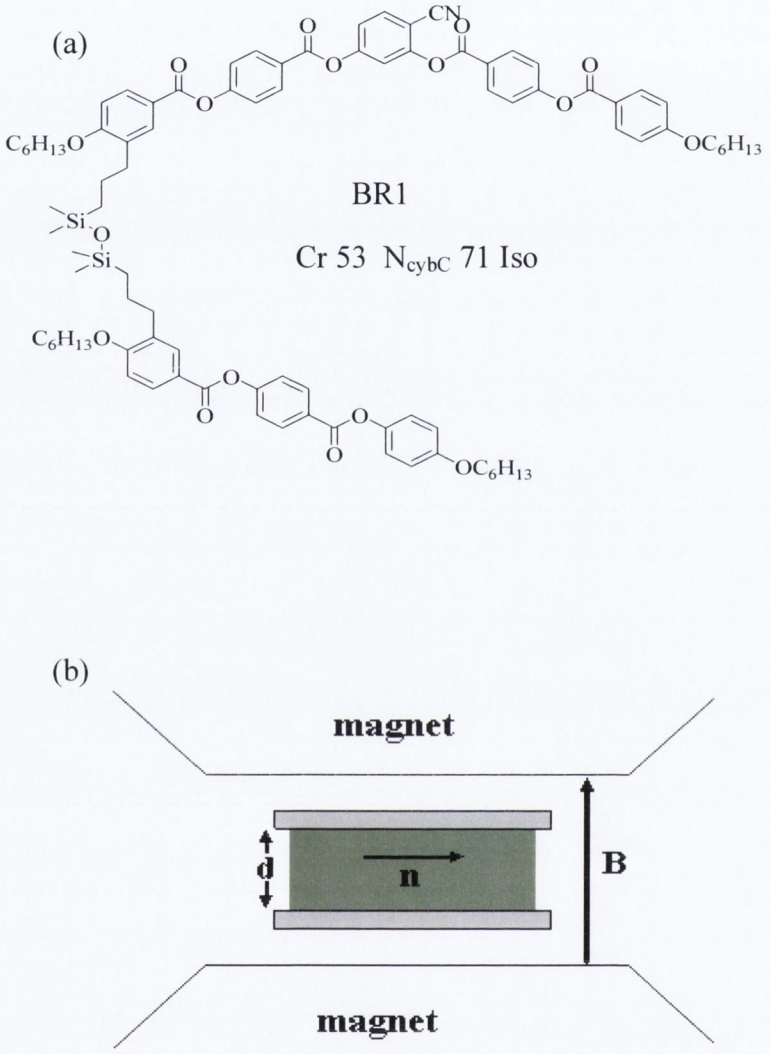

Figure 6.2: (a) Chemical structure and the transition temperature of the dimesogenic material under study, BR1. (b) shows the sample geometry used in the measurements of the parallel component of permittivity, obtained by inducing a homeotropic alignment on application of a magnetic field (**B**) in a direction perpendicular to the director (**n**) of the originally planar aligned cell.

The compound studied in this chapter, BR1 [10] is composed of a bent-core unit and calamitic mesogen linked laterally by a flexible spacer. The material was synthesized by Dr. Cartsen's group in Germany. The molecular structure and the phase transition temperatures of the material are given in Fig. 6.2 (a). The material exhibits nematic phase on cooling from the isotropic phase. XRD results [10] revealed that Smectic-*C* like clusters are present in the entire nematic phase of this compound, with the cluster size being of the order of the thickness of a single layer. Furthermore, the splitting of the small angle scattering $\Delta\chi/2$ is ~ 50° indicating a significant tilt of the molecules in the Sm*C* like clusters. Additionally, no macroscopic biaxiality was observed in the nematic phase of BR1, when investigated using the polarized IR technique [10].

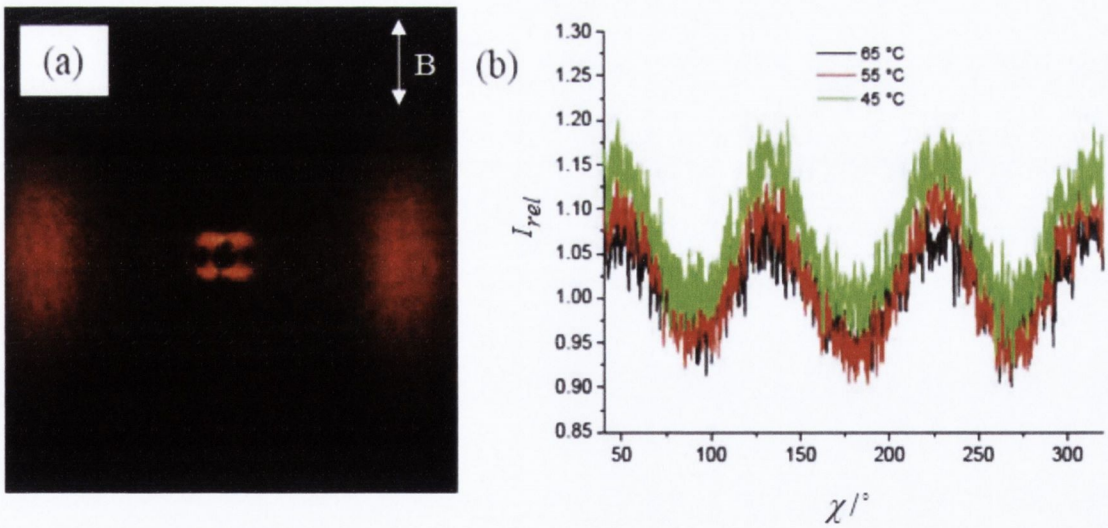

Figure 6.3: X-ray diffraction patterns of an oriented samples of compound **BR1** under a magnetic field: (a) N_{cybC} phase at 45°C (shows the pattern after subtraction of the scattering in the isotropic liquid state T = 80°C); (b) χ-scans over the diffused small angle scattering (for 2θ = 1.5-4°) at 65, 55 and 45 °C, I_{rel} = I(T)/I(80 °C, Iso). Image courtesy (Suppl. Info. ref.[10]).

Fig. 6.3 shows the X-ray diffraction patterns of BR1 under a magnetic field (Fig. 6.3(a)) and χ-scans (Fig. 6.3(b)) over the diffused small angle scattering (for 2θ = 1.5-4°) at 65, 55 and 45°C. It was observed that *d*, associated with the small angle scattering, decreases as the temperature is reduced (*d* varies from 3.16 nm at T = 65°C to 3.12 and 3.10 nm at T = 55°C and 45°C, respectively), indicating that the layer thickness decreases with lowering temperature. The average intermolecular distance for BR1, obtained from the wide-angle peak position, was found to remain unchanged with temperature. The result obtained for the wide angle scattering is not very unusual as the position of this diffuse scattering is not only influenced by the packing of the aromatic cores but also by the alkyl chain. Additionally, the silyl group also has a significant influence on the diffuse scattering. Due to the broad nature of the wide angle scattering peak, it was not possible to separate the individual contributions.

6.3 Experimental Method

The typical cell thickness used in the experiment was ~ 5 - 26.2 μm. The empty capacitance of the cell was measured before filling it with the material. The sample was then filled via capillary action by heating the empty cells into the isotropic phase using a temperature controller. We noted that filling the sandwich cells with this material took considerable amount of time in comparison to the BCNs and bimesogens studied in the previous chapters, indicating a large viscosity of the sample. The electro-optical set-up was used to inspect the optical textures and phase transition of the material and study the electro-optical behaviour.

The perpendicular component of the dielectric permittivity was obtained from the measurements on a planar cell, using a Novocontrol Alpha High Resolution

Dielectric Analyzer (Novocontrol Gmbh, Germany). The parallel component of permittivity, determined from homeotropic configuration, was obtained by placing the planar cell inserted in the hot-stage placed between the poles of a large electromagnet, and by applying a magnetic field (**B**) of strength 1 Tesla to orient the director, **n** along the magnetic field (Figure 6.2(b)). The dielectric permittivity was measured in the frequency range of 1 Hz to 10 MHz as the sample was cooled slowly from the isotropic state.

6.4 Results and Discussions

6.4.1 Optimization of Cell Thickness

Preliminary investigations in the planar and homeotropic cells revealed that the material aligns reasonably well in a planar cell; however it does not align well homeotropically. While it was readily possible to obtain the perpendicular component using a homogeneously aligned cell, the parallel component was determined by inducing a homeotropic state by applying a 1T field across the originally planar cell, as depicted in Fig. 6.2(b). In order to obtain a reasonable homeotropic alignment from the maximum possible magnetic field strength (1 Tesla), the cell thickness (d) was optimized until a satisfactory alignment was achieved. The critical field for the onset of the director deformations [11], B_{th}, is inversely related to the cell thickness d; $B_{th} = \frac{\pi}{d}\left(\frac{\mu_0 K_{11}}{\Delta\chi}\right)^{1/2}$, where μ_0 and $\Delta\chi$ are the magnetic permeability of free space and diamagnetic anisotropy, respectively. Hence, a larger d implies a smaller threshold field for *Freedericksz* transition. This would enable a complete switching of the cell to a homeotropic state for the maximum applied field.

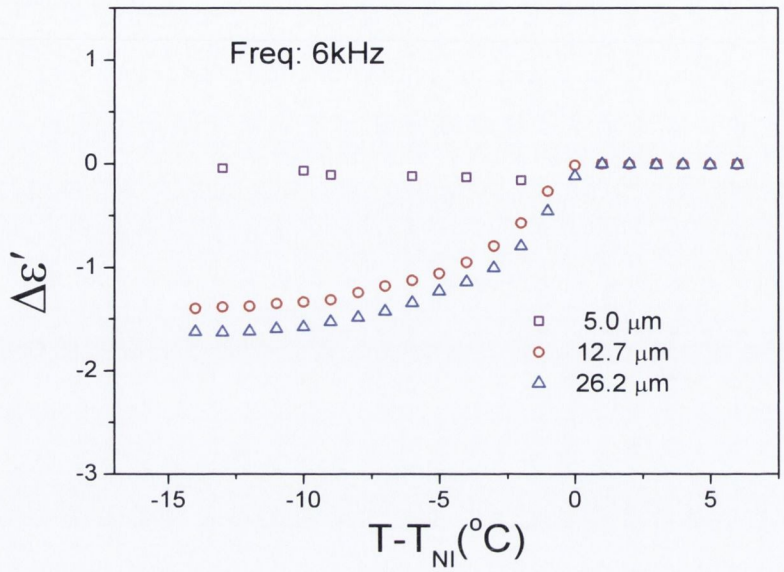

Figure 6.4: The dielectric anisotropy at frequency 6 kHz is compared for three different cells (~ 5, 12.7 and 26.2 μm), showing the changes in its values as the thickness is increased. In the 5 μm cell, Δε′~0 indicating that the cell has not switched to the homeotropic state; however the change is much more noticeable in cells of 12.7 and 26.2 μm. The difference in Δε′ between the 12.7 and 26.2 μm cells are not as large and hence it can be safely assumed that the alignment has switched to the homeotropic state in the thicker cell.

The optimum cell thickness, that would enable a reasonable homeotropic state, was determined by comparing the dielectric anisotropy at a pre-selected frequency for three different cell thicknesses. Fig. 6.4 compares the values of $\Delta\varepsilon'$, evaluated by subtracting the permittivities obtained for the induced homeotropic ($\varepsilon'_{\parallel}$) alignment and originally planar ($\varepsilon'_{\perp}$) cell, for cell thicknesses (5, 12.7 and 26.2 μm) at a frequency of 6 kHz. It can be seen that for a 5 μm cell, a magnetic field of 1T is not sufficient to switch it to the homeotropic state. As the cell thickness is increased, significant changes can be seen in the results. As seen from Fig. 6.4, there is considerable difference in the

value of $\Delta\varepsilon'$ between the 5 and 12.7 μm cells, while this difference is greatly reduced between the 12.7 and 26.2 μm cells. For cell thicknesses greater than 26.2 μm, this difference is expected to be even smaller. Hence, it can be assumed that for a 26.2 μm cell, a field of 1T is reasonably high enough to align it homeotropically. Consequently, the dielectric results presented in the remainder of this chapter are obtained from the 26.2 μm cell.

6.4.2 Dielectric and Electro-Optical Studies

The temperature dependence of the real part of dielectric permittivities, $\varepsilon'_{\perp}$ and $\varepsilon'_{\parallel}$, and the average permittivity, $< \varepsilon' >$, is depicted in Fig. 6.5 for pre-selected frequencies of 100 Hz, 6, 12 and 90 kHz. The figure clearly demonstrates that the sign of $\Delta\varepsilon'$ is positive at lower frequencies and becomes negative at higher frequencies. The most interesting aspect is that the average permittivity decreases with a reduction in temperature. Usually, if $< \varepsilon' >_N = < \varepsilon' >_{iso}$ (values extrapolated from those in the isotropic phase to that in the LC phase) then it implies that the *g*-factors are unity. However, if the average permittivity in the liquid crystal phase is smaller than $< \varepsilon' >_{iso}$, as is the case for the material under study, then this suggests that there is tendency for anti-parallel correlation of some of the dipoles.

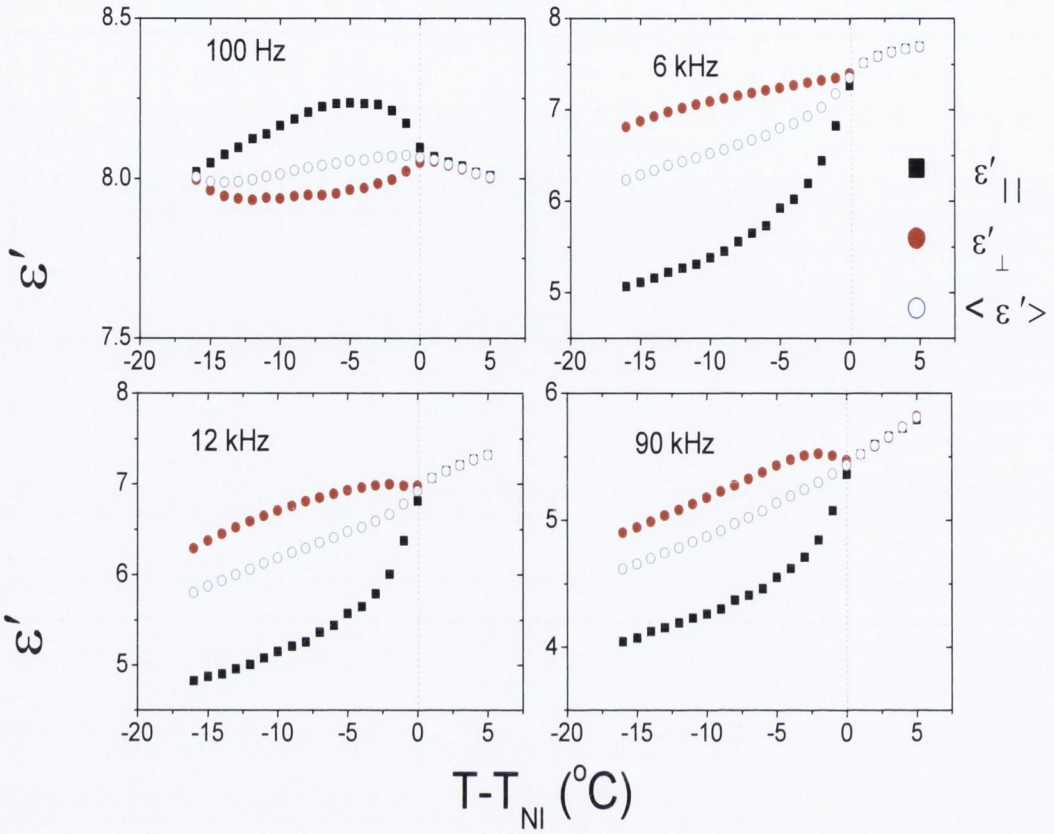

Figure 6.5: The real part of dielectric permittivity plotted as a function of reduced temperatures for frequencies 100 Hz, 6, 12 and 90 kHz. The values of $\varepsilon'_{\parallel}$ (■) and $\varepsilon'_{\perp}$ (●) are obtained from the homeotropic and planar configurations, respectively. $<\varepsilon'>$ (○) is the average permittivity, defined as $\frac{1}{3}(\varepsilon'_{\parallel}+2\varepsilon'_{\perp})$.

The sign reversal of the dielectric anisotropy at lower frequencies was also confirmed using the optical contrast spectroscopy. This technique is not severely influenced by the presence of ions in the medium as the dielectric studies are, at lower frequencies. Fig. 6.6 (a) presents the transmittance change as a function of temperature

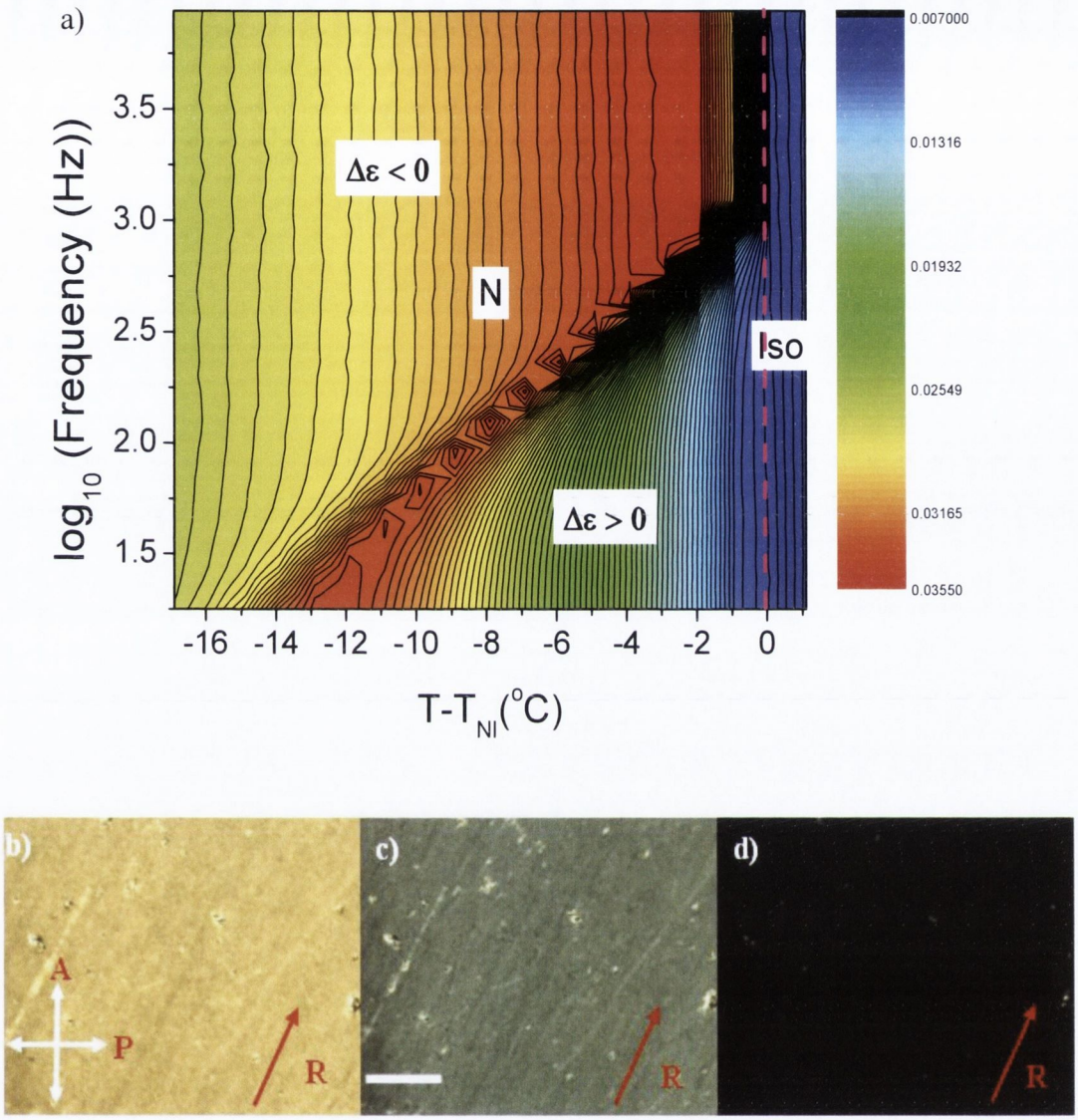

Figure 6.6: (a) Frequency-temperature plots of the transmittance curve obtained in a 5μm planar cell under an applied field of 2 V/μm. The contour line implies a constant value of transmittance. (b,c,d) Textures obtained between crossed polarizers at $T-T_{NI}$ = -5°C: (b) no field applied, (c) 6 V_{pk} applied across the cell at frequency of 50 Hz, (d) 15V_{pk} applied at frequency of 50 Hz, cell switches to homeotropic state. R (red- arrow) denotes the rubbing direction, set at angle ~22.5 degrees from the polarizer axis. Length of white bar is 60μm. All pictures were taken at an exposure time of 130 ms.

and frequency (plotted on $\log_{10}$ scale) using the optical spectroscopy technique. Measurements were carried out on a 5 μm planar cell as the material was cooled from the isotropic to the nematic phase, under an electric field of ~ 2 V/μm applied across the cell. In Fig. 6.6 (a), the lines represent constant transmittance while the colours depict arbitrary levels of transmittance. The crowded lines are related to a rapid change in transmittance due to *Freedericksz* transition. For a reduced temperature $T-T_{NI} = -5^{o}C$, the material shows positive $\Delta\varepsilon'$ for frequencies < 300 Hz and its value becomes negative at frequencies greater than 300 Hz. As seen from Fig. 6.6(a), the sign reversal of $\Delta\varepsilon'$ is observed as a function of frequency; however there is no particular temperature for which the sign reversal is observed. Such a behaviour is similar to that observed in conventional DFNs composed of calamitic molecules, with the exception that it occurs at much lower frequencies in this material.

Figures 6.6 (b, c and d) show the textures obtained at reduced temperature, $T-T_{NI} = -5^{o}C$, using polarizing optical microscopy. *Freedericksz* transition effects were observed at lower frequencies (<<1 kHz); for example, see Fig. 4 (c, d) for frequency 50 Hz. However no electrohydrodynamic patterns were observed for a maximum applied field of 5V/μm and frequencies up to 20 Hz. Thus confirming that the change in transmittance spectra obtained in Fig. 6.6(a) is due to *Freedericksz* transition alone.

In order to obtain better information about the various dielectric modes of the system, the derivative of the real part of permittivity with respect to ln(f), $d\varepsilon'/d(\ln f)$ [15] for both sets of data was analyzed (Fig. 6.8 (c) and (d)) using the equations [15]:

$$\frac{d\varepsilon'}{d(\ln f)} = \frac{d\varepsilon'}{d(\ln \omega)} = \sum_{j=1}^{n} \mathrm{Re} \frac{\delta\varepsilon_j \alpha (i\omega\tau_j)^{\alpha}}{[1+(i\omega\tau_j)^{\alpha}]^2}, \qquad (6.11)$$

$$\frac{d\varepsilon'}{d(\ln\omega)} = \sum_{j=1}^{n} \frac{\delta\varepsilon_j \alpha_j (\omega\tau_j)^{\alpha_j} \left\{ 2(\omega\tau_j)^{\alpha_j} + [1+(\omega\tau_j)^{2\alpha_j} \cos\frac{\pi\alpha_j}{2}] \cos\frac{\pi\alpha_j}{2} \right\}}{[1+(i\omega\tau_j)^{2\alpha_j} + 2(\omega\tau_j)^{2\alpha_j} \cos\frac{\pi\alpha_j}{2}]^2},$$

(6.12)

here j is the variable denoting the number of relaxation processes up to n, τ_j is the relaxation time of the j-th process (related to the relaxation frequency f_j or angular frequency ω_j as: $\tau_j = 1/\omega_j = 1/2\pi f_j$), α is a fitting parameter, and $\delta\varepsilon_j$ is the dielectric relaxation strength of the j-th process. The dielectric strength ($\delta\varepsilon_j$) for each process is determined from the fitting to the above equation.

We find that the derivative method for analysis of the dielectric modes is more convenient than using the dielectric loss spectrum alone, as it offers better resolution of the peaks. Moreover, the dielectric loss data includes dc conductivity, whose effect is rather dominant at lower frequencies, making the spectra difficult to deconvolute. The peak positions resolved using the derivative technique lie at the same positions as for ε'', as demonstrated in Fig. 6.7 (a, b). For the planar state, four processes are resolved using the derivative technique. These are P1, P2, P3, plus the highest frequency peak P_{ITO}, which is due to the ITO resistance. Similarly for homeotropic alignment (Fig. 6.7 (b)), three peaks H1, H2, H_{ITO}, are clearly seen. An additional peak H0 ($\delta\varepsilon$ = 0.95) appears at lower frequencies (f<10Hz), below peak H1, however this can only be resolved at temperatures close to the phase transition. The dielectric strength for the processes is plotted as a function of reduced temperatures in Fig. 6.8. The temperature dependence of the relaxation frequencies is presented by the Arrhenius plot in Fig. 6.9, where the relaxation frequency f_R is plotted versus the inverse absolute temperature 1/T.

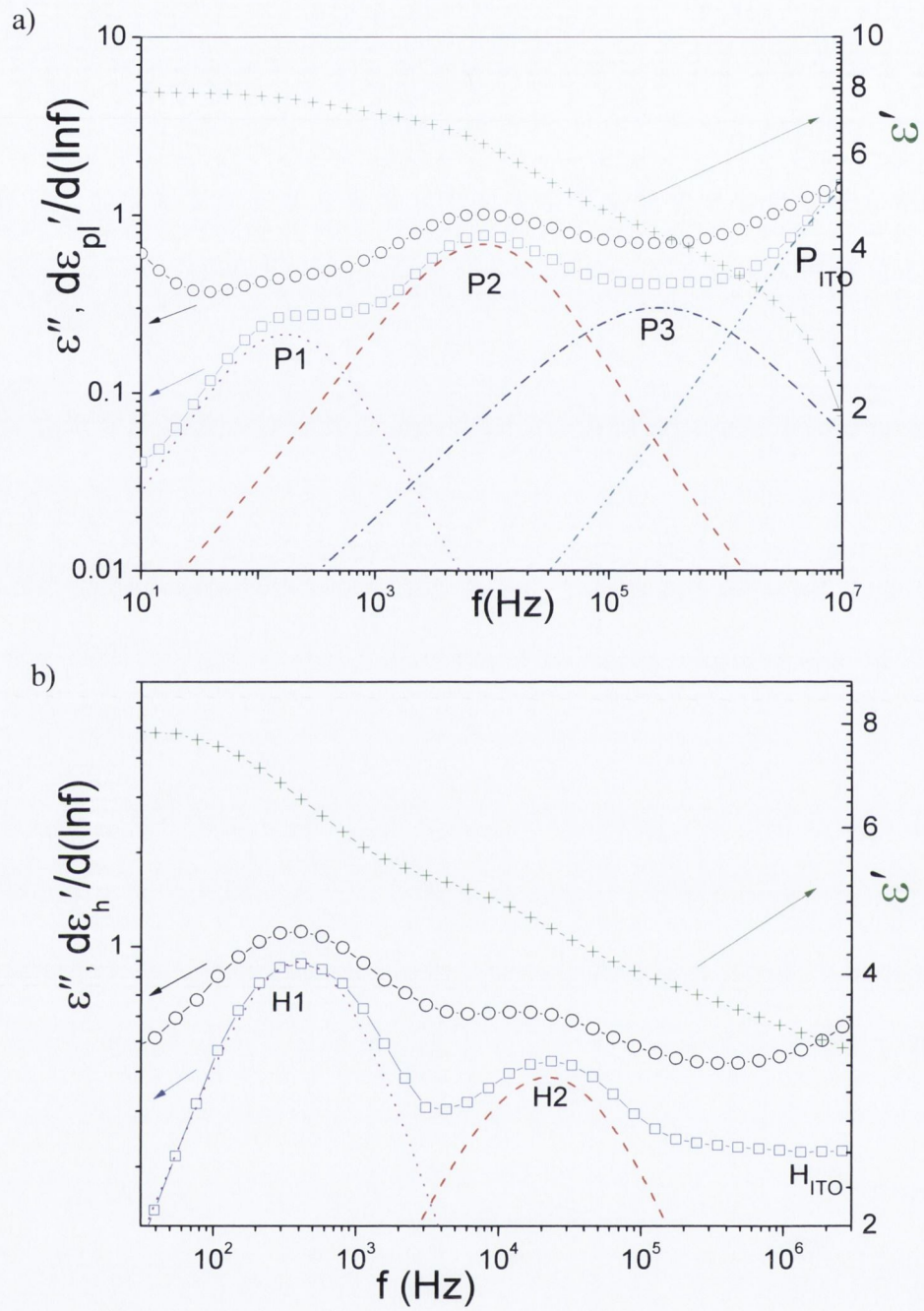

Figure 6.7: Frequency plot of the relative dielectric permittivity obtained from (a) planar (at $T-T_{NI}$ = - 22°C) and (b) homeotropic cell (at $T-T_{NI}$ = - 16°C): (+ symbol + line) denotes ε', (○ symbol + line) denotes ε'', (□ symbol + line) represents $d\varepsilon'/d(\ln f)$, the derivative of ε' with respect to (ln*f*). The dot, dash, dash-dot and dash-dash dot line in are the deconvoluted components of $d\varepsilon'/d(\ln f)$. P1, P2, P3 and P_{ITO} are the relaxation peaks for the planar cell; H1, H2 and H_{ITO} are modes obtained in the homeotropic configuration.

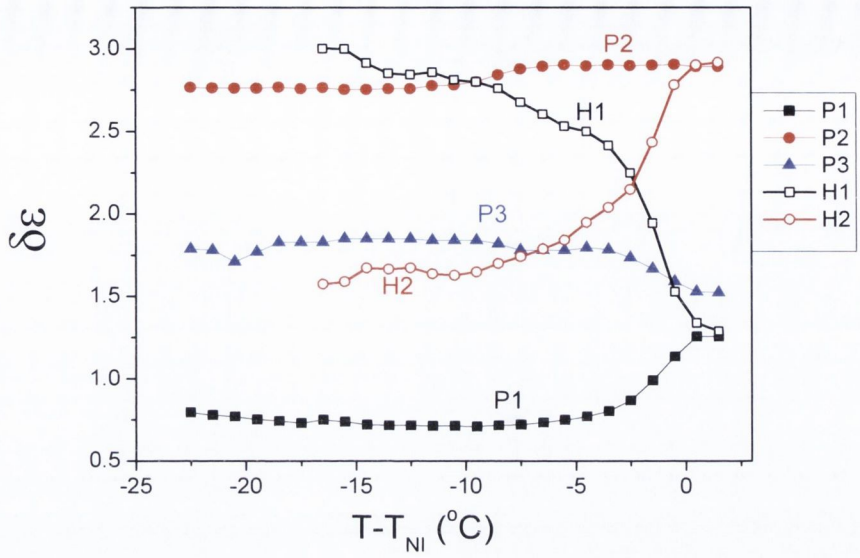

Figure 6.8: The dielectric strength ($\delta\varepsilon$) corresponding to the various relaxation processes P1, P2, P3 (planar configuration), and H1, H2 (homeotropic configuration) as a function of the reduced temperature.

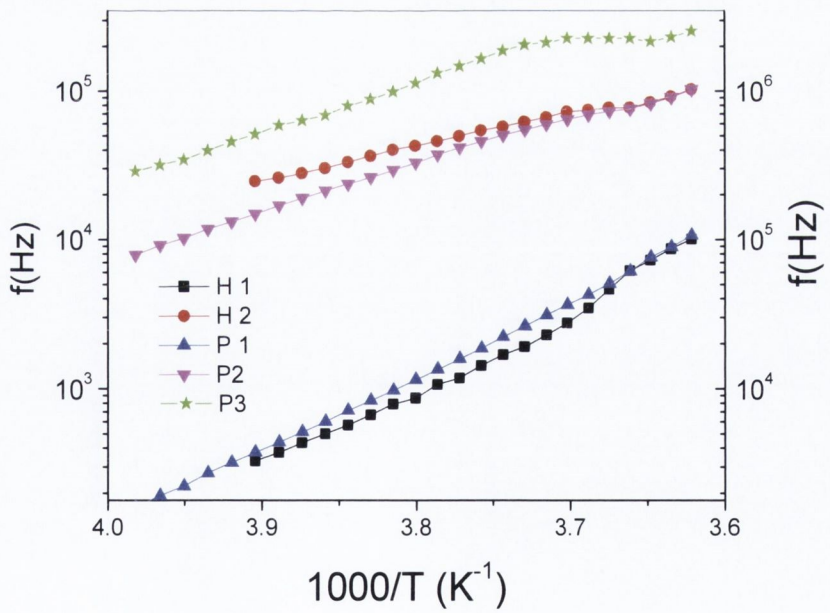

Figure 6.9: Relaxation frequency (f_R) for the various relaxation processes as a function of the inverse temperature (in K^{-1}).

In order to interpret the dielectric results, we refer to the M-M equations described in section 6.1.1. From equations 6.1 and 6.2 we see that μ_l and μ_t are the determining factors for the temperature dependency of $\delta\varepsilon$. In liquid crystalline molecules, various conformations are possible due to the intra-molecular degrees of freedom. As the temperature is lowered, conformations may change the angle between the effective dipole moment and the long molecular axis. This affects the overall dielectric results in such systems. Studies [16] on some bimesogens constituted of rod-like mesogens have revealed the influence of the conformational change in the dielectric results in these classes of materials. The changes arising from the orientation of one of the constituent mesogens, due to the change in the conformational state of the flexible spacer, causes a change in the magnitude and direction of the dipole moment with temperature. This results in a low frequency dielectric relaxation [16] in such systems. Such conformational changes in BR1 could be responsible for the observed low frequency relaxations. However, the bimesogenic molecule studied here is too large to show relaxation as a whole, and it is also unlikely to show relaxation at frequencies much greater than 10 Hz. It is more likely that the dynamic and orientational behaviour of the constituent mesogens are fairly decoupled from each other. Therefore it is reasonable to consider the contribution of each mesogen to the dielectric permittivity independently, plus a small contribution from the SiOSi electric dipole moment.

As mentioned above, due to a large size of the dimesogen it is unlikely that the whole molecule, by itself, can rotate that easily. It is possible that each constituent mesogen may rotate along its own long and short axes. Hence, we consider the relaxation of each constituent mesogens separately. Using the M-M equations we estimated the internal field factors for the reaction field *(F)* and cavity field *(h)* at the

transition temperature where $S \cong 0$, and the following values were obtained: F=1.42 and h=1.44. The number density was calculated to be $N = 0.43 \times 10^{27}$ m^{-3} by assuming material density to be 1100 kg/m^3. Thus the scaling factor $A\left(=\frac{NhF^2}{3\varepsilon_0 k_B}\right)$ was determined to be 3.35×10^{60} $KC^{-2}m^{-2}$.

From the M-M Eqns. (6.1) and (6.2), one can see that the dielectric strength of each relaxation process is primarily a function of the order parameter S. By comparing the temperature dependence of $\delta\varepsilon$ for the different relaxation processes in Fig. 6.8 it is quite evident that the dielectric strength of peaks P1, H2, are proportional to $(1\text{-}S)/T$, and H1 and P3 are proportional to $(1+2S)/T$ and $(1+S/2)/T$ respectively. The temperature dependence of peak P2 looks rather peculiar, but such behaviour could be due to large anisotropic correlations of the dipole components.

Solid lines in Fig. 6.10 show how the M-M model reproduces the experimental data for the homeotropic configuration, as an example. Blue and magenta lines show the temperature dependence of H1 and H2 on the $(1+2S)$ and $(1\text{-}S)$ term, respectively, of Eqn (6.1). Similarly, P1 and P3 showed $(1\text{-}S)$ and $(1+S/2)$ dependence with temperature, respectively, for the fit of the corresponding dielectric strengths to Eqn. (6.2). By analyzing the fitting of the dielectric strength data to the M-M model and corresponding relaxation frequencies, we can assign a relaxation mode to each process. The lowest frequency peak H0, observed in the homeotropic configuration, is assigned to the relaxation of the longitudinal dipole component of the bent core mesogen. Peaks H1 and P1 correspond to the relaxations of the longitudinal dipole components of the rod-like (RL) mesogen. The processes P2 and H2 are due to the relaxation of the transverse dipole components of the BC mesogen, while P3 corresponds to the relaxation of the

transverse component of the RL mesogen. The highest frequency peaks, H_{ITO} and P_{ITO}, are attributed to ITO contribution.

The fit to the M-M equations also yields the longitudinal (μ_l) and transverse (μ_t) components of the molecular dipole moment. Using Eqns. (6.1) and (6.2), the square of the effective total dipole moment μ_{eff}^2 [$= (\varepsilon(0)-n^2)T/A$], by assuming $S \cong 0$ at the phase transition], was evaluated to be 61.8 D^2, thus μ_{eff} =7.86 D. The mesogenic units of the material under study are linked by a flexible spacer and hence it is more likely that their reorientation is more or less independent from each other. For the case of independent reorientations we have four contributions to the dielectric permittivity which are related to square of dipole moments ($\mu_{l\,BC}$, $\mu_{t\,BC}$, $\mu_{l\,RL}$ and $\mu_{t\,RL}$). The dipole moment of each component is calculated using its corresponding dielectric strength. These are found as follows: $\mu_{l\,BC}$=2.97D, $\mu_{t\,BC}$=5.21D, $\mu_{l\,RL}$=3.41D, $\mu_{t\,RL}$=3.76D.

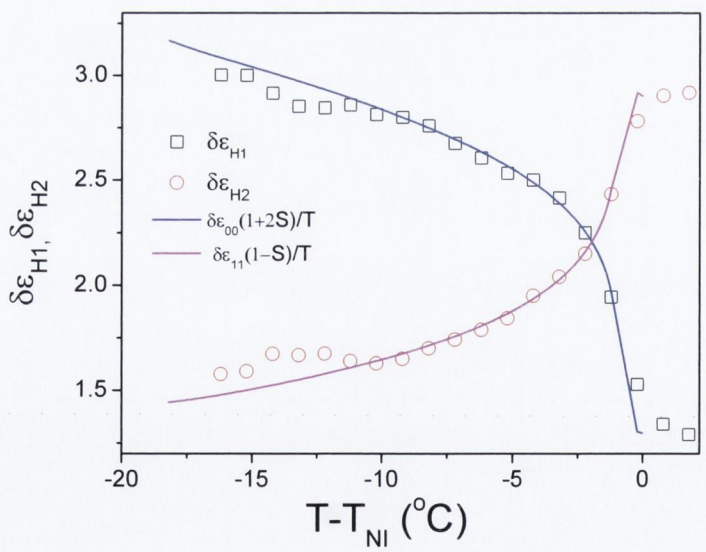

Figure 6.10: The dielectric strength corresponding to H1 (□) and H2 (○) versus reduced temperature; fit to the M-M model is depicted by the solid lines.

The order parameter, S (Fig. 6.11) was calculated from the homeotropic configuration (as it is less influenced by surface boundaries) by using the dielectric strength corresponding to both H1 and H2 mode and applying the scaling factor A to the corresponding $\delta\varepsilon$ data in the temperature range below the Iso-N transition. If we assume $g_{||} = 1$, then the order parameter determined from H2 is slightly higher than obtained from H1. In order to achieve self-consistency of the results, we allow $g_{||}$ to depart from unity ($g_{||} \cong 1.05$, see Fig. 6.12). Fig. 6.11 shows the resulting S evaluated from the experimental data, and its fit by the power law $(1\text{-}T/T_{NI})^{\gamma}$, where γ is the critical exponent ($\gamma = 0.24$); the value of γ depends on the molecular structure. Interestingly, S does not show a first-order transition and this is presumably due to the non-uniform alignment of the sample. The same S data was used to reproduce experimental data for planar alignment by allowing $g_{\perp}$ to be different. The determined correlation factors show relatively different temperature behaviours, as seen from Fig. 6.12.

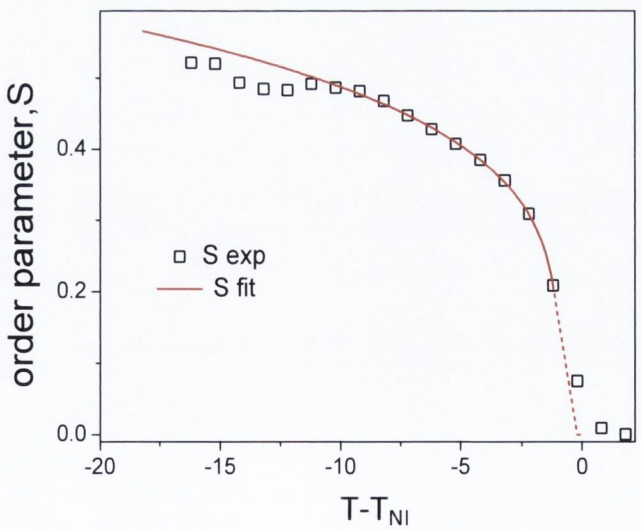

Figure 6.11: The order parameter as a function of temperature calculated from the experimental data for the homeotropic cell. Solid red line represents the fit of S to the power law $(1\text{-}T/T_{NI})^{\gamma}$; γ is the critical exponent = 0.24.

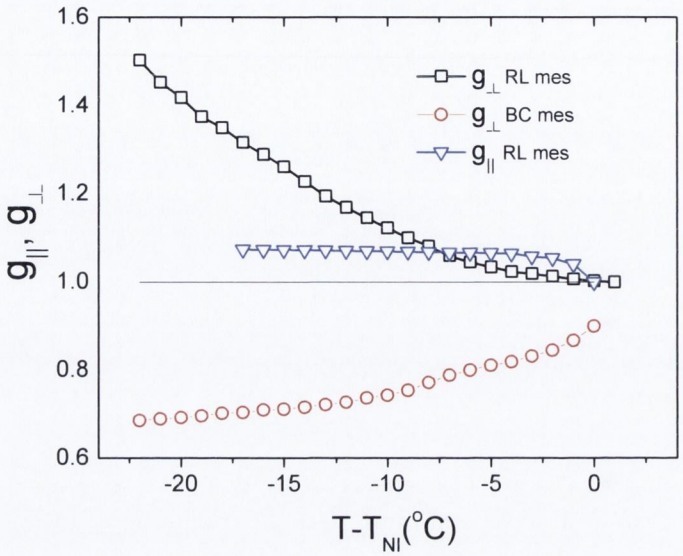

Figure 6.12: Temperature dependencies of the g-factors. $g_{||}$ and $g_{\perp}$ are the anisotropic Kirkwood correlation factors for the director parallel and perpendicular to the electric field respectively. The text RL and BC refer to rod-like and bent-core mesogens, respectively.

Fig. 6.12 shows the variation of the g-factors as a function of temperature. $g_{\perp}$ and $g_{||}$ for the rod-like mesogen is seen to increase from unity at the transition temperature to ~1.5 and ~1.05, respectively, while $g_{\perp}$ associated with the bent-core mesogen is seen to decrease to ~0.7. The theoretical evaluation of the anisotropic correlation factors requires a detailed microscopic model. A model proposed by Jeu et al.[17] considers the clusters as smectic like structures on the assumption that S =1, so that the molecules are constrained to be either parallel or anti-parallel to the director axis. If the molecular dipole lies at an angle β with respect to the long molecular axis, the anisotropic dipole-dipole correlation factors can be written as [11]:

$$g_{\parallel} = 1 - \frac{n\mu^2 \cos^2\beta \left\langle 3\left(\frac{r_z}{r}\right)^2 - 1 \right\rangle}{4\pi\varepsilon_0 r^3 k_B T}, \qquad (6.13)$$

$$g_{\perp} = 1 - \frac{n\mu^2 \sin^2\beta \left\langle 3\left(\frac{r_x}{r}\right)^2 - 1 \right\rangle}{8\pi\varepsilon_0 r^3 k_B T}. \qquad (6.14)$$

Here n is the number of neighbours; $\langle r \rangle$ is defined as the average distance between two molecules, r_z is the average separation perpendicular to the layers and r_x is the in-plane separation. For a smectic order, $r_z >>$ in-plane separation, and this results in $g_{\parallel} < 1$. If $\langle r_x^2 \rangle < \langle r^2/3 \rangle$, we get $g_{\perp} > 1$ indicating parallel alignment of the dipoles in the smectic layer. From the experimental data obtained here for BR1, we find that $g_{\perp}$ factor for the rod-like mesogen is greater than one, which is usual in smectic order. This indicates parallel correlation of transverse dipoles, which is seen to grow with decreasing temperature. On the contrary the $g_{\perp}$ factor for bent-core mesogen is below one, which indicates rather anti-parallel correlation of transverse dipoles, and this tendency of anti-parallel association increases with lowering temperature.

Similar studies performed on three bent-core liquid crystals (C4, C7, and C9), with the same mesogenic core unit (4-cyanoresorcinol bisbenzoate) as BR1, but different terminal groups [8] revealed that the temperature dependencies of permittivity were related to a change in the strong anisotropic correlations among the molecules. On increasing of the chain length, it was found that the separation along the layer normal increases but corresponding separation within the layer decreases. As a result $g_{\perp}$

gradually increases and $g_{\|}$ decreases. The cluster size was also found to increase with decreasing temperature.

In the dimesogen studied here, attaching the rod-like mesogen laterally to the 4-cyanoresorcinol bisbenzoate unit may also reinforce dipole-dipole interactions, perhaps in a different manner, resulting in the modified correlation factors $g_{\perp}$ and $g_{\|}$. Based on the model suggested by Jeu et al.[17], the temperature dependence of $g_{\perp}$ and $g_{\|}$ observed for BR1 can be explained by a decrease in the average separation perpendicular to the layers *(r_z)* together with an increase in the in-plane separation *(r_x)*. The introduction of a laterally attached rod-like mesogenic core will indeed increase the separation of the bent-core mesogenic units within layers, but at the same time the effective layer thickness is significantly reduced (d - 3.2 nm, from the X-ray data) either due to a large tilt angle (50^{o}) [14] and/or (inter) layer (inter) penetration, thus decreasing the separation length perpendicular to layers, $<r_z>$. Moreover the analysis of the dielectric modes of BR1 also indicates that the laterally attached rod-like mesogenic core unit may bring $g_{\perp}$ below unity and increase $g_{\|}$. These may result in a possible arrangement of molecules within the smectic-like clusters, wherein the transverse dipoles interact in an anti-parallel manner (note $r_z < r_x$), as illustrated by the model shown in Fig. 6.13. The tilt angle represents the tilt of the molecules in the Sm*C* like clusters. Additionally, the X-ray results reveal that *d*, associated with the small angle scattering, decreases as the temperature is reduced, which indicates that the layer thickness decreases with lowering temperature. This is consistent with the model proposed.

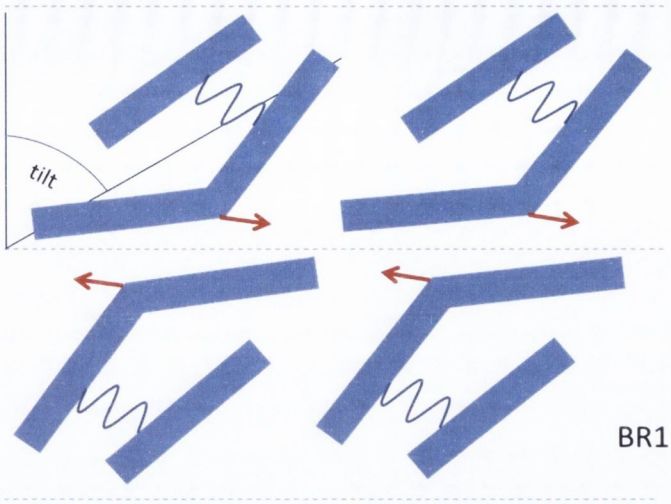

Figure 6.13: Possible arrangement of the mesogenic units in smectic layers. The system in the nematic phase has a local smectic-like structure.

The proposed arrangement of molecules within a cluster indicates an anti-parallel interaction of the transverse dipoles between the neighbouring layers. In order to investigate if there is an emergence of any local anti-ferroelectric structure, we performed polar switching measurements based on the current repolarization technique. These studies revealed that in the entire nematic range of BR1, no polar switching is observed under an applied triangular wave, even at relatively high applied voltages (30V/μm, 5 μm planar cell, frequencies: 0.1 – 30Hz). This shows the apolar nature of the clusters.

6.5 Conclusion

We studied the dielectric behaviour of the dimesogen BR1 composed of a bent-core unit combined with a laterally attached rod-like mesogenic core. The material shows sign reversal of the dielectric anisotropy as a function of frequency, and the

behaviour is similar to that observed in DFNs composed of rod-like mesogens. However the sign reversal occurs at much lower frequencies in comparison to the calamitic/bent-core mesogens explored previously, arising presumably from the larger size of the bimesogen. On transition to the nematic phase, the average permittivity is seen to decrease as the temperature is lowered, indicating occurrence of an anti-parallel association of some of the dipoles in the system. Our analysis of the dielectric spectra using the Maeir-Meier (M-M) model suggests the presence of anti-parallel correlation of the transverse dipoles in the neighbouring layer of the Sm*C* like clusters. Based on this, a model was proposed for the possible arrangement of molecules within the clusters, which is also supported by the X-ray scattering studies on this material.

References

[1] G. Dantlgraber, S. Diele and C. Tschierske, *Chem. Comm.* **23**, 2768-2769 (2002).

[2] M.G. Tamba, B. Kosata, K. Pelz, S. Diele, G. Pelzl, Z. Vakhovskaya, H. Kresse, and W. Weissflog, *Soft Matter* **2**, 60-65 (2006).

[3] C.V. Yelamaggad, S.K. Prasad, G.G. Nair, I.S. Shashikala, D.S.S. Rao, C.V. Lobo and S. Chandrasekhar, *Angew. Chem. Int. Ed.* **43**, 3429-3432 (2004).

[4] G. Shanker, M. Prehm, and C. Tschierske , *Beilstein J Org Chem.* **8**, 472–485 (2012).

[6] E.P. Raynes and I. Shanks, *Electron. Lett.*, 1974,**10**, 114-115; M. Schadt, *Annu. Rev. Mater. Sci.* **27**, 305-379 (1997).

[7] Y. Jang, V. P. Panov, C. Keith, C. Tschierske, and J. K. Vij, *Appl. Phys. Lett.* ***97***, 152903 (2010).

[8] Y. Jang, V. P. Panov, A. Kocot, A. Lehmann, C. Tschierske and J. K. Vij, *Phys. Rev. E* **84**, 060701 R (2011).

[9] S. A. Jewell and J.R. Sambles, *Appl. Phys. Lett.* **87**, 021106 (2005).

[10] G. Shanker, M. Prehm and C. Tschierske, *J. Mat. Chem.* **22**, 168 (2012).

[11] D. Dunmur and K. Toriyama, in *Handbook of Liquid crystals*, ed. D. Demus, J. Goodby, G.W. Gray, H.W. Speiss and V.Vill, Wiley-VCH: Weinheim Vol. 1, 1988, pp. 231-252.

[12] D.A. Dunmur, *Liquid Crystals*, **10,** 1379 (2005).

[13] D. Dunmur, A Fukuda, G. R. Luckhurst, *Physical Properties of Liquid Crystals: Nematics*, Institution of Engineering and Technology, 2001.

[14] P.L.Nordio, G. Regatti and U. Segre, *Molecular Phys.*, **25**, 129 (1973).

[15] K. Merkel, A. Kocot, J. K. Vij, G. H. Mehl and T. Meyer, *Phys. Rev. E* **73**, 051702 (2006,); K. Merkel, A. Kocot, J. K. Vij, G. H. Mehl, and T. Meyer, *J. Chem. Phys.* **121**, 5012-5021 (2004).

[16] M. Stocchero, A. Ferrarini, G. J. Moro, D. A. Dunmur and G. R. Luckhurst, *J. Chem. Phys.* **121,** 8079 (2004).

[17] W. H. de Jeu, W. J. A. Goossens, and P. Bordewijk, *J. Chem. Phys.* **61**, 1974, (1985).

Chapter 7

Conclusion and Future Work

7.1 Conclusion and Summary

The knowledge of the material parameters of a liquid crystal, such as dielectric anisotropy and elastic constants, is very important in the design and optimization of LC based devices. The reorientation of NLC molecules under an applied electric field, caused by the dielectric anisotropy, is a fundamental physical property employed in numerous modern LC based technologies, while the elastic constants determine the threshold voltage for director deformation. The molecular structure or shape of a liquid crystal can also significantly influence these parameters, for example: in conventional rod-like molecules usually $K_{33} > K_{11}$, while in many bent-cores and bimesogens it has been found experimentally that $K_{33} < K_{11}$. Hence, an understanding of the factors that affect these properties is vital in the field of liquid crystal research. The work presented in this thesis was primarily concerned with the study of material parameters such as dielectric anisotropy, elastic constants and flexoelectric coefficients in the nematic phase of some bent-core mesogens and bimesogens, and the factors that influence the observed results were discussed. A brief summary of the research work undertaken is described below.

In the first part of the chapter, we investigated the flexo-elastic properties of three bent core materials belonging to a homologous series. There is a continued interest

in studying the elastic properties of LC materials as they play an important role in determining the switching properties of LC based applications. The flexo-elastic properties, especially in BCNs, are of particular interest as they are predicted to be different from that usually observed in rod-like molecules. In one study the value of $|e_3|$ was measured to be higher by a factor of 10^3 than for calamitic liquid crystals. Furthermore, there is a disagreement in literature as to what factor causes the observed results; smectic-like clusters or the bent shape of the molecules. In order to gain a better understanding and resolve this discrepancy we determined the elastic constants in materials where the clusters were present in two of the compounds, while it was measurably absent in the material with the shortest chain length. We found that the bend elastic constant K_{33} is smaller than K_{11} in all materials studied, irrespective of the chain length or presence/absence of clusters. This confirmed that the elastic properties are more likely to be influenced by the bent shape rather than clusters. The effective flexoelectric coefficients in all three materials were obtained to be in the range of tens of pC/m and any evidence of giant flexoelectricity was excluded in our studies.

Next we investigated the physical properties of some odd bimesogens which exhibit the second nematic phase below the higher temperature classical nematic phase. The N_{tb} phase of these materials has attracted significant attention in recent years due to a number of interesting properties exhibited by them, such as the spontaneous appearance of stripes, microsecond linear response etc. The theoretical studies pertaining to the fascinating properties observed in this phase are still is in its initial stages and needs a lot of careful study. However, the parameters of the ordinary nematic phase, the theory for which is well established, could also reveal useful information about the lower temperature twist bend nematic phase. In Chapter 4, we obtained the

splay and bend elastic constants, the effective flexoelectric coefficient in the nematic phase, and flexoelectric polarization in both the nematic and twist nematic phase of a bimesogen CBC11CB. It was found that K_{11} increased with decreasing temperature, but the value of K_{33} tended to fall steadily after an initial increase on transition from the isotropic phase. Though the bend elastic constant was seen to fall by a factor of almost three with decreasing temperature, its sign was still positive and did not seem to go to zero or become negative for the temperature ranges measured. It is still an open question whether the negative value of the bend elastic constant may be a necessary condition for the emergence of the N_{tb} phase. However, a small value of K_{33} is important for the existence of this phase. The effective flexoelectric coefficient was observed to be nearly independent of temperature after an initial increase below the isotropic-nematic transition. $|(e_1 - e_3)|$ for CBC11CB was obtained to be much larger in comparison to conventional calamitics and almost twice higher for CBC11CB than that reported for another odd symmetric bimesogen. The flexoelectric polarization in the N phase was found to be almost 2.5 times higher than in rod-like molecules. Additionally, P_f was obtained to be ~ twice as larger in the N_{tb} phase than in the nematic phase. The large P_f is presumably the source of the electroclinic effect observed in this phase.

In Chapter 5, we presented the results close to the N-N_{tb} phase where a new type of striped pattern was observed under a polarizing microscope in some odd bimesogens and their mixtures with the monomer (5CB) in a planar cell. These macroscopic structures are the second type of spontaneous striped patterns to be observed in odd-spacer linked bimesogens, and appear normal to the rubbing direction (R), as opposed to the first kind of stripes which are parallel to R. These micrometer scale stripes are often

accompanied by the appearance of rainbow colours, and are present only in a narrow temperature range close to the N-N_{tb} phase transition temperature. The appearance of these patterns and their periodicity was found to be dependent on both the cell gap and concentration of 5CB in the mixture. Above a certain concentration of 5CB, this phenomenon was seen to disappear altogether. Introduction of a second heater revealed that the appearance of 'rainbow colours' was found to be related to the temperature gradient, while the stripes were independent of it. It is possible that large flexoelectric polarization or changes in the elastic constant values close to the phase transition could influence the appearance of these stripes.

In Chapter 6 we studied the dielectric behaviour of the dimesogen BR1 composed of a bent-core unit combined with a laterally attached rod-like mesogenic core. The material shows sign reversal of the dielectric anisotropy as a function of frequency and the behaviour is similar to that observed in DFNs composed of rod-like mesogens, with the exception that it occurs at much lower frequencies in this material. On transition to the nematic phase, the average permittivity was seen to decrease as the temperature is lowered, indicating occurrence of an anti-parallel association of some of the dipoles in the system. A systematic and detailed analysis of the dielectric spectra using the Maeir-Meier (M-M) model and X-ray results suggested the presence of anti-parallel correlation of the transverse dipoles in the neighbouring layer of the Sm*C* like clusters. Based on the results a model was proposed wherein the transverse dipole moments interact in an anti-parallel manner.

7.2 Future Work

The effect of the addition of the chiral dopant on the structure of the N_{tb} phase needs to be explored in more detail. Careful studies need to be performed in order investigate if the chiral additive could stabilise just those chiral domains having the same handedness. It would be interesting to study how the twist elastic constant varies for the materials investigated in this thesis, especially for the materials that exhibit the twist-bend phase, since one of the requirements for the stability of the twist-bend phase is that $K_{11} > 2K_{22}$. The investigation of the elastic and flexoelectric property of the various bimesogenic mixtures as a function of the concentration of 5CB also seems to be a promising topic for future investigations. Apart from these, design of better experimental methods to estimate the flexo-elastic parameters very close to the N-N_{tb} phase transition will help provide useful insights into the understanding the formation of this fascinating phase and the unusual but highly desirable properties exhibited by the N_{tb} phase.

Appendix

A.1 Software

This section provides a list of the softwares used for the measurement or analysis of the experimental data presented in this thesis.

- **OriginLab** (Version 7.5) was used to analyse the experimental data. All figures presented in the thesis are plotted using the Origin program.
- **Visual Basic (VB)** in conjuction with **MATLAB** was utilized in the measurement of the elastic constants. A program written using VB controlled the PEM set-up, while MATLAB was used for data fitting/simulation.
- A programme designed using **LabVIEW** provided necessary control for the optical-contrast spectroscopy technique.

A.2 Materials under study

1. 120F1M7

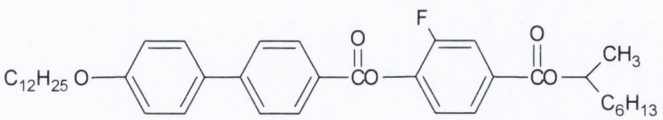

SmC_A* 77.49 SmC_{5Ir} 78.3 SmC_γ^* 79.8 AF 83.3 SmC* 93.5 SmA

2. M2

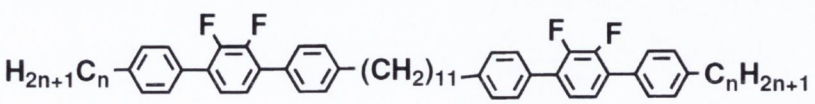

N_{tb} 124.9 N 180 Iso

3. CBC11CB

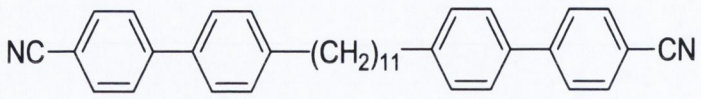

N_{tb} 108.7 N 125.3 Iso

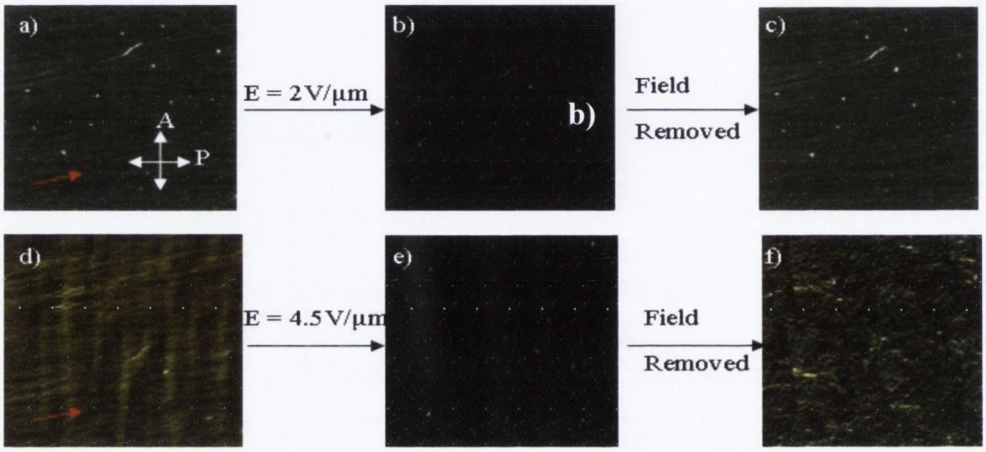

POM textures of CBC11CB obtained in a 5μm planar cell under crossed polarizers. (a) N phase, 109°C, no field applied, (b) complete switching to homeotropic state at E = 2V/μm and frequency of 1Khz, (c) field removed state, (d) uniform N_{tb}, 107.5°C, no field applied; (e) nearly switches to homeotropic at E ~ 4.5V/μm and Frequency of 1kHz; (f) field removed state, the original texture is not recovered, unlike the N phase.

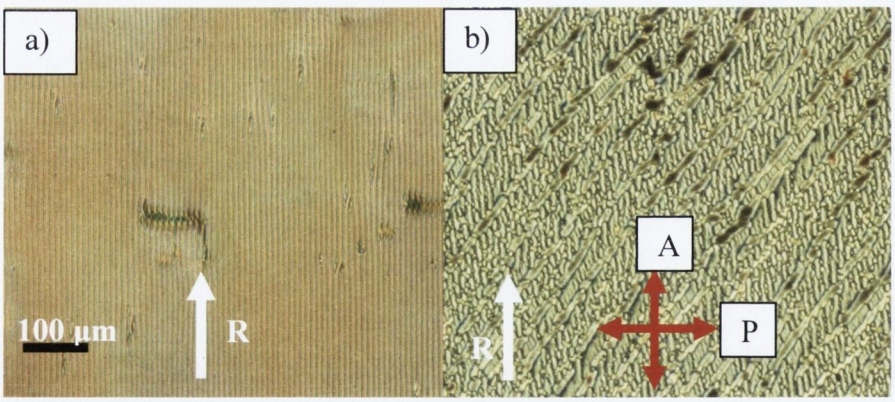

Textures obtained in the N_{tb} phase of CBC11CB in 5 μm planar aligned cells under crossed polarizers of a polarizing optical microscope: (a) in the absence of chiral additive, length of black bar is 100μm, white arrow depicts rubbing direction (R), (b) presence of 3% chiral agent R5011. Addition of the chiral agent dramatically affects the properties of the N_{tb} phase as seen from the non-uniform rope-like textures presented in (b).

List of Publications:

1. **R. Balachandran,** V. P. Panov, J. K. Vij, G. Shanker, C. Tschierske, K. Merkel, and A. Kocot, "Dielectric and Electro-optical studies of a bimesogenic Liquid Crystal composed of bent-core and calamitic units", *Phys. Rev. E*, **90**, 032506 (2014).

2. **R. Balachandran**, V. P. Panov, M. G. Tamba, G. H. Mehl, J. K. Song, and J. K. Vij, "Flexo-electric behavior of bimesogenic liquid crystals in nematic phase -additional self-assembly pattern at the twist-bend nematic and nematic interface", *J. Mat. Chem. C*, **2**, 8179, (2014).

3. **R. Balachandran,** V. P. Panov, J. K. Vij, A. Lehmann and C. Tschierske, "Effects of cybotactic clusters on the elastic properties of bent core liquid crystals: elastic constants and flexoelectric coefficients", *Phys. Rev. E*, **88**, 032503 (2013).

4. **R. Balachandran**, V.P. Panov , J.K. Vij, A. Kocot, M.G. Tamba , A. Kohlmeier and G.H. Mehl, "Elastic properties of bimesogenic liquid crystals", *Liquid Crystals*, **40**, 5 (2013).

5. V. P. Panov , J. K. Vij , **R. Balachandran** , V. Borshch , O. D. Lavrentovich , M. G. Tamba, Georg H. Mehl, "Properties of the self-deforming Ntb phase in mesogenic dimers", *Proc. SPIE, Liquid Crystals*, XV11 **8828**, 88280X (2013).

6. V. P. Panov, **R. Balachandran**, J. K. Vij, M. G. Tamba, A. Kohlmeier, and G. H. Mehl, " Field-induced periodic chiral pattern in the N_x phase of achiral bimesogens", Appl. Phys. Lett., **101**, 234106 (2012).

7. Yun Jang , **R. Balachandran** , C. Keith , A. Lehmann , C. Tschierske and J. K. Vij, "Chirality of an achiral bent-core nematic mesogen observed in planar and homeotropic cells under certain boundary conditions", *Soft Matter*, **8**, 10479-10485 (2012).

8. V. P. Panov, **R. Balachandran**, M. Nagaraj, J. K. Vij,1 M. G. Tamba, A. Kohlmeier,and G. H. Mehl, " Microsecond linear optical response in the unusual nematic phase of achiral bimesogens", *Appl. Phys. Lett.*, **99**, 261903 (2011).

List of Presentations:

1. **R. Balachandran,** V. P. Panov, J.K. Vij, A. Kocot, M.G. Tamba, A. Kohlmeier, and G.H.Mehl, "Flexo-electric properties of Bimesogenic liquid crystals", 25th International Liquid Crystal Conference, Dublin, Ireland, 29th June - 4th July, 2014.

2. **R. Balachandran,** V.P.Panov, A. Kocot, J. K. Vij, , A. Lehmann, C. Tschierske, "Comparison of Elastic Constants of two Bent Core Nematic Liquid Crystals from a Homologous series", 24th International Liquid Crystal Conference, Mainz, Germany, 19th - 24th August, 2012.

3. V. P. Panov, **R. Balachandran**, J. K. Vij, M. G Tamba, A. Kohlmeier, G. H Mehl, "Field-induced linear optical response domains in the N_X phase of achiral bimesogens",_24th International Liquid Crystal Conference, Mainz, Germany, 19th - 24th August, 2012.

4. J. K. Vij, V. P. Panov, M. Nagaraj, **R. Balachandran**, M. G Tamba, G. H Mehl, "Spontaneous periodic deformations and linear optical response in nonchiral bimesogens with nematic-nematic transition", 24th International Liquid Crystal Conference, Mainz, Germany, 19th - 24th August, 2012.

5. Vitaly P. Panov, M. Nagaraj, **R. Balachandran**, J. K. Vij, M. G. Tamba and G. H. Mehl,"Microsecond linear optical response in the unusual nematic phase of achiral bimesogens", 8th BIND Project Meeting , Dublin, Ireland, 24-27 October 2011.

6. **R. Balachandran,** V.P.Panov, A. Kocot, J. K. Vij, , A. Lehmann, C. Tschierske, "Determing the elastic constants of bent core nematic liquid crystals showing sign reversal in dielectric anisotropy", Photonics Ireland 2011, 7th - 9th September, 2011.

Flexo-Elastic and Electro-Optical Studies of some Novel Liquid Crystalline Systems

Reshma Balachandran

Department of Electronic and Electrical Engineering,
Trinity College Dublin, Dublin 2, Ireland

The knowledge of the material properties of liquid crystals is very important in the design and optimization of LC based devices. The work presented in this thesis is primarily concerned with the study of material parameters such as dielectric anisotropy, elastic constants and effective flexoelectric coefficients in the nematic phase of some bent-core mesogens and bimesogens. Some of the main findings of this thesis are summarized below:

- It is found experimentally that the cybotactic clusters may not significantly affect the flexo-elastic properties exhibited by bent-core nematics; instead these properties are more likely to be influenced by the bent shape of the molecules.

- In an odd bimesogen, composed of two rod-like molecules connected by a flexible spacer, the bend (K_{33}) elastic constant is observed to decrease by a factor of almost 3 below the splay (K_{11}) constant as the temperature approaches the twist-bend nematic phase. The effective flexoelectric coefficient is found to be at least two times higher than for bimesogens that do not exhibit the N_{tb} phase. The flexoelectric polarization in the N_{tb} phase is almost twice greater than in its nematic phase.

- At temperatures near the N-N_{tb} phase a new type of striped pattern is observed under polarizing microscope in some odd bimesogens and their mixtures with the monomer (5CB), in a planar aligned cell. This phenomenon is reminiscent of the self-deformation and spontaneous chirality that appears in the system.

- A dimesogen composed of a bent-core and calamitic unit exhibits dual frequency nematic mode, as confirmed by dielectric and electro-optic studies. The sign reversal of dielectric anisotropy occurs at much lower frequencies. Investigation of the dielectric spectra using the M-M model suggests the presence of anti-parallel correlation of the transverse dipoles in the neighbouring layers of the SmC like clusters.